Optical Gas-Phase Frequency References Based on Photonic Crystal Technology: Impact of Slow Light on Molecular Absorption

THÈSE N^{O} 5267 (2012)

PRÉSENTÉE LE 17 FÉVRIER 2012
À LA FACULTÉ DES SCIENCES ET TECHNIQUES DE L'INGÉNIEUR
INSTITUT DE GÉNIE ÉLECTRIQUE ET ÉLECTRONIQUE
PROGRAMME DOCTORAL EN PHOTONIQUE

ÉCOLE POLYTECHNIQUE FÉDÉRALE DE LAUSANNE

POUR L'OBTENTION DU GRADE DE DOCTEUR ÈS SCIENCES

PAR

Isabelle DICAIRE

acceptée sur proposition du jury:

Prof. O. Martin, président du jury
Prof. L. Thévenaz, directeur de thèse
Prof. T. Kippenberg, rapporteur
Prof. J. Knight, rapporteur
Dr E. Murphy, rapporteur

ÉCOLE POLYTECHNIQUE
FÉDÉRALE DE LAUSANNE
Suisse
2012

ACKNOWLEDGEMENTS

This thesis has been realised in the Group for Fibre Optics at EPFL under the supervision of Prof. Luc Thévenaz. First and foremost I wish to warmly thank him for allowing me to join his group and for believing in my abilities to do scientific research. He always welcomed my questions and helped me to improve my understanding of physics principles. On the personal side my funny Canadian French accent was always a source of amusement for him and I enjoyed the numerous conversations we had about that topic. I could not have imagined having a better advisor and mentor for my Ph.D. studies.

My warm thanks to my thesis jury members, Prof. Jonathan Knight from the University of Bath, U.K., Dr. Eamonn Murphy from the European Space Agency, and Prof. Tobias Kippenberg from EPFL. They gave constructive advice and valuable suggestions which greatly improved the quality of this thesis. In addition Eamonn followed my research progress as second advisor and I warmly thank him for his kind support throughout my studies. The financial support of the European Space Agency is gratefully acknowledged.

I am indebted to Dr. Alfredo De Rossi and Dr. Sylvain Combrié from Thales Research and Technology for providing the photonic crystal waveguide samples and to Prof. Kyunghwan Oh from Yonsei University in Seoul, South Korea and University Marie-Curie Skłodowskiej (UMCS) in Lublin, Poland (via Prof. Waclaw Urbanczyk from the Wroclaw University of Technology, Poland) for providing the photonic crystal fibres.

Special thanks to Dr. Stéphane Schilt for his guidance in laser spectroscopy and to Dr. Jean-Charles Beugnot for his support and constant interest in my research studies. My acknowledgement also goes to Pascal Morel for his time spent on technical drawings for my projects.

I thank my fellow colleagues in the Group for Fibre Optics for providing a stimulating environment in which to learn and grow. In particular I thank Stella Foaleng-Mafang for her friendship, Sanghoon Chin and Nikolay Primerov for insightful discussions about science and life in general, and Andrey Denisov for his assistance during the delivery process of the thesis. I also appreciate the assistance I received from the Ph.D. students at Yonsei University in Seoul, South Korea. I could spend a wonderful time there during my stay thanks to their support and friendship.

I wish to thank the two successive secretaries of our Group Luana Huguenin & Alexandra Mor-

rison and the secretary of the doctoral program Pierrette Paulou-Vaucher for their administrative help and interesting discussions.

I am grateful to my extended family for providing a loving and supportive environment for me. My grandparents Denise and Gérard from my father's side and Estelle and late Paul from my mother's side were particularly supportive throughout my studies.

My deepest gratitude goes to my parents Daniel and Lucie and to my sister Marie-Ève for their continuous love and support throughout my life; this thesis would have been impossible without them. And most of all I warmly thank my long-term boyfriend Maxime for his supportive, reassuring, and loving presence during my studies in Switzerland. His faithful support during the final stages of this Ph.D. is greatly appreciated. Thank you.

Isabelle Dicaire
EPFL, Lausanne
January 2012

VERSION ABRÉGÉE

Les références de fréquence optiques sont des dispositifs fournissant une réponse en fréquence stable et bien définie à un rayonnement optique incident, pour des applications telles que la spectroscopie à haute résolution et les communications par fibre optique. Pour stabiliser de façon précise la fréquence d'émission de sources laser, qui de façon générale va varier au cours du temps principalement à cause de fluctuations en température et de vibrations mécaniques, les transitions atomiques et moléculaires peuvent être utilisées car elles démontrent une réponse en fréquence stable et précise au rayonnement incident. Cependant d'un point de vue pratique les dispositifs classiques de cellules de gaz peuvent être difficilement intégrés aux systèmes optiques actuels en raison de leurs dimensions volumineuses. Afin de remplacer les cellules conventionnelles, les fibres à cristaux photoniques contenant de façon hermétique des molécules de gaz sont des dispositifs prometteurs en raison de leur robustesse, fiabilité et portabilité. En outre, elles peuvent être directement intégrées dans des systèmes optiques embarqués et elles sont efficaces et fiables même dans des conditions extrêmes. Dans cette étude expérimentale, des références de fréquence optiques sont réalisées en utilisant la technologie des cristaux photoniques. Les propriétés de détection de gaz de différents échantillons de fibres à cristaux photoniques sont étudiées et la stabilité et la fiabilité à long terme des cellules de gaz fibrées sont démontrées. En outre, un modèle analytique de prédiction du temps de remplissage de gaz des capillaires de fibres à cristaux photoniques est développé et peut être appliqué à tout type de microstructure et pour toute longueur de fibre. Puis les cellules de gaz fibrées contenant du gaz d'acétylène, une référence de fréquence reconnue, ont été préparées afin d'effectuer des recherches fondamentales sur la génération de lumière lente et rapide dans des fibres optiques pour vérifier si la lumière lente pouvait augmenter l'effet de l'interaction lumière-matière. La vitesse de groupe de la lumière est contrôlée en modifiant les propriétés de dispersion matérielles et structurelles des cellules d'absorption fibrées en utilisant respectivement la diffusion Brillouin stimulée et les cavités résonantes fibrées. Nous avons pu démontrer que la lumière lente matérielle n'a aucun impact sur l'absorption moléculaire tandis que lumière lente structurelle a un impact sur l'efficacité d'absorption qui est linéaire avec l'indice du groupe. Cette différente réponse à la propagation en régime de lumière lente suggère que la vitesse de groupe n'est pas la quantité physique universelle décrivant l'interaction lumière-matière et que l'absorption optique des molécules est plus étroitement liée à la vitesse de l'énergie électromagnétique. Enfin, l'impact de la lumière lente sur l'efficacité d'absorption moléculaire est également évalué dans des guides d'ondes planaires à cristaux photoniques avec dispersion structurelle modifiée. Nous démontrons que l'augmentation de la densité du champ électrique et de sa fraction évanescente a plus d'impact sur l'efficacité d'absorption que la réduction de la vitesse de groupe de la lumière dans les guides d'ondes planaires à cristaux photoniques.

Mots clés: Références de fréquence optiques, fibres à cristaux photoniques, fibres optiques microstructurées, absorption moléculaire, guides d'ondes à cristaux photonique, spectroscopie laser, capteurs fibrés, lumière lente, dispersion, diffusion.

ABSTRACT

Optical frequency references are devices providing well-defined and stable optical frequency responses to incoming radiation for applications such as high-precision spectroscopy and optical fibre communications. To stabilise the emission frequency of lasers, which drifts with time mostly because of fluctuations in temperature and mechanical vibrations, atomic and molecular optical transitions can be used since they show precise and well-defined frequency responses to incoming radiation. However from a practical standpoint conventional gas cell devices cannot be easily integrated into existing optical systems because of their bulky dimensions. To replace conventional absorption cells, photonic crystal fibres filled with gas-phase material are promising devices owing to their robustness, reliability, and portable characteristics. In addition they can be directly embedded into existing optical systems and they perform well in harsh environments. In this experimental study, optical gas-phase frequency references based on photonic crystal technology are realised. The gas-sensing properties of different photonic crystal fibre samples are studied and the long-term stability and reliability of fibre gas cells are demonstrated. In addition an analytical model predicting the gas-filling time in photonic crystal fibres (PCF) is developed and can be applied to any type of fibre, fibre geometry, or length. Then fibre gas cells filled with acetylene gas, a recognised frequency reference gas-phase material, have been prepared to conduct fundamental research on slow & fast light generation in optical fibres to verify the possibilities of slow light in enhancing light-matter interaction. The group velocity of light is controlled by modifying the material and structural dispersive properties of the PCF absorption cells through stimulated Brillouin scattering and cavity ring resonators, respectively. We could demonstrate that material slow light has no impact on the molecular absorption effect whereas structural slow light has an impact on the absorption efficiency scaling linearly with the group index. Such radically different responses to slow light suggest that group velocity is not the universal physical quantity scaling light-matter interaction, and that the optical absorption of molecules is more closely related to the velocity of the electromagnetic energy. Finally the impact of slow light on the molecular absorption efficiency is also evaluated in dispersion-engineered photonic crystal waveguides. We demonstrate that in planar photonic crystal waveguides the field enhancement and its evanescent fraction have more impact on the absorption efficiency than the reduction of the group velocity of light.

Keywords: Optical frequency references, photonic crystal fibres, microstructured optical fibres, molecular absorption, photonic crystal waveguides, laser spectroscopy, fibre optics sensors, slow light, dispersion, diffusion.

CONTENTS

LIST OF FIGURES xiii

LIST OF TABLES xxiii

INTRODUCTION 1

CHAPTER 1: MOLECULAR ABSORPTION SPECTROSCOPY 7

- 1.1 Introduction 7
- 1.2 Molecular absorption 7
- 1.3 The lineshape function 10
- 1.4 Line broadening 12
  - 1.4.A Lifetime broadening 12
  - 1.4.B Pressure broadening 13
  - 1.4.C Doppler broadening 13
  - 1.4.D Transit-time broadening 15
  - 1.4.E Saturation broadening 16
- 1.5 Absorption Spectroscopy Techniques 16
  - 1.5.A Tunable Diode Laser Absorption Spectroscopy (TDLAS) 17
  - 1.5.B Saturated Absorption Spectroscopy (SAS) 19
  - 1.5.C Wavelength Modulated Spectroscopy (WMS) 23

CHAPTER 2: GAS SPECTROSCOPY USING PHOTONIC CRYSTAL FIBRES 31

- 2.1 Introduction 31
- 2.2 Photonic crystal fibres 31
- 2.3 Dynamics of gas diffusion inside photonic crystal fibres 34
  - 2.3.A Theory of Gas Diffusion 34
  - 2.3.B Gas Filling Dynamics 38
  - 2.3.C Experimental Procedure 40
  - 2.3.D Results and Analysis 40
  - 2.3.E Ideal Gas Filling Conditions 41

2.4 All-fibre absorption cells 43
2.4.A The helium permeation technique 44
2.4.B Long-term stability of fibre gas cells 45
2.4.C Comparative study of various all-fibre absorption cells 46
2.5 Laser stabilisation using fibre gas cells 47
CHAPTER 3: MOLECULAR ABSORPTION AND SLOW LIGHT IN OPTICAL FIBRES 53
3.1 Introduction 53
3.2 Signal propagation in dispersive media 53
3.3 Material and structural slow light 55
3.4 Material slow light via Stimulated Brillouin Scattering 56
3.4.A Stimulated Brillouin Scattering 58
3.4.B Experimental configuration and results 59
3.4.C Discussion 63
3.5 Structural slow light via Cavity Ring Resonators 65
3.5.A Theoretical group delay in long cavity ring resonators 65
3.5.B Experimental configuration and results 69
3.5.C Discussion 74
3.6 Conclusion 76
CHAPTER 4: GAS SPECTROSCOPY USING PHOTONIC CRYSTAL WAVEGUIDES 79
4.1 Introduction 79
4.2 Photonic crystal waveguides 80
4.3 Slow light in photonic crystal waveguides 81
4.4 Experimental study of molecular absorption in photonic crystal waveguides 83
4.4.A Experimental setup 83
4.4.B Results 87
4.4.C Lineshape analysis 90
4.5 Theoretical absorption coefficient in photonic crystal waveguides 92

4.6 Conclusion 95

CONCLUSIONS AND PERSPECTIVES 99

Appendix I: Computation of the theoretical Lorentzian width xxv

Appendix II: Computation of the theoretical saturation power in photonic crystal waveguides xxvii

LIST OF PUBLICATIONS xxix

CURRICULUM VITAE xxxiii

LIST OF FIGURES

1.1 Rotational vibrational transitions and their relative positions in the spectrum. The ground vibrational state $v'' = 0$ and the first excited vibrational state $v' = 1$ are shown with their respective fine structure corresponding to rotational states labelled using the rotational quantum number J. 9

1.2 Line strengths S of the $\nu_1 + \nu_3$ ro-vibrational absorption band of acetylene at $\lambda = 1.5\mu$m (Hitran database). Each absorption line is related to a different rotational transition and rotational quantum number J. Several weaker sets of absorption lines can also be seen in the spectrum; they correspond to the so-called hot bands, where lower states are thermally excited states with population described by the Boltzmann distribution (Eq. 1.30). 11

1.3 Typical line profile with associated energy levels. The gray area represents the energy uncertainty due to the finite lifetime of the energy levels. 12

1.4 Voigt profile as a convolution of Lorentzian and Gaussian lineshapes. The left panel shows several Lorentzian profiles weighted by their respective probability $p(\nu)$ (dashed line). The right panel illustrates the difference in lineshapes between a Doppler-limited profile $g_D(\nu)$ and a Voigt profile $g_V(\nu)$ with a Lorentzian contribution $g_L(\nu)$ shown for molecules moving perpendicularly to the laser beam. 15

1.5 Absorption spectrum of acetylene measured at $\lambda = 1.5\mu$m with a high-resolution OSA. The amplified spontaneous emission (ASE) of an erbium-doped fibre amplifier (EDFA) was used as broadband source. 17

1.6 Left panel: absorption lines measured for various acetylene gas pressures ($\lambda = 1534.1\,\mathrm{nm}$). The saturation in absorption efficiency is visible for pressures values higher than 150 mbars. Right panel: the lineshape function, which represents the absorption cross section of each molecule, and the absorption linewidth are strongly dependent on the gas pressure. 18

1.7 Experimental configuration of the SAS experiment. Pump and probe signals are counterpropagating along distinct polarisations in the fibre absorption cell. Lock-in detection is performed to acquire clean signals. 21

1.8 Lamb dips obtained for several pump power values (λ=1533.46nm). The theoretical saturation power of 410 mW agrees well with the experimental values needed to saturate the acetylene vibration transition. 22

1.9 Experimental configuration of the WMS technique where a 2-kHz sine modulation is added to a 5-Hz ramp signal. A weak absorption line is obtained by filling a vacuum chamber with 7 mbars of acetylene gas (T=98.5%). A lock-in amplifier tuned to the sine modulation frequency extracts the second harmonic signal which is observed using an oscilloscope. 23

1.10 Wavelength Modulated Spectroscopy (P15 line, $\lambda = 1534.1\,\mathrm{nm}$). Left panel: second-harmonic signals as a function of the frequency detuning for several modulation indices (represented here in units of injection current). Right panel: amplitude of the second-harmonic signal S_{2f} as a function of the driving current of the sine modulation. 26

2.1 Several examples of photonic crystal fibres. Scale bars indicate 20 μm. 32

2.2 Calculated diffusion coefficients of acetylene gas for several capillary diameters. The various flow regimes are defined according to the two blue lines representing Knudsen numbers of 1 and 0.01 respectively. 34

2.3 Calculated diffusion coefficient of acetylene gas for several hole diameters in the slip-flow regime according to Eq. 2.11 & 2.12. 38

2.4 Filling process measured as a function of time in a suspended-core PCF (A), a microstructured-core PCF (B), and a solid-core PCF (C). The black curves represent nonlinear fittings of Eq. 2.13 from which experimental diffusion coefficients can be obtained. All scale bars represent 20 μm. 41

2.5 Experimental diffusion coefficients for acetylene gas diffusing in suspended-core fibres (hole diameter: 11.8 μm, scale bar: 10 μm) obtained using Eq. 2.11. The black curve represents diffusion coefficients calculated with average pressures taken as 2/3 of the filling pressures. 42

2.6 Contours of constant filling time are plotted in the $2a-L$ plane for a filling pressure of 100 mbars according to Eq. 2.11 & 2.15 ($P/P_0 = 85\%$). 43

2.7 Helium permeation process in a microstructured-core photonic crystal fibre. From the initial gas loading to the final sealed absorption cell, the width of the absorption line remains equal, demonstrating the efficiency of the technique. . 45

2.8 Long-term absorption stability of two fibre gas cells, a microstructured-core PCF (B) and a hollow-core PCF (D) (scale bars indicate 20 μm). The blue and pink curves represents absorption profiles measured directly after the gas cells were prepared. The green and red curves represent absorption profiles measured 7 and 20 months later, respectively. 46

2.9 All-fibre frequency stabilisation system. A 1.869-kHz sine modulation dithers the injection current of a DFB laser diode and a lock-in amplifier demodulates the detected signal at the sine frequency. A feedback loop provides injection current corrections to the laser controller to compensate any frequency drift of the laser line. 48

2.10 Frequency stabilisation of a DFB laser diode using a PCF frequency reference filled with 76 mbars of acetylene gas. Left panel: Signal profile of the error function. The dashed line represents the linear fitting of the error signal in the central region. Right panel: Laser fluctuations as a function of time in free-runing and in locked-mode. Frequency fluctuations are reduced from 15 MHz to 0.3 MHz by locking the laser line to the P15 absorption line ($\lambda = 1534.1$nm). 49

3.1 Left panel: Initial optical signal $E(0,t)$ (solid curve) with signal envelope $E_{env}(t)$ (dashed curve). Right panel: Fourier amplitude distribution centered about ω (solid curve) for the optical signal and zero (dashed curve) for that of the envelope $E_{env}(\Omega)$. 55

3.2 Left panel: Brillouin gain (solid line) and dispersion (dashed line) for a 30-MHz Brillouin resonance [3]. Right panel: Corresponding group index increase. . . . 57

3.3 Observation of pulse delaying using stimulated Brillouin scattering (SBS) based slow-light. The higher the pump power and the stronger the dispersive effect one can obtain in order to decrease the group velocity. These measurements were obtained in a 9.18-m long solid-core photonic crystal fibre. 57

3.4 Schematic representation of the stimulated Brillouin scattering (SBS) process. A signal wave experiences gain from a counterpropagating pump spectrally upshifted by the Brillouin frequency shift ν_B. The interference beating of both waves creates via electrostriction an acoustic wave that diffracts the pump wave into the signal wave, reinforcing the nonlinear coupling. (From chapter 9 of [3], with permission). 58

3.5 All-fibre gas absorption cell. Left panel: Calculated mode field distribution of the fundamental mode. Middle panel: SEM image of the solid-core photonic crystal fibre. Right panel: Distribution of the small evanescent fraction of the optical field available for sensing. 60

3.6 Experimental setup realising simultaneously slow-light and gas absorption in the same fibre gas cell. The optical frequency of the signal is amplified and slowed down using stimulated Brillouin scattering and is scanned through an absorption line. The frequency separation between the pump wave and the signal wave remains constant during the frequency scan. 60

3.7 Effect of Brillouin slow-light on the P15 acetylene absorption profile. Left panel: P15 absorption profiles measured for several pump powers. Right panel: Peak absorption measured as a function of the slow-down factor (squares). The black dashed line represents the data points fitted with a constant value ($A =$ 5.940 dB) while the blue line represents an absorption coefficient hypothetically proportional to the slow-down factor. 61

3.8 Effect of Brillouin slow-light on the P17 acetylene absorption profile. Left panel: P17 absorption profiles measured for several pump powers. Right panel: Peak absorption measured as a function of the slow-down factor (squares). The black dashed line represents the data points fitted with a constant value ($A = 4.654$ dB) while the blue line represents an absorption coefficient hypothetically proportional to the slow-down factor. 62

3.9 Theoretical group velocity profile v_g across a Brillouin resonance for a 15 dB gain in a 9.18-m long PCF fibre and normalised by its off-resonance value. . . 64

3.10 Theoretical electromagnetic (EM) energy velocity profile $v_{EM}(\omega)$ across a Brillouin resonance for a 15 dB gain in a 9.18-m long PCF fibre (Eq. 3.14). 65

3.11 Theoretical delaying effect of the macroscopic cavity system on 5 μs Gaussian pulses for several cavity recirculation factors η (based on Eq. 3.21). 66

3.12 Theoretical group delay obtained using macroscopic cavity ring resonators as a function of the recirculation factor and normalised by the cavity round-trip time τ. 69

3.13 Experimental setup realising structural slow light using a long fibre ring resonator system. Variable group delay is achieved by modifying the propagation loss in the fibre loop. The gas cell is made of a photonic crystal fibre filled with acetylene gas and fusion spliced to standard single-mode fibres. 70

3.14 Cavity ring down measurements. A cavity round-trip loss of 1.7 dB/pass is found by fitting the exponentially decaying pulse intensities and measuring the cavity round-trip time (260 ns). 70

3.15 Left: Pulse delay measurements shown for several cavity round-trip losses. Decreasing the cavity loss leads to longer pulse arrival time through light recirculation. Right: Group delay measured as a function of the cavity round-trip loss using the phase shift technique. The dashed curve shows theoretical dependence obtained from Eq. 3.30 for a cavity round-trip time of 260 ns. . . . 71

3.16 Left: Absorption profiles measured in the 5.0-m long hollow-core PCF for the P14 line ($\lambda = 1533.46$ nm) for several group indices. Right: Absorption enhancement as a function of the group index. The dashed line represents Eq. 3.35 fitted with $A_0 = 1.75$ dB. 72

3.17 Left: Absorption profiles measured in the 9.18-m long solid-core PCF for the P15 line ($\lambda = 1534.10$ nm) for several group indices. Right: Absorption enhancement as a function of the group index. The dashed line represents Eq. 3.35 fitted with $A_0 = 5.5$ dB. 73

3.18 Left: Absorption profiles measured in the 9.18-m long solid-core PCF for the P17 line ($\lambda = 1535.40$ nm) for several group indices. Right: Absorption enhancement as a function of the group index. The dashed line represents Eq. 3.35 fitted with $A_0 = 4.5$ dB. 73

3.19 Left: Absorption profiles measured in the hollow-core PCF for the P14 line ($\lambda = 1533.46$ nm) for several cavity round-trip losses. Right: Absorption enhancement as a function of the cavity round-trip losses. The dashed line represents the theoretical absorption enhancement expected for a longer effective optical path length through light recirculation (Eq. 3.33). 75

3.20 Left: Absorption profiles measured at $\lambda = 1535.43$nm in the 5.0-m long hollow-core PCF for several group indices. Right: Absorption enhancement as a function of the group index. The dashed line represents Eq.3.35 fitted with $A_0 = 0.2457$ dB while the dotted line represents an absorption coefficient scaling linearly with n_g (Eq. 3.36). 76

3.21 Dependence of the optical absorption of molecules on the group index for material slow light (white squares) and structural slow light (black squares). The dotted line represents an absorption coefficient constant with group index and the dashed line represents the theoretical model for the absorption enhancement in macroscopic cavities (Eq. 3.35). Larger error bars seen for the structural slow-light data points are related to normalisation issues due to a non-uniform intensity build-up of the line background, whereas gain uniformity is ensured for the material slow-light experiment via simultaneous tuning of the pump and signal waves. 77

4.1 Micrograph of a photonic crystal waveguide made of Gallium Indium Phosphide (GaInP) (Courtesy of Thales Research and Technology). The membrane thickness is 180 nm (not shown here). The lattice constant is ∼500 nm and the diameter of the air holes is 220 nm. The white scale bar represents 3 μm. . . 80

4.2 Transmission and group index characteristics of a photonic crystal waveguide fabricated and characterised by Thales Research and Technology, http://www.thalesresearch.com. The structural dispersion properties were tuned by increasing the innermost hole diameter from 224 nm to 252 nm. . . . 82

4.3 End-fire setup for photonic crystal characterisation. Optical coupling is ensured by lensed optical fibres precisely aligned with the line defect of the photonic crystals. 83

4.4 Stability of the optical coupling to external perturbations with the end-fire setup placed inside a gas chamber. Air is evacuated from the chamber using a vacuum pump and 70 mbars of acetylene gas is introduced in the chamber. A transmission difference of only 1 dB is obtained during the gas loading process. 85

4.5 Transmission spectrum of several photonic crystal waveguides with different group indices n_g measured at 1534 nm. The band-edges are clearly seen for all measured waveguides and are positioned closer to the reference wavelength λ =1534 nm for waveguides having larger group indices at this wavelength, demonstrating that lower group velocities can be obtained for light signals propagating closer to the bandgap. 86

4.6 Variarion of the absorption line shape with group index. The black curve represents the experimental absorption of acetylene gas over a distance equal to 30 % of the photonic crystal length. The maximum absorption is $A = 0.0440$ dB for $n_g = 5$ and $A = 0.0678$ dB for $n_g = 7$. The linewidth is [0.87 ± 0.05] GHz for the black curve and [1.40 ± 0.05] GHz & [1.46 ± 0.05] GHz for $n_g = 5$ & $n_g = 7$ respectively. The difference in linewidths is due to different contributions from transit-time broadening (see §4.4.C for a detailed lineshape analysis). . . 87

4.7 Top: Simulated intensity of the electric field $\| E \|^2$ for the TE polarisation along the transverse section of the photonic crystal slab. The electric field is strongly confined to the high-index dielectric slab and cannot therefore interact with the gas molecules. Bottom: Simulated time-averaged Poynting vector $\frac{1}{2}\Re[E \times H^*]$ for the TE polarisation along the transverse section of the photonic crystal slab. Numerical simulations are a courtesy of Thales Research and Technology. . . . 88

4.8 Absorption profiles along the TM polarisation for several photonic crystals with the n_g values corresponding to the TE engineered ones. The TM values are all approximately equal to $n_g = 1.7$. The black curve represents the simulated absorption of acetylene gas over a distance equal to the photonic crystal length for an overlap fraction between the optical power and the gas molecules of 100 %. The maximum absorption is $A = 0.218$ dB for the simulated molecular absorption (black curve) and $A = [0.224 \pm 0.007]$ dB for the absorption profiles measured in the photonic crystal samples. 89

4.9 Left: Simulated intensity of the electric field $\| E \|^2$ for the TM polarisation along the transverse section of the photonic crystal slab. The electric field is located mostly in the lower-index material and can therefore strongly interact with the gas molecules. Right: Time-averaged Poynting vector $\frac{1}{2}\Re[E \times H^*]$ for the TM polarisation. Numerical simulations are a courtesy of Thales Research and Technology. 89

4.10 Simulated absorption relative to free-space propagation for the TE polarisation in photonic crystal waveguides as a function of the optical frequency normalised by the lattice constant a and the speed of light c. The electric field is strongly confined to the high-index dielectric slab and decays rapidely outside the slab in the low-index medium, leading to low overlap fractions with the gas molecules. The theoretical absorption coefficient is less than unity in all situations, hence smaller than in free-space propagation. Numerical simulations are a courtesy of Thales Research and Technology. 93

4.11 Simulated absorption relative to free-space propagation for the TM polarisation in photonic crystal waveguides as a function of the optical frequency normalised by the lattice constant a and the speed of light c. The electric field is located mostly in the low-index medium and can therefore strongly interact with the gas molecules. The theoretical absorption coefficient is approximately the same as that obtained in free-space propagation even though the optical mode is guided within the planar waveguide. Very weak dependence of the absorption coefficient on the group index is obtained. Numerical simulations are a courtesy of Thales Research and Technology. 94

LIST OF TABLES

1.I Wavelength bands and associated dominant transitions 8

1.II Fundamental vibrational modes of acetylene 9

2.I Characteristics of the microstructured fibres 40

2.II Permeation constants for several gases in fused silica [24] 44

4.I Characteristics of different absorption profiles obtained in photonic crystals . . 91

4.II Experimental and simulated relative logarithmic absorption coefficients 95

I.I Calculated broadening contributions xxv

INTRODUCTION

Optical frequency references are devices designed to provide stable optical frequencies, that can be classified in two types of frequency references or frequency standards. First active frequency standards are basically laser sources emitting light at a very well defined and known optical frequency or at a set of evenly spaced frequencies known as a frequency comb. Then passive frequency standards are passive devices showing well-defined frequency responses to incoming radiation, which can be used to build active frequency standards. Frequency metrology requires the development of frequency references because the emission frequency of lasers tends to drift with time, mostly due to fluctuations in temperature and acoustic vibrations of laser cavity mirrors. To stabilise laser frequencies atomic and molecular optical transitions are typically used since they show precise and well-defined frequency responses given by quantum mechanics and the quantisation of energy levels in atoms and molecules. Following theoretical considerations by M. Planck and A. Einstein early in 1900's regarding quantisation of light, N. Bohr conjectured in 1913 that atoms and molecules are only allowed a discrete set of energy states. He also explained that atoms and molecules absorb and emit radiation following quantum transitions from one of their allowed states to another one. The theory could successfully qualitatively explain the absorption of electromagnetic radiation and the formation of discrete spectral lines. Laser frequencies locked to optical transitions considerably reduce the sensitivity of the lasing system to external perturbations and provide the stable frequency (or time for that matter) output needed for optical clocks. Applications of ultraprecise optical frequency references include high precision spectroscopy, global positioning systems, and optical fibre communications. Optical frequency references offer the possibility of improving current time keeping performances by several orders of magnitude with respect to current microwave atomic clocks [7].

In frequency metrology frequency standards are characterised by their stability, accuracy, and reproducibility [3, 5]. Stability indicates the degree to which the output frequency stays constant throughout operation. Accuracy refers to the ability of the frequency standard to match the frequency value of the natural transition. Finally reproducibility or precision refers to the degree to which repeated measurements of the output frequency in different settings and under different conditions will yield values close to the average frequency value. As an example a frequency standard showing a systematic frequency shift can be stable, precise but not accurate. Accurate frequency references are necessarily stable over long time intervals, but not all stable references are accurate.

There are several requirements for obtaining precise optical frequency references. The optical transition should be as narrow as possible to reduce the frequency uncertainty of the stabilised laser. To reduce the homogeneous broadening due to collisions between gas molecules the gas pressure is reduced to a minimum value. As for the inhomogeneous broadening due to thermal motion of gas molecules the operating temperature is minimised using advanced cooling techniques. For applications requiring lower precision, simple gas cells with low molecular densities are realised and probed by advanced techniques such as Doppler-free spectroscopy. In addition the optical transition should be insensitive to external perturbations such as electric or magnetic fields. Finally the optical transition frequency should be convenient so that suitable interrogation and processing systems are available.

Among all molecular gases, acetylene gas is a promising optical frequency reference gas for performing laser stabilisation and is recognised by the International Committee for Weights and Measures. It exhibits a certain number of reference transitions conveniently located in the 1.5 μm telecommunication wavelengths. These lines probed by Doppler-free spectroscopy have widths on the order of 1 MHz and can provide frequency standards with uncertainty level of $\Delta\nu/\nu_0 = 10^{-10}$ or better [2, 4]. In addition acetylene molecules are negligibly affected by magnetic fields and are therefore considered accurate and precise frequency standards. From the point of view of practical applications multipass absorption cells cannot be easily integrated into optical systems due to their bulky dimensions. There is therefore a pressing need for portable, compact, robust, and reliable gas cells to replace conventional gas cells. Recent developments in fibre optics technology have made possible the realisation of optical fibres having hollow transverse sections, which can be filled with gas-phase material and showing substantial interaction with the guided mode [1]. Moreover they can be fusion spliced to standard optical fibres and directly embedded in optical systems and instruments. Photonic crystal fibres are thus promising devices for realising all-fibre gas cells and are particularly attractive for the space industry thanks to their cost-effective and light-weight properties combined with their long-term reliability and intrinsic immunity to electromagnetic interferences.

The first objective of this thesis is to evaluate the possibilities of photonic crystal fibres in realising portable gas cells. To serve as optical frequency references these gas cells should contain a low density of molecules, i.e. filled with low pressure gas. To prevent contamination by air molecules during the fusion splicing procedure, a clever gas-filling technique based on helium permeation has been tested. In this technique the fibre capillaries are filled with helium gas to bring the total pressure inside the fibre holes to more than the surrounding atmospheric pressure, thus avoiding particle contamination during the splicing procedure [6]. Once the fibre gas cell is perfectly sealed the high permeation rate of helium gas through silica glass will yield a perfectly hermetic gas cell containing a pure set of low-density molecules. The second objective of the thesis is to verify the long-term efficiency of the helium technique regarding the stability of the absorption profiles and to test the possibilities of such all-fibre gas cells as optical frequency references by implementing a laser stabilisation scheme.

The third objective is to conduct fundamental research on the applications of gas-phase fibre cells to advanced systems such as saturated absorption spectroscopy and slow & fast light generation. Photonic crystal fibre technology allows for effective interactions between light and matter as part of the guided optical mode can interact over a very long distance with the gas-phase material filled in the fibre capillaries. However for gas-detection applications it is always desirable to improve sensing efficiencies as to realise more compact devices. Theoretical considerations suggested that slowing down the velocity of a light signal could lead to enhanced light-matter interactions [8]. To experimentally verify the impact of slow light on molecular absorption the material and structural dispersion properties of photonic crystal fibre gas cells are modified and the resulting absorption efficiencies compared to standard propagation. The impact of slow light on the molecular absorption effect is also evaluated in dispersion-engineered photonic crystal waveguides to hopefully gain new insights on the management of light-matter interactions.

This thesis is organized as follows. The first Chapter reviews the basics of molecular absorption spectroscopy in the near infrared region of the electromagnetic spectrum. The most important contributions to linewidth broadening are presented as well as three advanced and complementary spectroscopic techniques commonly used in laser spectroscopy.

The second Chapter presents gas spectroscopic measurements performed using photonic crystal fibres. The dynamics of gas diffusion are studied and a simple analytical model predicting the gas-filling time in photonic crystal fibres is developed. The helium permeation technique enabling the realisation of low-density fibre gas cells is tested to verify its efficiency in obtaining a pure set of gas molecules that is fully contained in the fibre capillaries. Moreover the long-term efficiency and reliability of the sealing technique is verified by acquiring high-resolution gas absorption spectra in different fibre geometries over a two-year period. The relative performance of various types of photonic crystal fibres showing different transverse geometries is qualitatively studied by comparing the spectral quality of their transmission spectra and the linewidths of their absorption profiles. Finally a simple laser stabilisation scheme is implemented to test possible applications of all-fibre gas cells as optical frequency references.

The third Chapter is devoted to the experimental verification of the impact of slow-light on molecular absorption using optical fibres. The material and structural dispersion properties of optical systems based on photonic crystal fibres are modified and the impact on the effect of molecular absorption is analysed by performing high-resolution gas spectroscopic measurements.

The fourth Chapter presents gas spectroscopic measurements using dispersion-engineered photonic crystal slab waveguides. Their gas sensing capabilities in the slow-light regime are critically studied and compared to free-space propagation to investigate their possibilities in enhancing light-matter interactions to eventually realise ultra-compact frequency references.

References

[1] Benabid, F., Couny, F., Knight, J. C., Birks, T. A., and Russell, P. S. J. (2005). Compact, stable and efficient all-fibre gas cells using hollow-core photonic crystal fibres. *Nature*, 434:488–491.

[2] Czajkowski, A., Madej, A., and Dubé, P. (2004). Development and study of a 1.5 μm optical frequency standard referenced to the P(16) saturated absorption line in the $\nu_1 + \nu_3$ overtone band of $^{13}C_2H_2$. *Optics Communications*, 234(1-6):259 – 268.

[3] Diddams, S. A., Bergquist, J. C., Jefferts, S. R., and Oates, C. W. (2004). Standards of time and frequency at the outset of the 21^{st} century. *Science*, 306(5700):1318–1324.

[4] Edwards, C. S., Margolis, H. S., Barwood, G. P., Lea, S. N., Gill, P., Huang, G., and Rowley, W. R. C. (2004). Absolute frequency measurement of a 1.5-μm acetylene standard by use of a combined frequency chain and femtosecond comb. *Optics Letters*, 29(6):566–568.

[5] Hall, J. L. and Ye, J. (2001). A new era of frequency standards and optical frequency measurement. *Opt. Photon. News*, 12(2):44–50.

[6] Light, P. S., Couny, F., and Benabid, F. (2006). Low optical insertion-loss and vacuum-pressure all-fiber acetylene cell based on hollow-core photonic crystal fiber. *Opt. Lett.*, 31(17):2538–2540.

[7] Ma, L.-S. (2007). Optical Atomic Clocks-From Dream to Reality. *Opt. Photon. News*, 18(9):42–47.

[8] Mortensen, N. A. and Xiao, S. (2007). Slow-light enhancement of Beer-Lambert-Bouguer absorption. *Applied Physics Letters*, 90(14):141108.

CHAPTER 1

MOLECULAR ABSORPTION SPECTROSCOPY

1.1. Introduction

Molecular spectroscopy is the use of electromagnetic radiation to gain information about the structural or dynamical properties of molecules. Absorption of an incoming photon with frequency ν_{mn} will cause a transition from an initial energy state E_m to a higher energy state E_n according to the following relation:

$$\nu_{mn} = \frac{E_n - E_m}{h}, \tag{1.1}$$

where h is the Planck constant. Because energy levels are quantised in molecules, only certain frequencies matching the energy difference between the two states will be absorbed, giving rise to absorption lines. The whole set of absorption lines plotted as a function of wavelength is called an absorption spectrum.

1.2. Molecular absorption

The Born-Oppenheimer approximation is the framework through which we understand molecular absorption and the absorption spectrum of molecules. The approximation is based on the fact that electron masses m are much smaller than nuclear masses M by a factor 10^4, allowing electrons to move on a time scale that is about two orders of magnitude shorter than that of nuclei:

$$\frac{v_e}{v_n} = \sqrt{\frac{M}{m}} \sim 100, \tag{1.2}$$

where v_e and v_n are the velocities of the electrons and nuclei respectively. The electron cloud will therefore adapt instantaneously to any motions set by the nuclei, such as vibrational and rotational motions. This way the motions of the electrons and the nuclei can be separated and the total energy E of the molecule be calculated from its electronic and nuclear energies respectively:

$$E = E_e + E_{vib} + E_{rot}, \tag{1.3}$$

where E_e is the electronic energy, E_{vib} is the vibrational energy, E_{rot} is the rotational energy. Each energy term being smaller than the former, the quantisation of energy states will also be different according to the type of motion involved: the rotational energy levels will be more compact than the vibrational levels, which themselves will be more compact than electronic energy levels, and the energy of the photons involved in the respective transitions will be smaller and smaller accordingly. The result is that different wavelength bands will be associated with different types of dominant transitions (see Table 1.I).

Table 1.I. Wavelength bands and associated dominant transitions

Dominant transition	Bands	Wavelength
Electronic	Visible, UV	$\lambda < 1\mu\text{m}$
Vibrational	Near IR	$1\mu\text{m} < \lambda < 20\mu\text{m}$
Rotational	Far IR, microwave	$\lambda > 20\mu\text{m}$

Consequently radiation absorbed by molecules at near infrared wavelengths will be transferred to dominant vibrational motions when the frequency of the incoming radiation matches the resonant vibrational frequency. There are $3N-6$ fundamental vibrational modes for a molecule consisting of N atoms, or $3N-5$ for a linear molecule. The fundamental vibration modes are chosen to be orthogonal so that vibrational motions can be described as a superposition of normal modes. The various stretching and bending modes for the linear acetylene molecule are illustrated in Table 1.II [10].

However it must be pointed out that not all these fundamental modes will absorb incoming radiation. Only vibrational modes that result in a *change* of the dipole moment of the molecule will be radiation sensitive [11]. Similarly an infrared rotational spectrum can only occur if the molecule has a permanent dipole moment, which is not the case for linear and symmetric molecules or for homonuclear molecules such as H_2, N_2, and O_2. For the latter case, the symmetry properties of the molecules forbid any rotational or vibrational infrared activity and the molecules are basically transparent in the whole infrared region of the spectrum [11].

As previously seen, absorption in the near infrared region of the spectrum is associated with

Table 1.II. Fundamental vibrational modes of acetylene

Mode	Frequency	Description	Geometry
ν_1	$3373\,\mathrm{cm}^{-1}$	Symmetric C - H stretch	$\overleftarrow{\mathrm{H}} - \mathrm{C} \equiv \mathrm{C} - \overrightarrow{\mathrm{H}}$
ν_2	$1974\,\mathrm{cm}^{-1}$	Symmetric C - C stretch	$\mathrm{H} - \overleftarrow{\mathrm{C}} \equiv \overrightarrow{\mathrm{C}} - \mathrm{H}$
ν_3	$3295\,\mathrm{cm}^{-1}$	Asymmetric C - H stretch	$\overleftarrow{\mathrm{H}} - \mathrm{C} \equiv \mathrm{C} - \overleftarrow{\mathrm{H}}$
ν_4	$613\,\mathrm{cm}^{-1}$	Symmetric bend	$\overset{\uparrow}{\mathrm{H}} - \underset{\downarrow}{\mathrm{C}} \equiv \overset{\uparrow}{\mathrm{C}} - \underset{\downarrow}{\mathrm{H}} \quad \overset{\odot}{\mathrm{H}} - \underset{\otimes}{\mathrm{C}} \equiv \overset{\odot}{\mathrm{C}} - \underset{\otimes}{\mathrm{H}}$
ν_5	$730\,\mathrm{cm}^{-1}$	Asymmetric bend	$\overset{\uparrow}{\mathrm{H}} - \underset{\downarrow}{\mathrm{C}} \equiv \underset{\downarrow}{\mathrm{C}} - \overset{\uparrow}{\mathrm{H}} \quad \overset{\odot}{\mathrm{H}} - \underset{\otimes}{\mathrm{C}} \equiv \underset{\otimes}{\mathrm{C}} - \overset{\odot}{\mathrm{H}}$

vibrational transitions, however individual vibrational motions are usually accompanied by rotational motions. The total energy of the combined transitions slightly increasing (or decreasing) as

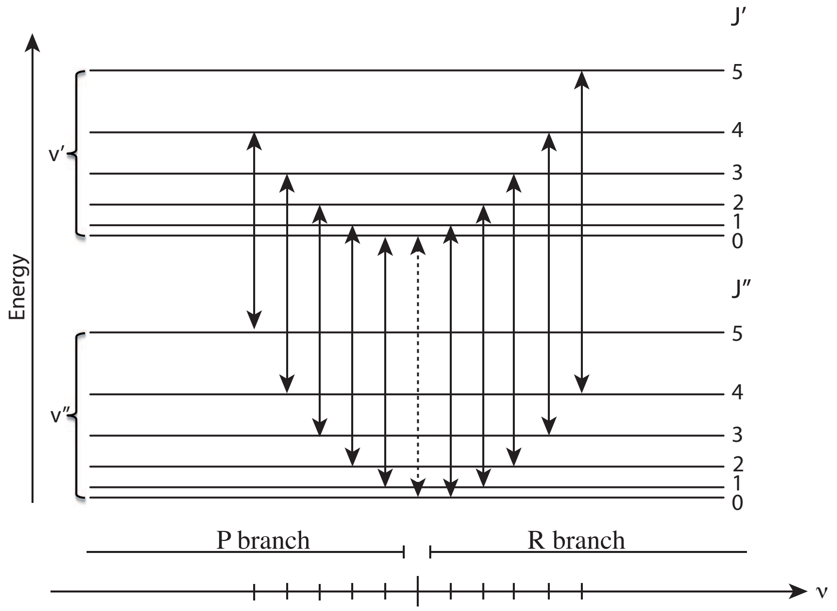

Figure 1.1. Rotational vibrational transitions and their relative positions in the spectrum. The ground vibrational state $v'' = 0$ and the first excited vibrational state $v' = 1$ are shown with their respective fine structure corresponding to rotational states labelled using the rotational quantum number J.

a function of the rotational energy states involved, the effect is to split one vibrational line into a set of discrete lines to form a vibrational band [6] (see Fig. 1.1).

1.3. The lineshape function

When examined under high resolution (R $\sim$ 0.01nm), individual absorption lines are seen as having particular shapes, indicating that a continous set of frequencies can be absorbed for a given transition but with different absorption efficiencies. The absorption coefficient $\alpha_L(\nu)$ is defined as the absorption per unit length:

$$dI(\nu) = -\alpha_L(\nu)I(\nu)dz, \tag{1.4}$$

where $I(\nu)$ is the intensity of the incoming radiation and $dI(\nu)$ is the difference in intensity due an absorbing material with thickness dz. The solution to this simple differential equation is the Beer-Lambert law:

$$I(\nu) = I_0 \exp[-\alpha_L(\nu) \cdot L], \tag{1.5}$$

where L is the optical path length and I_0 is the intensity of the incoming radiation. The linear absorption coefficient $\alpha_L(\nu)$ depends on the density of absorbers and on the transition cross section $\sigma(\nu)$ of each absorbing molecule:

$$\alpha_L(\nu) = N \cdot \sigma(\nu). \tag{1.6}$$

The molecule density N (in $\mathrm{mol/cm^3}$) is related to the pressure P under the ideal gas law approximation:

$$N = N_L \frac{296}{T} P, \tag{1.7}$$

where T is the temperature of the gas and $N_L = 2.45 \cdot 10^{16}\,[\mathrm{mol/(mbar \cdot cm^3)}]$ is the Loschmidt number. The transition cross section $\sigma(\nu)$ is readily separated in two parts, the transition strength S and the lineshape function $g(\nu)$:

$$\sigma(\nu) = Sg(\nu). \tag{1.8}$$

The lineshape function $g(\nu)$ is normalised:

$$\int_0^\infty g(\nu)d\nu = 1, \tag{1.9}$$

and is centered about the resonance frequency ν_0. Its width is known as the transition linewidth $\Delta\nu$ and is usually defined as the full width at half the maximum value (FWHM) of $g(\nu)$. The value of the lineshape function at the resonance frequency is inversely proportional to the linewidth $\Delta\nu$, indicating that the absorption efficiency of each molecule will depend on any line broadening effect present in the system.

In contrast, the transition strength S is constant for each absorption line and can be calculated knowing the Einstein coefficient for absorption B_{mn} and the difference of population $N_n - N_m$ between levels $|n>$ and $|m>$:

$$S = h\nu_{mn} B_{mn} \frac{N_n - N_m}{N}. \tag{1.10}$$

Values of the transition strength S can be found in the database HITRAN (HIgh-resolution TRANsmission molecular absorption database) at a reference temperature of 296 K [7]. As an example, Fig. 1.2 shows the transition strengths for the $\lambda = 1.5\mu\mathrm{m}$ rotational-vibrational absorption band of acetylene gas conveniently positioned at telecommunication wavelengths.

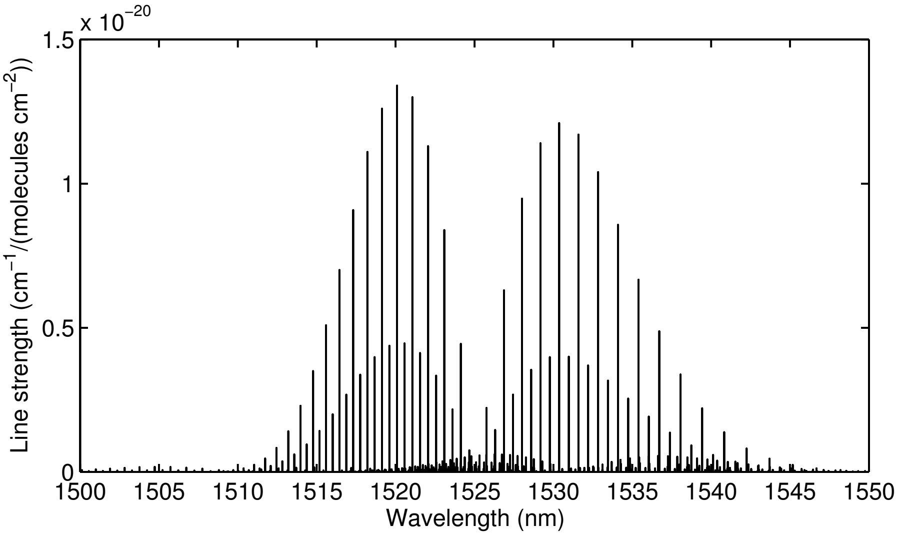

Figure 1.2. Line strengths S of the $\nu_1 + \nu_3$ ro-vibrational absorption band of acetylene at $\lambda = 1.5\mu\mathrm{m}$ (Hitran database). Each absorption line is related to a different rotational transition and rotational quantum number J. Several weaker sets of absorption lines can also be seen in the spectrum; they correspond to the so-called hot bands, where lower states are thermally excited states with population described by the Boltzmann distribution (Eq. 1.30).

1.4. Line broadening

This section presents various contributions to line broadening and their importance for high-resolution spectroscopy.

1.4.A. Lifetime broadening

Except for the lowest allowed energy level (*the ground state*), each energy level has a lifetime τ, which is the inverse of the rate Γ at which its population decays to all levels by either radiative or nonradiative process. With a mean lifetime τ_k on the excited state k, its energy E_k can only be determined within an uncertainty $\Delta E_i = \hbar/\tau_i$ as given by Einstein's uncertainty principle (see Fig. 1.3). The frequency between the two energy levels i and k shows therefore an uncertainty:

$$\Delta\nu = \frac{\Delta E_i + \Delta E_k}{h} = \frac{1}{2\pi}\left(\frac{1}{\tau_i} + \frac{1}{\tau_k}\right) = \frac{\Gamma}{2\pi}. \tag{1.11}$$

Linewidths due to spontaneous decay are typically in the kHz range for rovibrational transitions in the infrared and are much lower than other broadening effects because of the relatively long lifetimes of the energy levels involved. The lineshape function $g(\nu)$ associated with lifetime broadening is the Lorentzian function [8] but is seldom observed in practice.

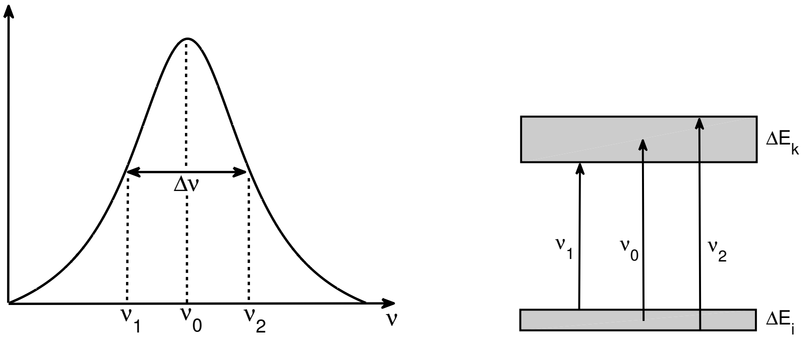

Figure 1.3. Typical line profile with associated energy levels. The gray area represents the energy uncertainty due to the finite lifetime of the energy levels.

1.4.B. Pressure broadening

Collisions involving energy exchange between molecules are called *inelastic collisions* and modify the lifetimes and decay rates considered above. The lifetime is limited by the mean free path between collisions, which is a function of the gas pressure P. The lineshape function is the Lorentzian profile:

$$g_L(\nu) = \frac{\Delta\nu_L/2\pi}{(\nu-\nu_0)^2+(\Delta\nu_L/2)^2}, \tag{1.12}$$

where $\Delta\nu_L$ is a function of the pressure broadening coefficient C_P:

$$\Delta\nu_L = C_P \cdot P. \tag{1.13}$$

Typical values of C_P for pure acetylene gas are $5-10$ MHz/mbars for ro-vibrational transitions near $\lambda = 1.55\,\mu\text{m}$. Pressure broadening accounts for the most important broadening effect at atmospheric pressure as linewidths of 5 GHz can be observed. In addition it severely limits the transition cross section per molecule σ:

$$\sigma(\nu_0) = S \cdot g_L(\nu_0) = \frac{2S}{\pi\Delta\nu_L} = \frac{2S}{\pi C_P \cdot P}. \tag{1.14}$$

Pressure broadening can be reduced in a gas absorption cell by using much lower filling pressures, with the added bonus of keeping the absorption coefficient α_L constant. This is due to two opposite effects: the absorption cross section of each molecule increases with reduced pressure while the total number of absorbing molecules decreases. There is however a minimal pressure value under which the linewidth cannot be decreased ($P \sim$ 50 torrs). In such cases the absorption line is said to be *Doppler-limited* because of the so-called Doppler broadening.

1.4.C. Doppler broadening

Another significant contribution to the spectral linewidth of gases is due to the thermal motion of molecules. At thermal equilibrium, the probability $p(v)dv$ of a molecule having a velocity between v and $v+dv$ is given by the Maxwellian distribution:

$$p(v)dv = \frac{1}{\sqrt{\pi}u}\exp\left(-\frac{v^2}{u^2}\right)dv, \tag{1.15}$$

where u is the most probable velocity. As a result of the Doppler effect, the resonance frequency ν_0 of a molecule moving at velocity v will correspond to an absorbing frequency ν_a:

$$\nu_a = \nu_0(1 \pm v/c) \tag{1.16}$$

in the rest frame of an observer, indicating that molecules moving at velocity v will absorb radiation at a frequency ν_a that is different from the resonance frequency ν_0. Inserting Eq. 1.16 in Eq. 1.15 with $dv = (c/\nu_0)d\nu_a$ the derivative of Eq. 1.16, the probability of a molecule absorbing the incoming radiation is:

$$p(\nu_a)d\nu_a = \frac{1}{\sqrt{\pi}\sigma_D} \exp\left(-\frac{(\nu_a - \nu_0)^2}{\sigma_D^2}\right) d\nu_a \tag{1.17}$$

and the lineshape function becomes:

$$g_D(\nu) = \frac{1}{\sqrt{\pi}\sigma_D} \exp\left(-\frac{(\nu - \nu_0)^2}{\sigma_D^2}\right), \tag{1.18}$$

where $\nu = \nu_a$ and σ_D is:

$$\sigma_D = u\nu_0/c = \frac{1}{\lambda}\sqrt{\frac{2k_BT}{M}}, \tag{1.19}$$

where c is the speed of light, λ is the wavelength, k_B is the Boltzmann constant, and M is the molecular weight. The full width at half-maximum (FWHM) of the Doppler profile is then:

$$\Delta\nu_D = 2\sqrt{\ln 2}\,\sigma_D = \frac{2\sqrt{\ln 2}}{\lambda}\sqrt{\frac{2k_BT}{M}}. \tag{1.20}$$

Typical full widths are ∼ 500 MHz for Doppler-broadened acetylene lines near $\lambda = 1.55\,\mu\text{m}$. However, spectral lines cannot be represented by Gaussian profiles at high pressure values since molecules moving with velocity v can absorb radiation at other frequencies than ν_a because of the Lorentzian-shaped absorption probability of each molecule. As illustrated in Fig. 1.4, the global lineshape function $g_V(\nu)$ of the spectral line is obtained by weighting each molecule with velocity v and Lorentzian profile $g_L(\nu - \nu_0 \cdot v/c)$ by the probability $p(v)$ of finding the molecule with velocity v:

$$g_V(\nu) = \int_{-\infty}^{+\infty} g_L(\nu - \nu_0 \cdot v/c)\, p(v)\, dv, \tag{1.21}$$

where $\nu_0(v/c)$ represents the Doppler shift. The resulting profile is called the Voigt profile is therefore a convolution of Lorentzian and Gaussian profiles [8].

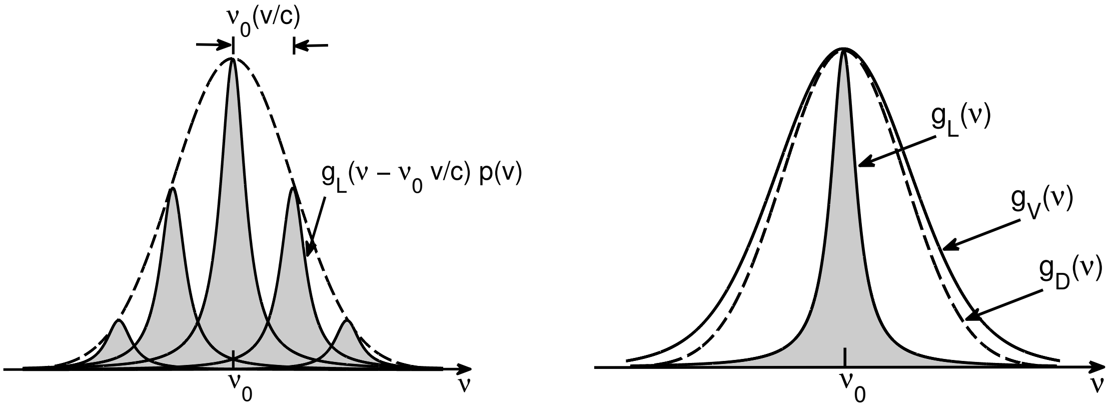

Figure 1.4. Voigt profile as a convolution of Lorentzian and Gaussian lineshapes. The left panel shows several Lorentzian profiles weighted by their respective probability $p(v)$ (dashed line). The right panel illustrates the difference in lineshapes between a Doppler-limited profile $g_D(\nu)$ and a Voigt profile $g_V(\nu)$ with a Lorentzian contribution $g_L(\nu)$ shown for molecules moving perpendicularly to the laser beam.

The FWHM of the Voigt profile $g_V(\nu)$ can be computed from:

$$\Delta\nu_V \approx 0.5346\Delta\nu_L + \sqrt{0.2166\Delta\nu_L^2 + \Delta\nu_G^2}. \tag{1.22}$$

Doppler broadening is inevitable in standard gas spectroscopy, however Doppler-free detection techniques such as saturated absorption spectroscopy can be used to access the narrow Lorentzian profile. The technique will be presented in §1.5.B.

1.4.D. Transit-time broadening

Another non-homogeneous contribution to line broadening is called transit-time broadening [1]. In evanescent-field spectroscopy, the interaction time of gas molecules with the optical field can be relatively small compared to the mean lifetime of excited levels. For such cases the energy E_k of the excited state will have an uncertainty ΔE_k that will depend on the time of flight of molecules through the optical beam. The resulting broadening is therefore a function of the most probable velocity $u = \sqrt{2k_B T/M}$:

$$\Delta\nu_{tt} = \frac{\sqrt{2\ln 2}}{2\pi}\frac{u}{w}, \tag{1.23}$$

where the quantity w is the Gaussian beam waist and represents the radius at which the field intensity of the optical beam reduces to $1/2e$ of its maximum value.

The contribution of transit-time broadening to the total linewidth can be significantly large in solid-core photonic crystal fibres due to the microscopic size of the air holes. The evanescent-field beam waist being often as small as 0.4 μm, transit-time broadening can add a significant 200 MHz to the total homogeneous width.

1.4.E. Saturation broadening

Saturated spectroscopy techniques require strong optical beams to access the narrow Doppler-free spectral line. A strong monochromatic light with frequency ν will reduce the population of molecules on the lower state moving at velocity $v = c(\nu - \nu_0)$, creating a spectral hole in the velocity distribution. At sufficiently large optical intensities, the pumping rate becomes larger than the relaxation rate, and the transition is said to be *saturated.* Saturation broadening occurs because the probability of creating a spectral hole is larger at the line center than far from resonance: the saturation effect is stronger at the line center, and approaches zero in the line wings. Saturation broadening is homogeneous for all molecules and increases the total Lorentzian linewidth $\Delta\nu_L$ by a factor $\sqrt{1+I/I_S}$:

$$\Delta\nu_s = \Delta\nu_L(\sqrt{1+I/I_S}), \tag{1.24}$$

where I and I_S are the incident optical intensity and saturation intensity, respectively. The saturation intensity represents the optical intensity at which the pumping rate at the line center ν_0 equals the total relaxation rate Γ of the transition [3]. It is a function of the square of the dipole moment μ of the transition [2] :

$$I_s = \frac{\varepsilon_0 c\hbar^2\Gamma^2}{2\mu^2}. \tag{1.25}$$

1.5. Absorption Spectroscopy Techniques

Basically all absorption spectroscopy techniques rely on the following setup: a source, an absorbing sample, transmission optics, and a detector. Broadband sources and optical spectrum analysers (OSA) are used to measure optical absorption spectrum such as the one presented in Fig. 1.5. Detailed analysis of the absorption lines is however difficult to perform due to the limited resolution of the OSA (typically R = 0.01nm compared to FWHMs of 0.05nm). In this case tunable lasers are used to measure individual absorption lines. All spectroscopy techniques presented in this section use distributed-feedback (DFB) laser diodes as they are very reliable, inexpensive, compact, and can be wavelength modulated very easily.

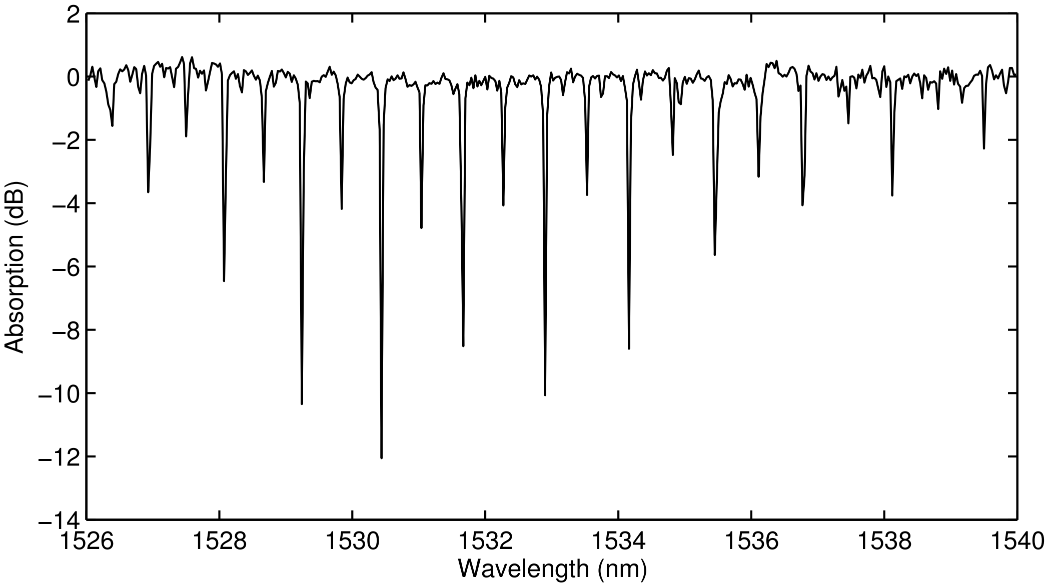

Figure 1.5. Absorption spectrum of acetylene measured at $\lambda = 1.5\mu\mathrm{m}$ with a high-resolution OSA. The amplified spontaneous emission (ASE) of an erbium-doped fibre amplifier (EDFA) was used as broadband source.

1.5.A. Tunable Diode Laser Absorption Spectroscopy (TDLAS)

In TDLAS measurements the emission line of a tunable laser diode is tuned over an absorption feature of a gas of interest. There are two ways of modulating the emission wavelength of a DFB laser diode. Coarse tuning is obtained by adjusting the temperature of the semiconductor material, which in turn modify the refractive index of the material and change the physical length of the laser cavity due to thermal expansion and contraction. The tuning range is over 1-2 nm and is restricted to tuning rates of a few hertz due to the thermal inertia of the system. Finer tuning and adequate tuning rates are obtained by changing the driving current of the diode, thereby modifying the material temperature due to a change in its resistive properties. This process is known as

Joule heating and shows a second-power dependence on the injection current. Joule heating is caused by interactions between free carriers and semiconductor ions. As the injection current increases, electrons impart more kinetic energy to the ions which gain vibrational energy and rise the temperature of the semiconductor. In addition the injection current modifies the refractive index of the material through an increase of free carriers, with an opposite but weak effect on the refractive index. Increasing the driving current will globally increase the refractive index and shift the emission line to longer wavelengths. Fine wavelength tuning over 0.1-0.5 nm is obtained with tuning rates as high as 1 GHz.

Quantitative information is obtained using the Beer-Lambert law, enabling direct concentrations of gas to be measured. The calibration of the Beer-Lambert law must however be performed by obtaining individual absorption lines for several known acetylene pressures (see Fig. 1.6). These absorption lines were obtained by approaching an optical fibre ~3 mm from a large-area detector placed inside a gas chamber. Air was evacuated using a vacuum pump before filling the chamber with gas and a pressure gauge monitored the pressure conditions. Values of the lineshape function

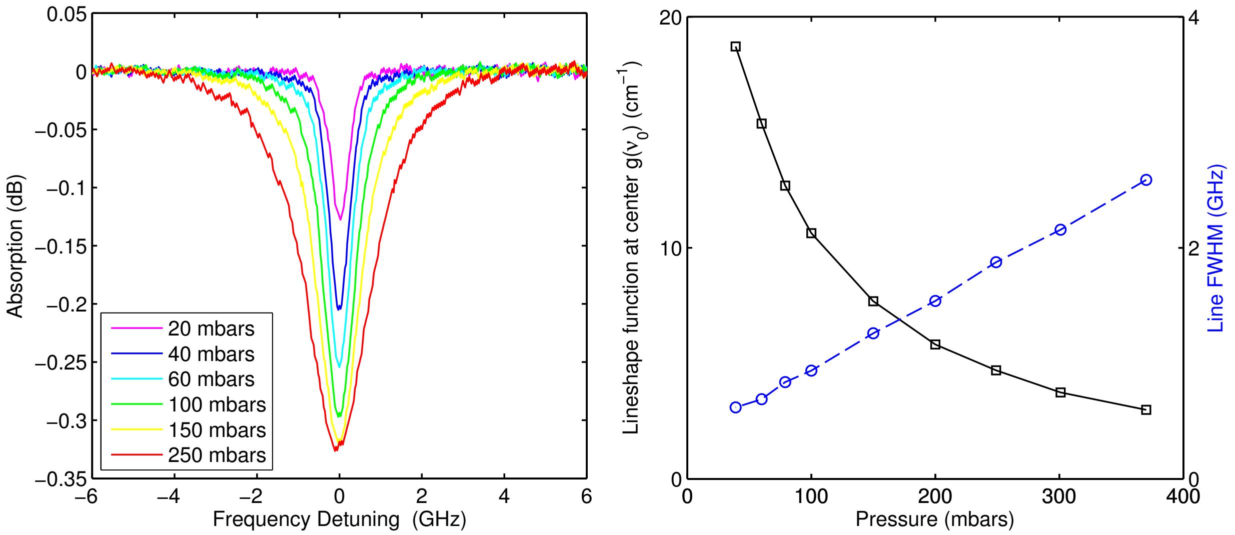

Figure 1.6. Left panel: absorption lines measured for various acetylene gas pressures ($\lambda = 1534.1\,\mathrm{nm}$). The saturation in absorption efficiency is visible for pressures values higher than 150 mbars. Right panel: the lineshape function, which represents the absorption cross section of each molecule, and the absorption linewidth are strongly dependent on the gas pressure.

were computed according to Eq. 1.5, 1.7, and 1.8 knowing the optical interaction length, the gas pressure, the strength of the absorption line, and the number of molecules in a given volume for an ideal gas. Absorption linewidths can also be used to obtain quantitative values of the pressure, however all broadening effects must be considered and calculated before using Eq. 1.22. One can also perform a calibration and obtain a figure such as the left panel of Fig. 1.6, where the value of lineshape function at line center and the line FWMHs are plotted as a function of the gas pressure.

Figure 1.6 also illustrates the working principle of absorption cells and their typical low filling pressures. As the pressure in the gas cell is increased, the number of absorbers is increased but the absorption cross section is decreased according to Eq. 1.14 in §1.4.B. There is thus a maximal pressure value above which there is no additional gain in absorption efficiency ($P \sim 150$ mbars). An additional pressure increase would merely lead to larger absorption widths and to a decrease in wavelength accuracy, hence the low filling pressures of absorption cells.

1.5.B. Saturated Absorption Spectroscopy (SAS)

Saturated absorption spectroscopy is an advanced technique used to access narrow Doppler-free spectral lines. The technique requires strong optical beams to optically pump molecules to excited states, burning spectral holes in the ground-state population of molecules. A weak probe beam is counter-propagating at the same wavelength in the absorption cell to detect this hole using TDLAS. For sufficiently strong pump powers a dip will appear at the centre of the absorption line corresponding to molecules moving perpendicularly to the laser beams. Such dips are called *Lamb dips* after W.E. Lamb, who first described it theoretically. Lamb dips can also occur on the side of an absorption line, but the probe and pump wavelengths, propagating in opposite directions, must be positioned at mirror-image frequencies to target exactly the same molecules [4].

Saturation of molecular absorption occurs when the optical intensity of a pump beam is equal to the saturation intensity I_S. It is a function of both the dipole moment μ and the total relaxation rate Γ of the transition according to Eq. 1.25. The relaxation rate Γ is found from the half width at half maximum of the Lorentzian profile:

$$\frac{\Gamma}{2\pi} = \Delta\nu_L/2. \tag{1.26}$$

The transition dipole moment μ is found from absorption data through the Einstein coefficient for absorption B_{mn}. It represents the absorption probability in units of [$\mathrm{s}^2/\mathrm{kg}\cdot\mathrm{m}$]:

$$B_{mn} = \frac{2\pi^2}{3\varepsilon_0 h^2 c}\mu^2. \tag{1.27}$$

where h is the Planck constant and c is the speed of light in vacuum. The Einstein coefficient for absorption is also related to the transition strength through $S = h\nu_{mn} B_{mn} (N_n - N_m)/N$ so that with Eq. 1.8 & 1.19 the following relation can be obtained:

$$\mu^2 = \frac{3\varepsilon_0 \hbar u \alpha_L}{\sqrt{\pi}(N_n - N_m)}, \tag{1.28}$$

where the population difference in a unit volume $N_n - N_m$ is calculated using the Boltzman distribution:

$$N_n - N_m = N_n \left[1 - \exp\left(-\frac{h\nu_{mn}}{k_B T}\right)\right]. \tag{1.29}$$

The population N_n on the lower level $|n>$ is:

$$N_n = \frac{N g_n}{Z} \exp\left(-\varepsilon_n hc/k_B T\right), \tag{1.30}$$

where g_n is the statistical weight for the lower level $|n>$, Z is the total internal partition function at $T = 296K$, and ε_n is the lower state energy in cm^{-1}. All three parameters can be found in HITRAN [7]. The numerical value of $(N_n - N_m)/N = \Delta\eta$ is $\sim$ 2 % for the P14 acetylene absorption line, indicating that only a very few number of molecules can actually absorb the incoming radiation. Using the ideal gas law, Eq. 1.28 is modified to:

$$\mu^2 = \frac{3\varepsilon_0 \hbar u}{\sqrt{\pi}} \frac{k_B T}{\Delta\eta} \frac{\alpha_L}{P}, \tag{1.31}$$

where P is the gas pressure inside the absorption cell. Using linear absorption data the transition dipole moment of the P14 line was estimated to:

$$\mu = 7.28 \cdot 10^{-33}\,\mathrm{C}\cdot\mathrm{m} = 4.55 \cdot 10^{-4} e \cdot \mathrm{\mathring{A}}. \tag{1.32}$$

The saturation intensity is therefore:

$$I_S = 0.011\,[\Delta\nu_L/2]^2\ \mathrm{mW}/\mu\mathrm{m}^2 = 9.26\,\mathrm{mW}/\mu\mathrm{m}^2. \tag{1.33}$$

for a Lorentzian linewidth $\Delta\nu_L$ of 58 MHz (see Appendix I for the computation of $\Delta\nu_L$). It is then straightforward to calculate the saturation power from the beam waist w:

$$P_S = \pi w^2 \cdot 9.26\,\mathrm{mW}/\mu\mathrm{m}^2. \tag{1.34}$$

As an example a theoretical saturation power of 410 mW is obtained for a beam waist of 3.75 μm in 5-mbars acetylene-filled hollow-core fibres. Such pump powers are easily achievable using erbium-doped fibre amplifiers (EDFA).

To test the technique an experimental setup was built according to Fig. 1.7. First absorption cells were prepared using hollow-core photonic crystal fibres (PCFs), which will be described in details in Chapter 2. They were prepared by filling acetylene gas at a very low pressure inside the fibre holes to minimise pressure broadening. The fibre gas cells are hermetically sealed to standard silica fibres using a standard electric-arc fusion splicer. Light from a DFB laser diode is separated in two parts which are propagating in opposite directions in the fibre gas cell. Two polarisation

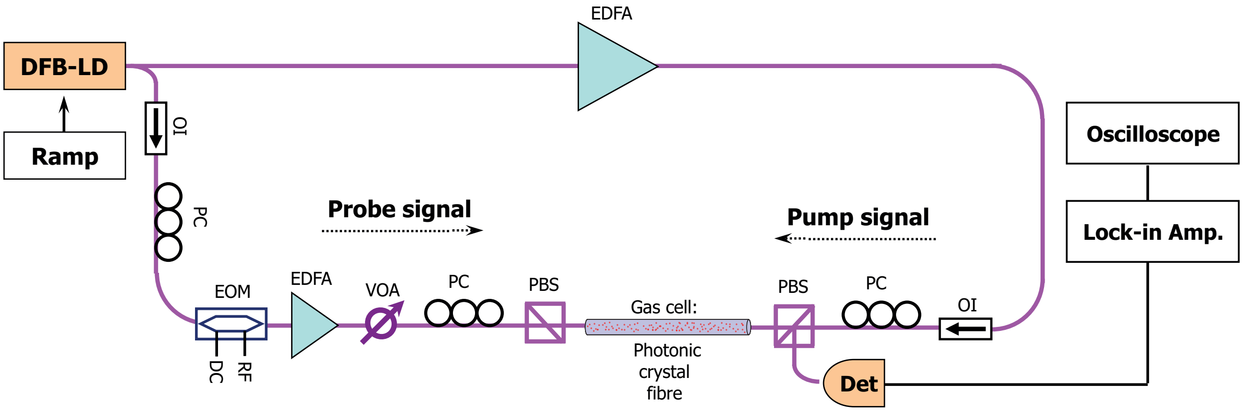

Figure 1.7. Experimental configuration of the SAS experiment. Pump and probe signals are counterpropagating along distinct polarisations in the fibre absorption cell. Lock-in detection is performed to acquire clean signals.

beam splitters (PBS) and three polarisation controllers (PC) are used to make the pump and probe beams propagate along distinct polarisations to minimise interferences between the probe beam and the reflected pump light. An electrooptic modulator (EOM) connected to a lock-in amplifier is used to further reduce the noise figure, followed by a small-power EDFA to account for the various power losses in the setup.

Experimental saturated absorption profiles are shown in Fig. 1.8 for several pump powers and clearly show Lamb dips for optical pump powers of ~450mW, agreeing with the theoretical saturation power of 410 mW. Saturated absorption profiles monitored by a probe signal follow the Gaussian lineshape multiplied by an inverted Lorentzian profile:

$$10 \cdot \log I_0(\nu) = A_G \exp\left(-\frac{(\nu-\nu_0)^2}{\Delta\nu_D^2/4\ln 2}\right)\left[1 - A_L \frac{\Delta\nu_s/2}{(\nu-\nu_0)^2+(\Delta\nu_s/2)^2}\right], \tag{1.35}$$

where the homogeneous width of the saturation feature $\Delta\nu_s$ is:

$$\Delta\nu_s = 0.5\Delta\nu_L\left[1+\sqrt{1+I/I_S}\right], \tag{1.36}$$

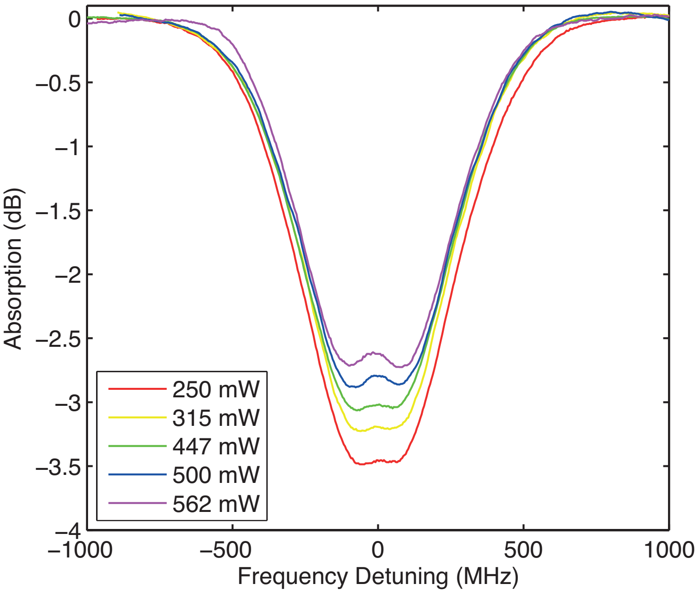

Figure 1.8. Lamb dips obtained for several pump power values (λ=1533.46nm). The theoretical saturation power of 410 mW agrees well with the experimental values needed to saturate the acetylene vibration transition.

corresponding to the sum of the half widths of the probe and pump beams equal to $\Delta\nu_L/2$ and $\Delta\nu_L\sqrt{1+I/I_S}/2$, respectively [1, 12]. The different contributions to the homogeneous width of the saturation dip are identified in Appendix I for a pump power of 500 mW. The theoretical saturated Lorentzian width is 72 MHz and agrees well with the experimental dip width of 71 ± 1 MHz.

The Doppler broadened background shown in Fig. 1.8 can be eliminated to perform Doppler-free spectroscopy. This is done by modulating the intensity of the pump beam and monitoring the transmitted intensity of the probe beam using a lock-in amplifier tuned to the modulated pump frequency. The experimental configuration should however be designed to prevent the detection of the pump signal that is reflected at the fibre gas cell interfaces and co-propagating with the probe signal.

1.5.C. Wavelength Modulated Spectroscopy (WMS)

This is an advanced technique used to monitor trace gases and weak absorptions as it enhances the detection limit. It is essentially an improvement to the TDLAS technique, where the injection current of laser diodes was modulated using a ramp signal to sweep the laser frequency across the absorption feature. In WMS a sinusoidal modulation is added to the ramp signal at a frequency of a few kHz. Light collected after the absorbing sample is then sent to a lock-in amplifier to extract the

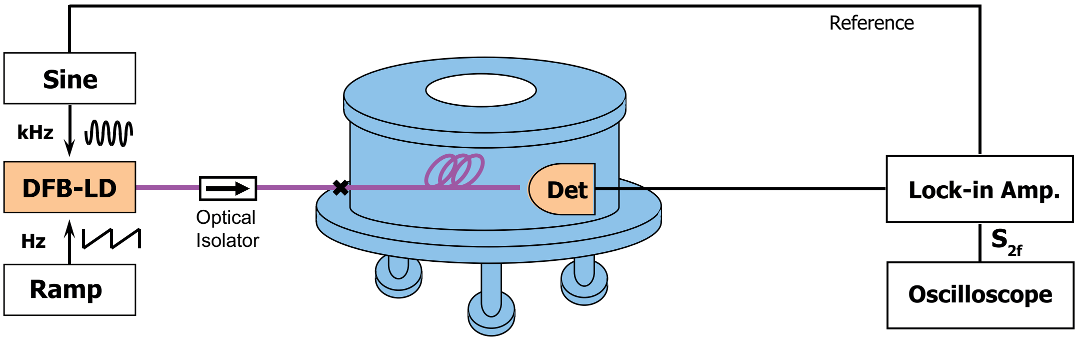

Figure 1.9. Experimental configuration of the WMS technique where a 2-kHz sine modulation is added to a 5-Hz ramp signal. A weak absorption line is obtained by filling a vacuum chamber with 7 mbars of acetylene gas (T=98.5%). A lock-in amplifier tuned to the sine modulation frequency extracts the second harmonic signal which is observed using an oscilloscope.

second harmonic signal. The output is observed on an oscilloscope and acquired with a computer.

The effect of adding a sinusoidal modulation in the kHz range is twofold. First it enhances the detection limit, because weak absorption causes very small changes in a background signal and the technique only monitors intensity changes for a given modulation frequency, resulting in a supressed DC background signal. Second it reduces any low frequency noise due to the kHz detection regime. A typical experimental setup is illustrated in Fig. 1.9. To test the technique the output of an SMF was placed only 3 mm from a large-area detector placed inside a vacuum chamber and 7 mbars of acetylene gas was introduced inside the chamber to obtain a weak absorption line (T=98.5%). The frequency reference for the lock-in amplifier was provided by a kHz frequency generator. The amplitude of the sinusoidal modulation was then varied from 2 mV to 40 mV and second-harmonic signals were acquired using the oscilloscope.

The global signal detected by the photodiode will be a function of the derivatives of the absorption line since basically the frequency modulation is translated to intensity modulation by the absorption feature (by its slope for the first-harmonic signal). The intensity of the detected radiation at a wavelength position λ_0 on the ramp signal can be described by:

$$I(t) = I(\lambda_0 + \Delta\lambda \cos \omega_m t), \tag{1.37}$$

where ω_m is the modulation frequency and $\Delta\lambda$ is the wavelength modulation index. Keeping $\Delta\lambda \ll$ HWHM for small modulation indices, Eq. 1.37 can be expanded in a Taylor series:

$$I(t) = I(\lambda_0) + I^{(1)}(\lambda_0)(\lambda - \lambda_0) + \frac{I^{(2)}(\lambda_0)}{2!}(\lambda - \lambda_0)^2 + \frac{I^{(3)}(\lambda_0)}{3!}(\lambda - \lambda_0)^3 + ... \tag{1.38}$$

where $I^{(n)}(\lambda_0)$ is the n$^{\text{th}}$ derivative of the unmodulated signal. Using 1.37 one gets:

$$I(t) = I(\lambda_0) + I^{(1)}(\lambda_0)\Delta\lambda \cos \omega_m t + \frac{I^{(2)}(\lambda_0)}{2!}(\Delta\lambda \cos \omega_m t)^2 + \frac{I^{(3)}(\lambda_0)}{3!}(\Delta\lambda \cos \omega_m t)^3 + ... \tag{1.39}$$

By using trigonometrical relations such as:

$$\cos^2(\omega_m t) = \frac{1 + \cos 2\omega_m t}{2}\ ,\ \cos^3(\omega_m t) = \frac{3 \cos \omega_m t + \cos 3\omega_m t}{4} \tag{1.40}$$

and by rearranging terms, it follows:

$$\begin{aligned} I(t) = & \left[I(\lambda_0) + \frac{I^{(2)}(\lambda_0)}{2 \cdot 2!} \Delta\lambda^2 + \frac{I^{(4)}(\lambda_0)}{8/3 \cdot 4!} \Delta\lambda^4 + ... \right] \\ & + \left[I^{(1)}(\lambda_0)\Delta\lambda + \frac{I^{(3)}(\lambda_0)}{4/3 \cdot 3!} \Delta\lambda^3 + ... \right] \cos\omega_m t \\ & + \left[\frac{I^{(2)}(\lambda_0)}{2 \cdot 2!} \Delta\lambda^2 + \frac{I^{(4)}(\lambda_0)}{2 \cdot 4!} \Delta\lambda^4 + ... \right] \cos 2\omega_m t + ... \end{aligned} \tag{1.41}$$

where terms within square brackets represent harmonic signals. The higher order terms can be neglected as $\Delta\lambda \ll$ HWHM:

$$\begin{aligned} I(\lambda) &= I(\lambda_0) + I^{(1)}(\lambda_0)\Delta\lambda \cos\omega_m t + \frac{I^{(2)}(\lambda_0)}{2 \cdot 2!}\Delta\lambda^2 \cos 2\omega_m t + ... \\ &= S_{DC}(\lambda_0) + S_{1f}(\lambda_0) \cos\omega_m t + S_{2f}(\lambda_0) \cos 2\omega_m t + ... \end{aligned} \tag{1.42}$$

where λ_0 is the wavelength position on the ramp signal and S_{nf} is the n$^{\text{th}}$ harmonic signal. This technique is thus also known as derivative spectroscopy, because the n$^{\text{th}}$ harmonic signal is proportional to the n$^{\text{th}}$ derivative of the absorption line for small modulation indices [13].

To get quantitative information about the gas concentration the 2$^{\text{nd}}$ harmonic signal is usually used, because the signal is stronger at this harmonic and also because several standard lock-in amplifiers cannot directly operate at higher harmonics. In the weak absorption limit $I(\nu) = I_0(\nu)\exp[-\alpha(\nu)L] \simeq I_0(\nu)[1-\alpha(\nu)]$, so that the second derivative $I^{(2)}$ of the signal reduces to the second derivative of the absorption coefficient when the background intensity I_0 is constant with frequency. This is typically not the case, as amplitude modulation is usually associated with wavelength modulation, resulting in a sloping background of the direct absorption signal:

$$I(\nu) = I_0(\nu)[1-\alpha(\nu)] = \bar{I_0}[1+s(\nu)][1-\alpha(\nu)] \tag{1.43}$$

The effect of the sloping background will be to add an asymmetry of the 2$^{\text{nd}}$ derivative shape in the 2$^{\text{nd}}$ harmonic signal, shifting the position of its maximum value with respect to the line centre [5]. Fortunately this effect is negligible as it modifies the obtained maximum value of the 2$^{\text{nd}}$ harmonic signal by a few percent only [9].

The left panel of Fig.1.10 shows the second-harmonic signal $S_{2f}(\lambda_0)$ as a function of the frequency

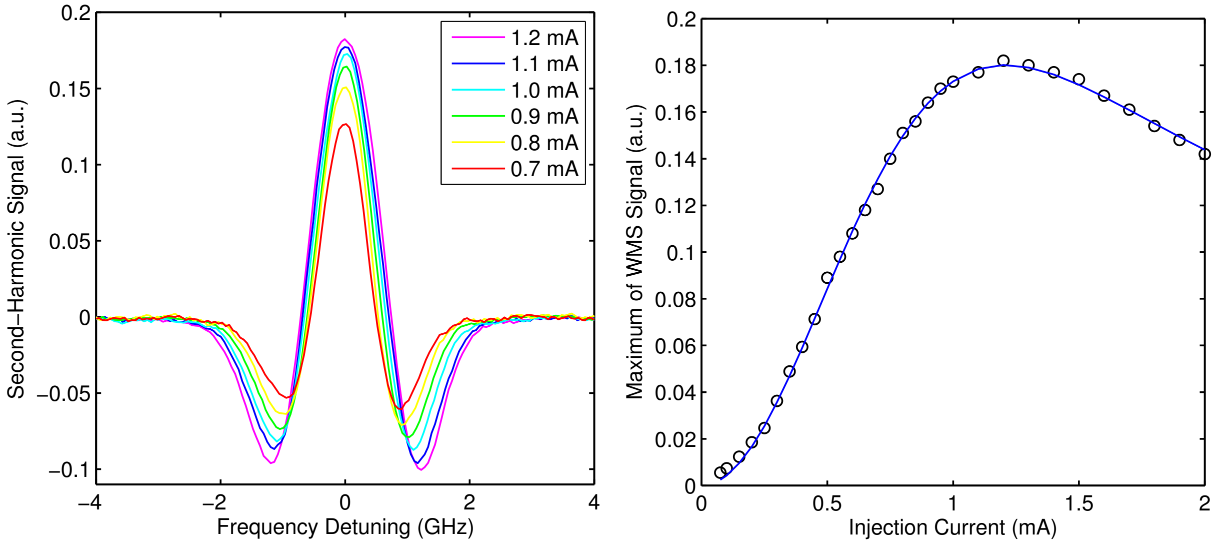

Figure 1.10. Wavelength Modulated Spectroscopy (P15 line, $\lambda = 1534.1\,\mathrm{nm}$). Left panel: second-harmonic signals as a function of the frequency detuning for several modulation indices (represented here in units of injection current). Right panel: amplitude of the second-harmonic signal S_{2f} as a function of the driving current of the sine modulation.

detuning for several modulation indices, and indeed looks like the second derivative of an absorption line as discussed previously. The right panel of Fig.1.10 shows the maximum of the second-harmonic signal S_{2f} as a function of the driving current of the sine modulation. The blue curve represents the fitted amplitude for a Gaussian absorption line [13]:

$$S_{2f}(m) = D I_1(m^2 \ln 2/2) \exp\left(m^2 \ln 2/2\right), \tag{1.44}$$

where $I_1(x)$ is the first-order modified Bessel function and $m = \Delta\lambda/HWHM$ is the modulation index. By fitting this equation to the data presented in the second figure, two constants can be retrieved: one is the constant D in the equation above and the second one represents the relation between modulation indices and driving current. The constant D is proportional to the absorption coefficient α_0 at the line centre:

$$D \propto \bar{I_0} \alpha_0 L, \tag{1.45}$$

from which relative gas concentrations can be obtained. Fluctuations of the optical power will also affect D through the average optical intensity $\bar{I_0}$, this uncertainty is removed by dividing $S_{2f}(m)$ by S_{DC} as both signals are proportional to $\bar{I_0}$ [13].

The second constant represents the relation between the modulation index m and the driving current Δi:

$$m = \left(\frac{1}{\Delta\nu/2} \frac{\Delta f}{\Delta i} \right) \Delta i, \tag{1.46}$$

and is proportional to the current tuning rate $\Delta f/\Delta i$. Knowing the half-width of the absorption line $\Delta\nu/2$, the current tuning rate corresponding to a modulation frequency of 1.869 kHz can be obtained:

$$\frac{\Delta f}{\Delta i} = 0.37\,\mathrm{GHz/mA}, \tag{1.47}$$

which is in the range of values expected for this modulation frequency according to Ref. [9].

References

[1] Bloembergen, N. and Shimoda, K. (1976). *High-resolution laser spectroscopy.* Springer-Verlag, Berlin.

[2] de Labachelerie, M., Nakagawa, K., and Ohtsu, M. (1994). Ultranarrow $^{13}C_2H_2$ saturated-absorption lines at 1.5 μm. *Opt. Lett.*, 19(11):840–842.

[3] Demtröder, W. (2008a). *Laser Spectroscopy: Vol. 1: Basic Principles.* Springer Berlin Heidelberg, 4th edition.

[4] Demtröder, W. (2008b). *Laser Spectroscopy: Vol. 2: Experimental Techniques.* Springer Berlin Heidelberg, 4th edition.

[5] Lucchesini, A., De Rosa, M., Pelliccia, D., Ciucci, A., Gabbanini, C., and Gozzini, S. (1996). Diode laser spectroscopy of overtone bands of acetylene. *Applied Physics B: Lasers and Optics*, 63:277–282.

[6] Petty, G. W. (2006). *A First Course in Atmospheric Radiation (2nd Ed.).* Sundog Publishing.

[7] Rothman, L. S., Gordon, I. E., Barbe, A., Benner, C., Bernath, P. F., Birk, M., Boudon, V., Brown, L. R., Campargue, A., Champion, J. P., Chance, K., Coudert, L. H., Dana, V., Devi, V. M., Fally, S., Flaud, J. M., Gamache, R. R., Goldman, A., Jacquemart, D., Kleiner, I., Lacome, N., Lafferty, W. J., Mandin, J. Y., Massie, S. T., Mikhailenko, S. N., Miller, C. E., Ahmadi, N. M., Naumenko, O. V., Nikitin, A. V., Orphal, J., Perevalov, V. I., Perrin, A., Cross, A. P., Rinsland, C. P., Rotger, M., Simecková, M., Smith, M. A. H., Sung, K., Tashkun, S. A., Tennyson, J., Toth, R. A., Vandaele, A. C., and Auwera, J. V. (2009). The HITRAN 2008 molecular spectroscopic database. *Journal of Quantitative Spectroscopy and Radiative Transfer*, 110(9-10).

[8] Saleh, B. E. A. and Teich, M. C. (2007). *Fundamentals of Photonics.* John Wiley & Sons, 2nd edition.

[9] Shilt, S. (2002). *Mesure de traces de gaz à l'aide de lasers à semi-conducteur.* PhD thesis, EPFL, Lausanne, Switzerland.

[10] Shoemaker, D. P., Garland, C. W., and Nibler, J. W. (1989). *Experiments in physical chemistry.* McGraw-Hill, New York, 5th edition.

[11] Steinfeld, J. I. (1974). *Molecules and radiation; an introduction to modern molecular spectroscopy.* Dover.

[12] Thapa, R., Knabe, K., Faheem, M., Naweed, A., Weaver, O. L., and Corwin, K. L. (2006). Saturated absorption spectroscopy of acetylene gas inside large-core photonic bandgap fiber. *Opt. Lett.*, 31(16):2489–2491.

[13] Uehara, K. (1998). Dependence of harmonic signals on sample-gas parameters in wavelength-modulation spectroscopy for precise absorption measurements. *Applied Physics B: Lasers and Optics*, 67:517–523.

CHAPTER 2

GAS SPECTROSCOPY USING PHOTONIC CRYSTAL FIBRES

2.1. Introduction

Thanks to their non-classical light guiding properties, photonic crystal fibre technology has brought a wealth of new applications to the well-established fibre optics domain. The motivation back in the 1990's was to fabricate an optical fibre with a guiding mechanism resembling photonic bandgaps and stop bands in periodic structures such as Bragg gratings, but to extend it in all directions. Moreover the interest in photonic crystal technology had already grown from the development of photonic crystals, which led to the identification of periodic microstructures as a powerful means of changing the transmission characteristics of a material. It took several years of technological development to fabricate the first successful silica-air PCF structure showing a photonic bandgap guidance mecanism [29].

2.2. Photonic crystal fibres

In photonic crystal fibres (PCFs) light is confined to the optical core by an array of small longitudinal air holes which define the cladding region [20]. PCFs are typically composed of a single material, usually pure silica glass to take advantage of its extremely high transparency at telecommunication wavelengths (λ=1.55 μm). PCFs are divided into two categories depending on their light-guidance mechanism.

There are index-guiding PCFs, where guidance occurs thanks to a modified form of total internal reflection, providing great flexibility in the design of the cladding region. Light propagates inside a solid core and an array of air holes provides the lower index material within the cladding region. The large refractive index contrast between glass and air combined with the micrometre scale of the cladding structure makes the effective indices strongly wavelength-dependent, leading to highly tailorable optical properties and a wealth of geometries. Several examples of such index-guiding fibres are illustrated in Fig. 2.1 (Fibres A, B, & C). Advantages of solid-core index-guiding PCFs include robustness, easy fabrication, and wide transmission bandwidths. Typical propagation losses for solid-core PCFs are 1 dB/m and are mostly due to fabrication-related imperfections [8, 22].

Improving the fabrication technique can lead to much better surface qualities and can decrease propagation losses down to 0.1 dB/m as reported in [8].

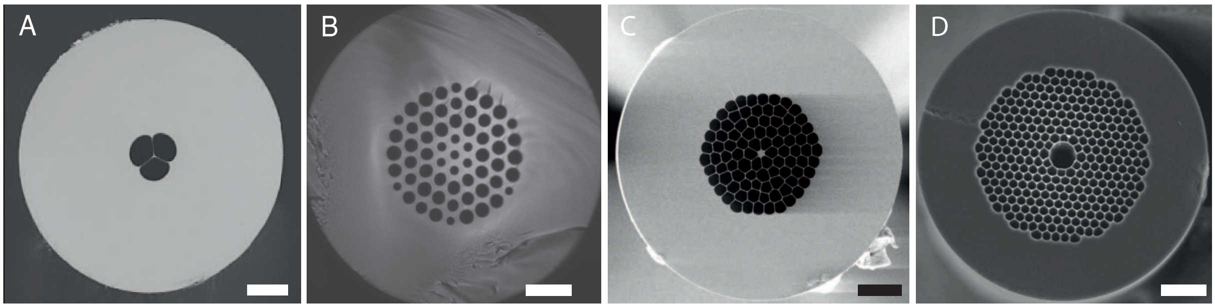

Figure 2.1. Several examples of photonic crystal fibres. Scale bars indicate 20 μm.

There are also photonic bandgap fibres (PBF), where guidance is ensured by a photonic bandgap effect arising from the wavelength-scale periodicity of the cladding region (see Fibre D [1] in Fig. 2.1). Photonic bandgap guiding results from the forbidden propagation inside the photonic lattice cladding, preventing lightwaves from lateraly escaping the optical core. The core index has no real impact on the guiding efficiency, so that guiding in air or in vacuum can be realised, provided sophisticated fabrication techniques and a careful design of the cladding region. The transmission in hollow-core fibres is only secured for narrow bandwidths (200nm), but with the benefit that propagation losses as low as 1dB/km can be obtained thanks to highly effective photonic bandgaps that can now be achieved [22].

PCF technology offers the possibility to fill the air holes with a given material to make light-matter interactions. Gas absorption spectroscopy is achieved via the evanescent optical field propagating in the holes of index-guiding fibres or via the optical field propagating in the hollow core of bandgap-guiding fibres. Their long interaction lengths and small sample volumes ($\sim 1\mu l$) result in more compact and effective gas cells than their conventional couterparts, with the added benefits of reliability and robustness in harsh environments, cost-effectiveness, and more.

The efficiency of an optical fibre for gas sensing purposes is described by the fraction of power located in the air holes. It is typically very low for solid-core holey fibres ($\sim$ 1%), but it can be increased via a careful design of the microstructured region. It has been shown that the overlap fraction increases with the d/Λ ratio, where d is the hole diameter and Λ is the pitch value [11]. In this respect air-suspended solid-core holey fibres (see Fibre D in Fig 2.1 [17]) perform well as this ratio is larger than 0.9, resulting in overlap fractions larger than 10 % [10]. This value can be further increased by decreasing the core dimensions down to subwavelength scales; a 500-nm core diameter offers slightly more than 50 % overlap at 1.55 μm [33]. However the core dimensions cannot be decreased arbitrarily due to roughness scattering [22]. As the core diameter is decreased to subwavelength dimensions, more light is guided outside the optical core as an evanescent wave and can be scattered by the glass-air interface, hence higher propagation losses. Single-mode propagation would be secured for such dimensions as the critical core diameter is 1.1 μm [31], but strong fusion splicing challenges would arise, making their implementation impractical.

---

[1] From BlazePhotonics Ltd, now NKT Photonics A/S

Another way to increase the amount of optical power located in the holes is to decrease the pitch value with respect to the operating wavelength, however increasing sharply confinement losses as the optical mode is more likely to spread over the cladding region and reach the outer cladding [12]. Confinement loss occurs because the fibre core and the outer cladding region extending beyond the microstructured cladding have the same refractive indices, leading to intrinsically leaky optical modes. Confinement losses can naturally be reduced by adding more layers of air holes [11, 35], but fabrication constraints along with gas filling time considerations (see §2.3) will eventually place a limit on the minimum pitch value and the maximum overlap attainable. In this respect hollow-core PCF are particularly attractive for evanescent-field applications as more than 99 % of the fundamental mode is propagating inside the hollow core [29].

Another great potential of hollow-core fibres is the possibility of extremely low propagation loss. Loss in hollow-core PCFs is nowadays limited by scattering at the glass-air interface due to surface roughness [8, 22]. However, with futher development of the fabrication process, it would theoretically be possible to reach attenuations values less than the 0.15 dB/km attenuation floor of conventional fibres. As the minimum attainable loss in standard silica fibres is due to Rayleigh scattering in the amorphous silica glass, hollow-core fibres can possibliy improve this figure, allowing for longer usable fibre lengths and reducing the need for optical amplifiers and repeaters.

2.3. Dynamics of gas diffusion inside photonic crystal fibres

In addition to the fraction of optical power available for sensing, the filling time is also an important parameter to consider when designing a fibre-based gas sensor since the microscopic size of the holes compared to the length of the fibre capillaries may lead to an endless gas progression along the fibre. Previous works monitored the gas filling process in hollow-core fibres using acetylene absorption lines and studied its dependence on fibre length [13, 16, 28]. Accurate expressions have been provided to predict the temporal response of a gas sensor, but proved to be quite inconvenient due to the non-analytical nature of the solutions [14]. This work aims at providing simple equations that can be applied to any type of fibre, fibre geometry or length. The model for the filling time is based on the theory of gas diffusion where approximations have been made to mitigate the complexity of the equations. The validity of these approximations is verified by analysing the gas filling dynamics in fibre samples of various geometries. Using this gas filling model, the filling time can be predicted for any given fibre geometry and length [7].

2.3.A. Theory of Gas Diffusion

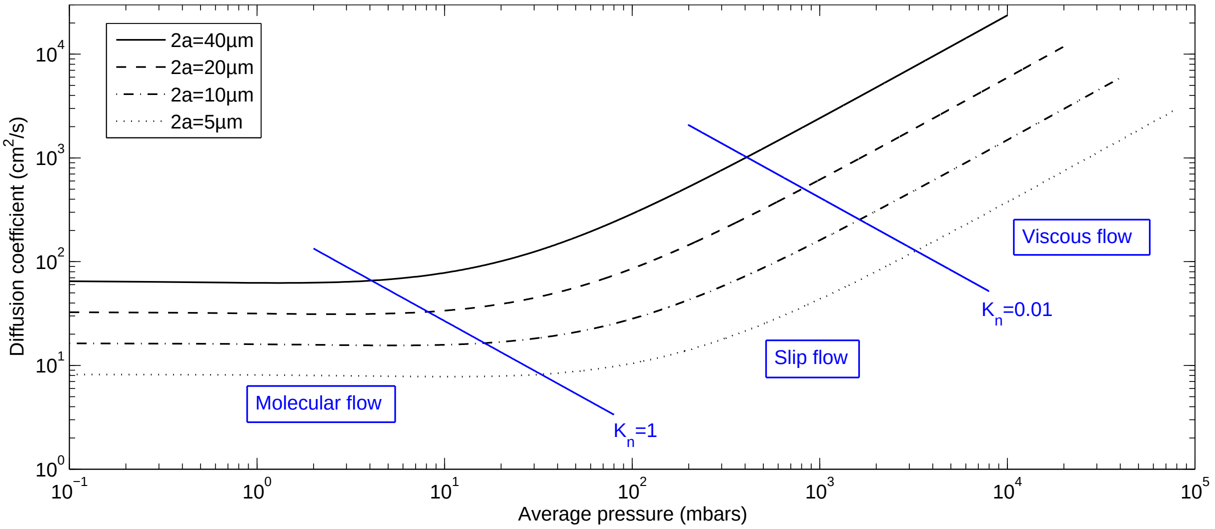

Figure 2.2. Calculated diffusion coefficients of acetylene gas for several capillary diameters. The various flow regimes are defined according to the two blue lines representing Knudsen numbers of 1 and 0.01 respectively.

This subsection presents the equations governing the diffusion of gas molecules inside capillaries.

We define the diffusive flux Φ as the amount of gas passing perpendicularly through a reference surface of unit area per unit time. It is directly a function of the gradient of the molecules density n at a position x:

$$\Phi = -D \frac{\partial n}{\partial x}, \tag{2.1}$$

where the proportionality constant D is the so-called diffusion coefficient. In addition, the conservation of mass during diffusion yields:

$$\frac{\partial n}{\partial t} = - \frac{\partial \Phi}{\partial x}. \tag{2.2}$$

The diffusive flux Φ and the diffusion coefficient D can be calculated; however, the nature of the flow being completely different according to the experimental conditions, the corresponding diffusion regime has to be identified (see Fig. 2.2). This is done by the means of a dimensionless parameter called the Knudsen number K_n, which is the mean free path λ of a molecule divided by the capillary radius a through which it is diffusing:

$$K_n = \lambda / a, \ \lambda = \frac{k_B T}{\sqrt{2}\pi \bar{P} \delta^2}, \tag{2.3}$$

where k_B is the Boltzmann constant, T is the temperature, P is the average pressure along the capillary and where the added bar sign indicates averaging over the filling time as well. Finally δ is the diameter of the gas molecule (334 pm for the acetylene molecule as defined in[14]).

2.3.A.1. Free Molecular Flow Regime

The low-pressure range of gas experiments is represented by large Knudsen numbers ($K_n > 1$) and the corresponding diffusion regime is called free molecular flow or simply molecular flow. In this regime, the gas molecules collide more frequently with the capillary walls than with other molecules. The molecular flux averaged over the cross section of the capillary is therefore determined by geometrical considerations:

$$\Phi_k = -\frac{2}{3} \frac{a \bar{v}}{k_B T} \frac{\partial p}{\partial x}, \tag{2.4}$$

where the mean molecular velocity $\bar{v}$ is function of both the temperature and the molecular mass m:

$$\bar{v} = \sqrt{\frac{8k_BT}{\pi m}}. \tag{2.5}$$

It is then straightforward to derive the diffusion coefficient for the free molecular flow regime D_k from its definition in Eq. 2.1:

$$D_k = \frac{2}{3}a\bar{v}. \tag{2.6}$$

As expected there is no pressure dependence of the diffusion coefficient D_k in the free molecular flow regime.

2.3.A.2. Hydrodynamic Flow Regime

On the other hand, small Knudsen numbers ($K_n < 0.01$) indicates that collisions between molecules occur more frequently than with the capillary walls, which is the case inside a PCF at atmospheric pressure down to a hole size of 16 μm. In this situation, the flow velocity is parabolic across the fibre hole and tends to be zero at the fibre walls due to frictional forces. The gas flow is then considered viscous and is governed by hydrodynamical equations. More specifically, the Poiseuille equation describes a laminar and incompressible flow in the viscous range:

$$\Phi_v = -\frac{a^2 n}{8\eta}\frac{\partial P}{\partial x}, \tag{2.7}$$

with η being the viscosity:

$$\eta = \frac{\bar{v}m}{2\sqrt{2}\pi\delta^2}. \tag{2.8}$$

The diffusion coefficient for the hydrodynamic flow regime is then obtained using Eq. 2.1:

$$D_v = \frac{a^2 P}{8\eta}. \tag{2.9}$$

The diffusion coefficient is therefore proportional to the pressure inside the capillary in the viscous flow regime.

2.3.A.3. Slip-Flow Regime

Between these two flow regimes is found a transition type of flow called slip flow showing characteristics of both viscous and molecular flows. As illustrated in Fig. 2.2, the extrapolation of the viscous flow curves into the lower part of the transition region underestimates the actual flow. The additional flow can be seen as gas slipping over the capillary walls: the flow velocity at the walls is no longer zero as in the viscous regime. The slip-flow transition region is unfortunately the operating regime for low-pressure absorption cells, and there are no analytical expressions describing this flow region, so we had to rely on semi-empirical relations.

The behaviour of the diffusive flux Φ as a function of pressure can be described using an empirical relation based on the Knudsen number scaling the flow additional to the extrapolated viscous flow Φ_v [5, 9]:

$$\Phi = \Phi_v + Z(K_n)\Phi_k. \tag{2.10}$$

The corresponding diffusion coefficient is:

$$D = \frac{a^2 P}{8\eta} + Z(K_n)\frac{2}{3}a\bar{v}, \tag{2.11}$$

where $Z(K_n)$ is:

$$Z = \frac{1+2.507(a/\lambda)}{1+3.095(a/\lambda)} = \frac{1+2.507/K_n}{1+3.095/K_n}. \tag{2.12}$$

This way, at low pressures, Z is close to unity and the pressure-dependent flow Φ_v goes to zero, resulting in the Knudsen flow Φ_k describing accurately the observed flow as we enter the free molecular flow regime. Reversely as pressure increases, the viscous flow Φ_v increases and the added flow becomes negligible.

By applying these equations to acetylene gas diffusing inside a microstructured fibre, the diffusion coefficient can be calculated for a given hole diameter and average pressure $\bar{P}$. This is done in Fig. 2.3 showing that the diffusion rate can be significantly improved by increasing the hole diameter.

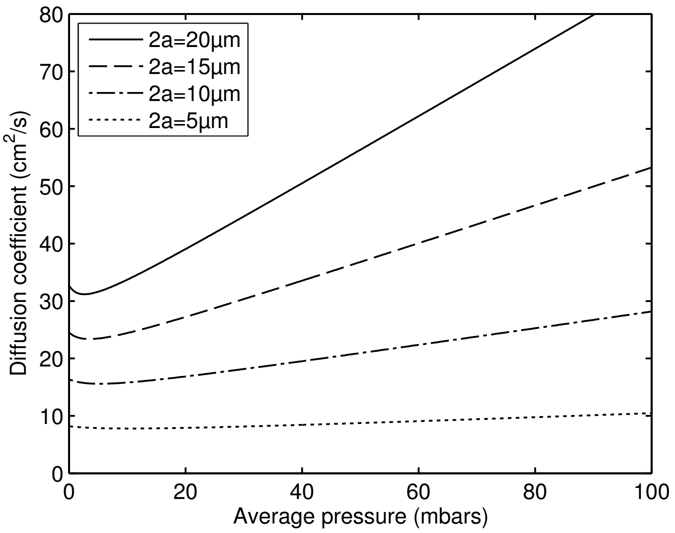

Figure 2.3. Calculated diffusion coefficient of acetylene gas for several hole diameters in the slip-flow regime according to Eq. 2.11 & 2.12.

2.3.B. Gas Filling Dynamics

The distribution of the molecules density n along the fibre length during the gas filling process is obtained by solving the two partial differential equations presented in section 2.3.A (Eq. 2.1 & 2.2). By integrating the corresponding normalised pressure distribution over the fibre length L, one can obtain [18]:

$$\frac{P(t)}{P_0} = 1 - \frac{8}{\pi^2} \sum_{j=1,3,5}^{\infty} \frac{1}{j^2} \exp\left[-\left(\frac{j\pi}{\xi L} \right)^2 D t \right], \tag{2.13}$$

where ξ is a geometrical factor depending on the filling conditions. It is equal to 2 for gas diffusing inside a fibre from one end and equal to unity for gas diffusing from both ends of the fibre. Moreover Eq. 2.13 is valid only if the diffusion coefficient is constant during the filling process, which is the case in the free molecular flow regime or for the special case of trace-gas diffusion inside air-filled cladding holes. The diffusion process being determined by the slip-flow regime for pure gas diffusing in vacuumed microstructured fibres, the diffusion coefficient is no longer constant. Instead of using numerical solutions to accurately describe the filling process [14], we will approximate the diffusion coefficient as being constant throughout the filling process and the parameter D in Eq. 2.13 will represent the averaged filling rate in any type of fibre for a given average pressure $\bar{P}$.

The filling time is here arbitrarily defined as the time required for the pressure P in the fibre to reach 85% of the equilibrium pressure P_0:

$$P = 85\% P_0. \tag{2.14}$$

This definition is justified by considering that typical fibre lengths can reach up to 20 m and that waiting for a complete gas filling would actually take an infinite time. The choice of 85% is therefore a compromise between time consumption and reasonable filling along the fibre. With the help of Eq. 2.13, the analytical model for the filling time t_{fill} of gaseous species inside PCFs is:

$$t_{fill} = \frac{(\xi L)^2}{\pi^2 D} \ln[\frac{\pi^2}{8} \times \frac{P_0}{P_0 - P}] \tag{2.15}$$

and can be applied to any fibre geometry or length. The diffusion coefficient is calculated using:

$$D = \frac{a^2 \bar{P}}{8\eta} + Z(K_n)\frac{2}{3}a\bar{v}, \tag{2.16}$$

with the help of Eq. 2.3, 2.5, 2.8 & 2.12 and the molecular mass equal to 26.04 g/mol for acetylene gas [34]. The average pressure is here defined as $\bar{P} = \frac{2}{3}P_0$ to take into account the exponential profile of the filling process as it increases the average pressure to more than just 50 % of the equilibrium pressure.

The comparison with experimental filling times is then performed by monitoring the gas filling process in various types of microstructured fibres. From an experimental point of view, the average pressure inside a fibre during gas filling can be retrieved by monitoring the decreasing intensity $I(t,\nu)$ of an absorption line as a function of time:

$$\frac{P(t)}{P_0} = \frac{\int \ln\left(I(t,\nu)/I_0(\nu)\right) d\nu}{\int \ln\left(I_{fill}(t_{fill},\nu)/I_0(\nu)\right) d\nu}. \tag{2.17}$$

This is done in the following experimental sections, where experimental and predicted filling times of several fibre samples are compared.

2.3.C. Experimental Procedure

First the fibre samples were spliced at one end to standard ITU-T G.652 single-mode fibres (SMFs) using an arc fusion splicer. A dispersion-compensating fibre (DCF) with a $\sim 4\ \mu$m core diameter was spliced between the SMFs and the small core PCFs to progressively match the mode field diameters. The typical splice loss between the SMFs and DCFs is 1dB compared to 2-3dB for splices between DCFs and PCFs. These concatenated fibres were then placed inside an hermetic gas chamber and vacuum was maintained for 4–8 days with the help of a turbo vacuum pump to let air evacuate the microstructured holes.

Acetylene gas was then introduced inside the chamber and the filling process was monitored using absorption lines in the $\nu_1 + \nu_3$ rotational-vibrational band of $^{12}C_2H_2$ centered at $\lambda = 1.526$ nm. The injection current of a distributed-feedback (DFB) laser diode was continuously modulated to sweep the laser line across the absorption line. The wavelength information was retrieved with a Burleigh WA-1000 wavemeter and a pressure gauge monitored the vacuum conditions inside the gas chamber.

2.3.D. Results and Analysis

This subsection presents the results of the gas filling experiments in the various fibre samples. The samples were chosen to cover various fibre geometries: an air-suspended silica core surrounded by three large cladding holes, a microstructured germanium-doped core with three added layers of cladding holes, and a pure silica core surrounded by five layers of holes (insets A, B, and C respectively in Fig. 2.4). For each fibre sample, the hole diameter is defined as the smallest diameter that can be inscribed inside a hole over which the optical field is significantly present. Figure 2.4 shows the filling process of acetylene gas inside the three fibre samples for a filling pressure of 77 mbars with the corresponding experimental filling times presented in Table 2.I.

Table 2.I. Characteristics of the microstructured fibres

Fibre (see Fig. 2.4)	Geometry	Length	Hole diameter	Predicted filling time	Experimental filling time	Accuracy
A	Suspended core	2.7 m	11.8 μm	35min	31min ± 5min	88 %
B	Microstructured core	5.4 m	3.4 μm	10h 06min	9h ± 1h	90 %
C	Solid core	9.2 m	5.4 μm	18h 12min	18h 36min ± 30min	97 %

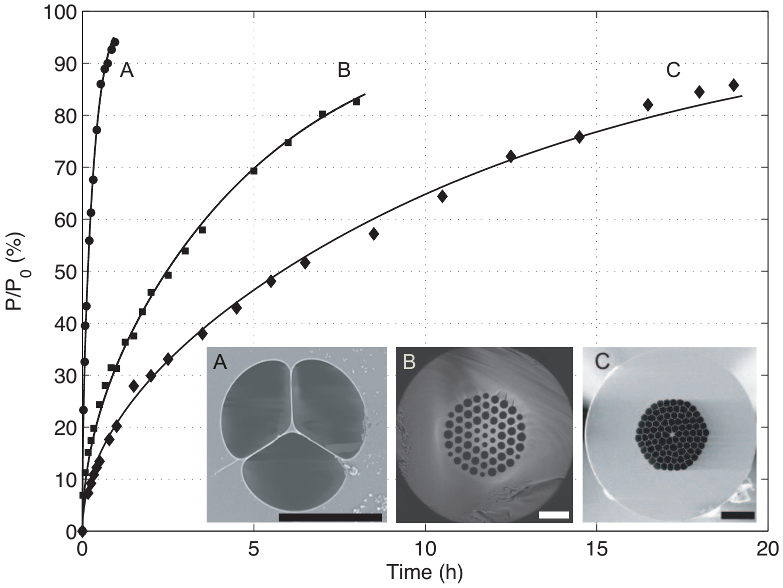

Figure 2.4. Filling process measured as a function of time in a suspended-core PCF (A), a microstructured-core PCF (B), and a solid-core PCF (C). The black curves represent nonlinear fittings of Eq. 2.13 from which experimental diffusion coefficients can be obtained. All scale bars represent 20 μm.

As seen in Table 2.I, the temporal response of a fibre gas sensor can be predicted for any fibre geometry with at least 85% accuracy using the simplified Eq. 2.15. Moreover, the relation between diffusion coefficient and pressure (i.e. Eq. 2.11) was verified by filling a given fibre sample (here a suspended-core fibre) at various filling pressures then retrieving experimental diffusion coefficients. As illustrated in Fig. 2.5, the experimentally determined values show reasonably satisfactory agreement with the calculated ones. However larger discrepancies can be seen for filling pressures higher than the useful 150 mbars determined in §1.5.A for absorption cells. This is due to the analytical model as the approximation for a constant diffusion coefficient is less accurate for higher pressures. Finally the uncertainty in the measured D values is due to normalisation difficulties related to the oscillating background pattern often seen in PCF spectra [15] combined with the difficulties in evaluating the equilibrium pressure P_0.

2.3.E. Ideal Gas Filling Conditions

In addition to being used as chemical sensors to detect hazardous gases, microstructured fibres can be filled with low-pressure gases to make all-fibre gas cells [3, 21]. As the linewidth of absorption

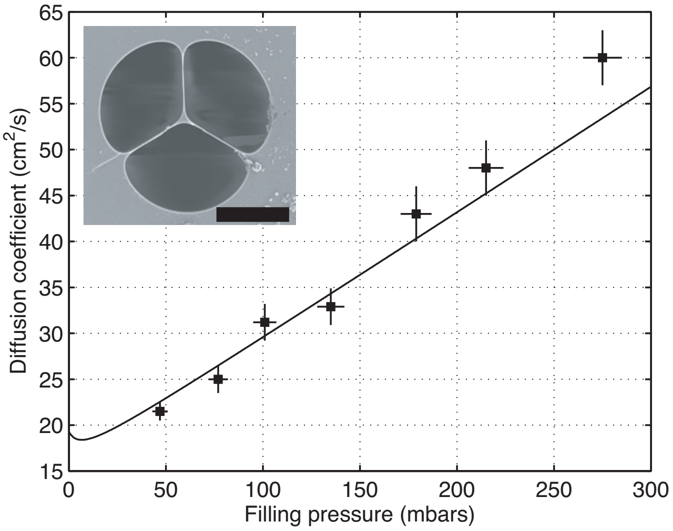

Figure 2.5. Experimental diffusion coefficients for acetylene gas diffusing in suspended-core fibres (hole diameter: 11.8 μm, scale bar: 10 μm) obtained using Eq. 2.11. The black curve represents diffusion coefficients calculated with average pressures taken as 2/3 of the filling pressures.

lines depends on gas pressure, the fibres usually contain pure gas at pressures less than 200 mbars to maintain high wavelength accuracy. However, when gas chambers or similar devices are used for filling the fibre cells, the gas pressure inside the chamber will increase with time due to three main factors: virtual or real leaks, outgassing of molecules at low pressure or backstreaming from the vacuum pump [25]. As a result, the gas leakage rate together with long filling times will introduce impurities into the gas cell. Figure 2.6 presents the predicted filling time of acetylene gas in microstructured fibres for a typical filling pressure of 100 mbars for any combination of hole diameter and fibre length.

The high wavelength accuracy of the gas cell is then secured by limiting the filling time according to a few selected criteria. The effect of impurities in the gas cell will be to increase the width of the absorption line $\Delta\nu_V$ via the Lorentzian absorption linewidth $\Delta\nu_L$ according to the empirical relation:

$$\Delta\nu_V = 0.5346\Delta\nu_L + \sqrt{0.2169\Delta\nu_L^2 + \Delta\nu_G^2}, \tag{2.18}$$

where $\Delta\nu_G$ is the Gaussian linewidth. A maximum 5% linewidth broadening due to impurities is here adopted, and yields a maximum impurity percentage of $\sim 10\%$ for contamination by air molecules (see [2] for broadening coefficients of acetylene in various buffer gases and [32] for numerical values of the Gaussian linewidths). According to a measured gas leakage rate of 1 mbar/h, this corresponds to a maximum allowed filling time of 10 hours for a 100 mbars filling pressure. In addition, by considering minimum fibre lengths of 5 m to ensure a minimal absorption efficiency according to the Beer-Lambert absorption law, a microstructured fibre should have a minimum hole diameter of 3 μm. These restrictions for the fibre characteristics are illustrated as shaded regions in Fig. 2.6. This is another indication that the gas flow dynamics is a crucial matter to consider when designing microstructured fibres for gas detection and gas cell applications.

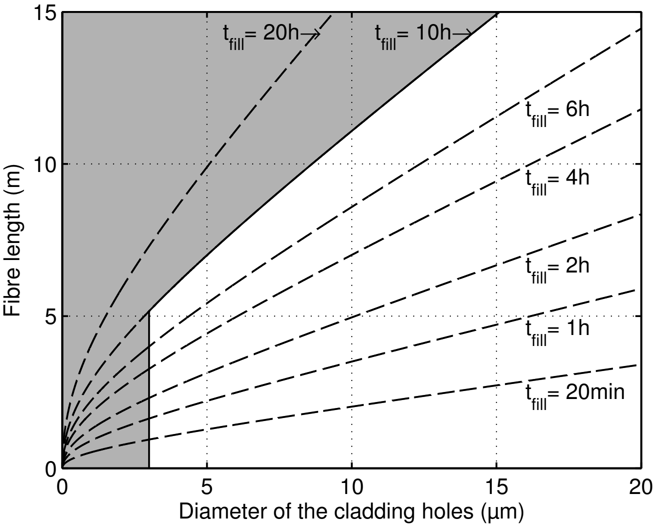

Figure 2.6. Contours of constant filling time are plotted in the $2a-L$ plane for a filling pressure of 100 mbars according to Eq. 2.11 & 2.15 ($P/P_0 = 85\%$).

2.4. All-fibre absorption cells

One powerful application of photonic crystal fibres is the possibility to fill the air holes with a given gas species and to hermetically seal the gas inside to obtain an all-fibre gas cell. Perfect sealing of the gas cell is obtained by fusion splicing the fibre ends to plain silica fibres, however resulting in a contamination of the gas cell by outside gases as this is performed at atmospheric pressure. Moreover gas cells are usually filled with low-pressure gases ($P \leq 50$ torrs) for applications requiring precise wavelength standards [1]. For such applications pressure broadening would be very detrimental, hence special techniques must be used to obtain low-pressure fibre gas cells that contain only a pure set of gas molecules.

2.4.A. The helium permeation technique

One of such techniques relies on the permeation of helium gas through the silica walls of the fibre [21]. Actually helium permeates all glass materials with different efficiencies, the permeation rate being higher for fused silica than other glasses [24]. One naive way of visualizing gas permeation is to imagine small helium molecules with a diameter of 1.95 Å dissolving in the interstices of the glass structure. The interstitial diameter of fused silica is estimated to 2.7 Å by comparing the permeation rate of other gas molecules (see Table 2.II).

Table 2.II. Permeation constants for several gases in fused silica [24]

Gas	Gas permeation rate at 700 °C ($cm^3s^{-1}cm^{-2}mm^{-1}cmHg^{-1}$)	Molecular diameter (Å)
Helium	$2.1 \cdot 10^{-8}$	1.95
Hydrogen	$2.1 \cdot 10^{-9}$	2.5
Deuterium	$1.7 \cdot 10^{-9}$	2.55
Neon	$4.2 \cdot 10^{-10}$	2.4
Oxygen	Under 10^{-15}	3.2
Nitrogen	Under 10^{-15}	3.4

Using this technique hermetically sealed all-fibre gas cells containing a pure set of gas molecules could be obtained for all fibre-based experiments presented in this work. The empty capillaries were filled with low-pressure acetylene gas from one end according to §2.3.C. After that helium gas was loaded inside the fibre holes at a pressure of 1.5 bars before splicing was performed. Then hermetic sealing of the fibre gas cell was realised by splicing the opened end to a plain silica fibre. Helium molecules trapped inside the gas cell after the splicing procedure were removed by placing the cell back inside the vacuum chamber and applying a strong pressure gradient to increase the permeation rate. The evolution of one absorption line throughout the helium permeation process is shown in Fig. 2.7 for an index-guiding PCF (scale bar: 20 μm).

As demonstrated by the width of the absorption line, there is no contamination by air molecules with this special technique. Air contamination could be prevented because of the helium molecules flowing out of the fibre holes according to the pressure gradient. However a non-negligible amount of gas molecules was lost during the splicing procedure; they were probably trapped by the flow of

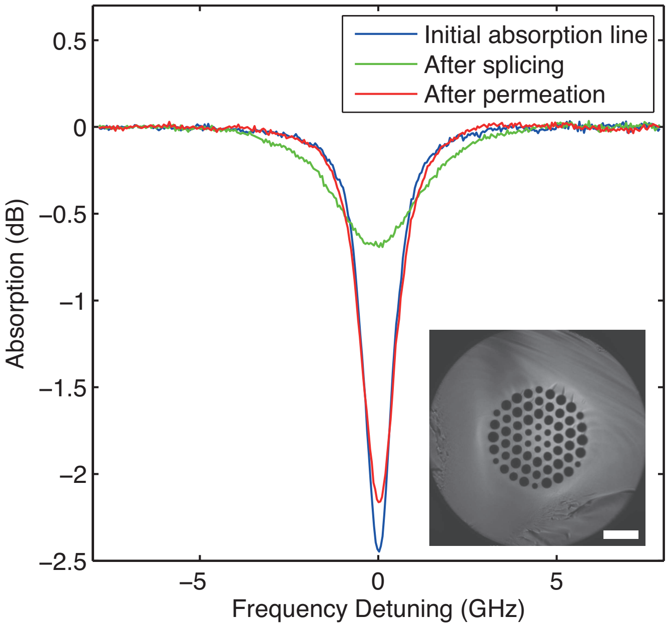

Figure 2.7. Helium permeation process in a microstructured-core photonic crystal fibre. From the initial gas loading to the final sealed absorption cell, the width of the absorption line remains equal, demonstrating the efficiency of the technique.

helium diffusing outside the fibre holes. This drawback can actually be beneficial as the average pressure in the fibre can be lowered without having to fill the gas cell at a lower pressure, which would take a longer filling time according to Eq. 2.16.

2.4.B. Long-term stability of fibre gas cells

The efficiency of the sealing technique was tested over a two year period by comparing absorption lines acquired after the gas cells were prepared and several months later. Figure 2.8 shows the absorption profile of the P15 line obtained in two different fibre gas cells, a hollow-core (HC) PCF filled with 5 mbars and a solid-core (SC) PCF filled with 76 mbars. As illustrated by Fig. 2.8, the acetylene profiles retained their original absorption profiles seven months later and 20 months later, respectively (see green and red profiles), demonstrating the excellent long-term stability of all-fibre gas cells.

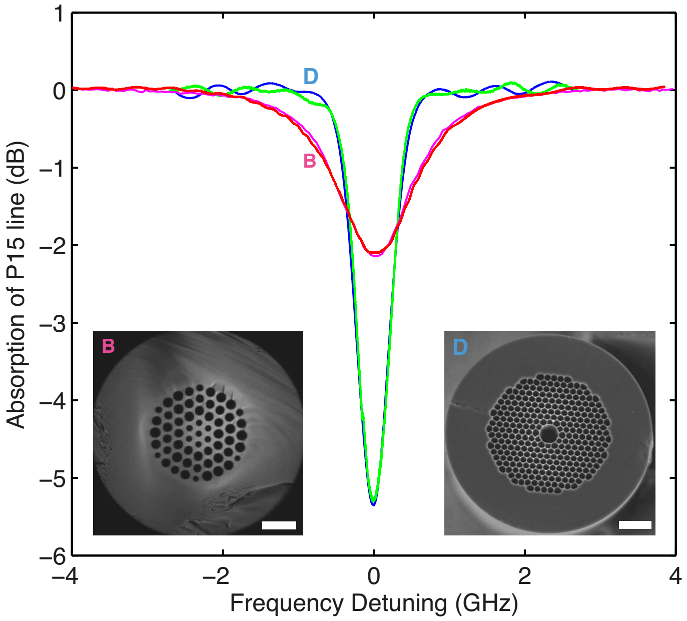

Figure 2.8. Long-term absorption stability of two fibre gas cells, a microstructured-core PCF (B) and a hollow-core PCF (D) (scale bars indicate 20 μm). The blue and pink curves represents absorption profiles measured directly after the gas cells were prepared. The green and red curves represent absorption profiles measured 7 and 20 months later, respectively.

2.4.C. Comparative study of various all-fibre absorption cells

The two fibre gas cells shown in Fig. 2.8 presented very different absorption profiles, most notably in the absorption coefficient and the absorption linewidth. In hollow-core fibres, the nearly complete overlap between the optical field and the gas molecules yields strong absorption efficiencies. They can be filled at vacuum pressures to perform saturated absorption spectroscopy owing to the resulting small Lorentzian linewidths indicative of long relaxation times on excited states. In addition much smaller fibre lengths can be used for gas detection applications, hence reducing gas detection times according to the square of the reduced length for the same fibre hole diameter. Hollow-core fibres perform also very well regarding the linewidths of the absorption profiles, with the difference in linewidths being due to very different contributions from transit-time broadening. The transit time of molecules through the laser beam is relatively long in hollow-core fibres due to the large beam waist (w=3.5 μm) of the optical field propagating inside the hollow core. However the transit time through the optical beam can be fairly small in solid-core fibres due to the submicron dimensions of the evanescent field, resulting in large contributions to the spectral linewidth. The difference in linewidths between the two fibres types is thus mostly due to transit-time broadening as the contribution from pressure broadening is fairly small.

Another difference between the two fibre types lies in the spectral noise observed in the absorption profiles. The spectral quality of the microstructured solid-core PCF (pink and red) is remarkable, while non-negligible noise can be seen in the absorption spectra of hollow-core fibres (blue and green profiles). The origin of these background oscillations has yet to be fully explained, however several hypotheses exist. These could be due to reflections at the splice points as the hollow core forms a cavity between the high-index silica core of standard fibres, however unlikely as the interference noise is also seen for unspliced fibres [23, 27]. It can possibly result from the interference between the fundamental air mode and higher guided optical modes [27, 28]. Hollow-core photonic bandgap fibres support multimode propagation due to the relatively high diameter of the hollow-core. The number of air modes supported by a photonic bandgap fibre scales as the hollow-core area and is typically 10-14 for a 11 μm hollow-core PCF and 35-45 optical modes for a 20 μm hollow-core [26]. The fundamental mode can be selectively excited by careful alignement of the launch optics, however part of the power can be transferred to higher order modes due to perturbations along the fibre. Moreover any spatial offset (e.g. 2 μm) in the launch conditions will result in higher modes being readily excited and a thus significant fraction of power can be coupled into these modes. Finally the background noise seen in Fig. 2.8 can originate from interference with surface modes propagating at the silica-air boundary [15, 23]. Surface modes interact with air-guided modes as they share a degree of spatial symmetry and overlap and they can affect the overall transmission of a photonic bandgap fibres [4, 30]. Further investigation is therefore needed to identify the origin of those background oscillations in hollow-core fibres, but solid assumption already exists the causes that all lead to multipath propagation and interferences.

2.5. Laser stabilisation using fibre gas cells

Fields such as high-resolution spectroscopy require an accurate stabilisation of laser frequency as lasers tend to drift with time. Frequency drifts are mainly caused by temperature drifts and acoustic vibrations of laser mirrors and can reach $\sim$ 4% of the linewidth of an absorption feature over a five minute period (see Fig. 2.10).

Frequency stabilisation systems consist of a laser controller, a frequency standard, and a feedback mechanism. An effective frequency standard should be insensitive to external perturbations and should exhibit long-term stability [6]. In this respect fibre gas cells are attractive candidates as frequency standards and they offer the additional benefits of alignment-free fibre-based systems.

A simple frequency stabilisation test was conducted using a PCF gas cell filled with 76 mbars of acetylene gas. A low-frequency current modulation (5-Hz ramp signal) was applied to a DFB laser diode to slowly sweep the laser line across the absorption line and a second modulation rapidly dithered the applied current (1.869-kHz sinusoidal signal). A lock-in amplifier demodulated the detected signal at the dithering frequency and harmonic signals were acquired with an oscilloscope.

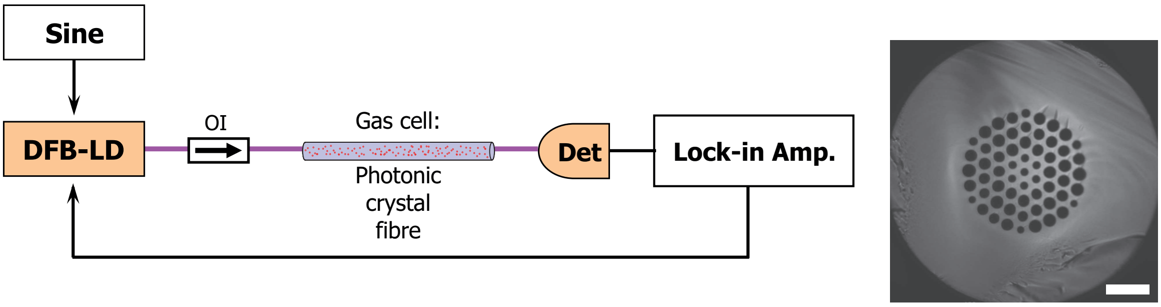

Figure 2.9. All-fibre frequency stabilisation system. A 1.869-kHz sine modulation dithers the injection current of a DFB laser diode and a lock-in amplifier demodulates the detected signal at the sine frequency. A feedback loop provides injection current corrections to the laser controller to compensate any frequency drift of the laser line.

The operating range for laser stabilisation was identified by acquiring the first-harmonic signal and locating the linearly varying region at the center of the first derivative profile (see the dashed line on left panel in Fig. 2.10). Then the 5-Hz ramp modulation was switched off and the current manually tuned to the center of the absorption line (~0V output error). The demodulated signal was then fed to the laser controller in a feedback loop according to Fig. 2.9. The frequency drift of the laser diode is shown in the right panel of Fig. 2.10 in free-running mode and with the feedback loop active. The frequency information was provided by the amplitude of the error signal divided by its slope in the central linear region (blue curve).

As illustrated in Fig. 2.10, the laser frequency fluctuations could be reduced ~ 50X after locking

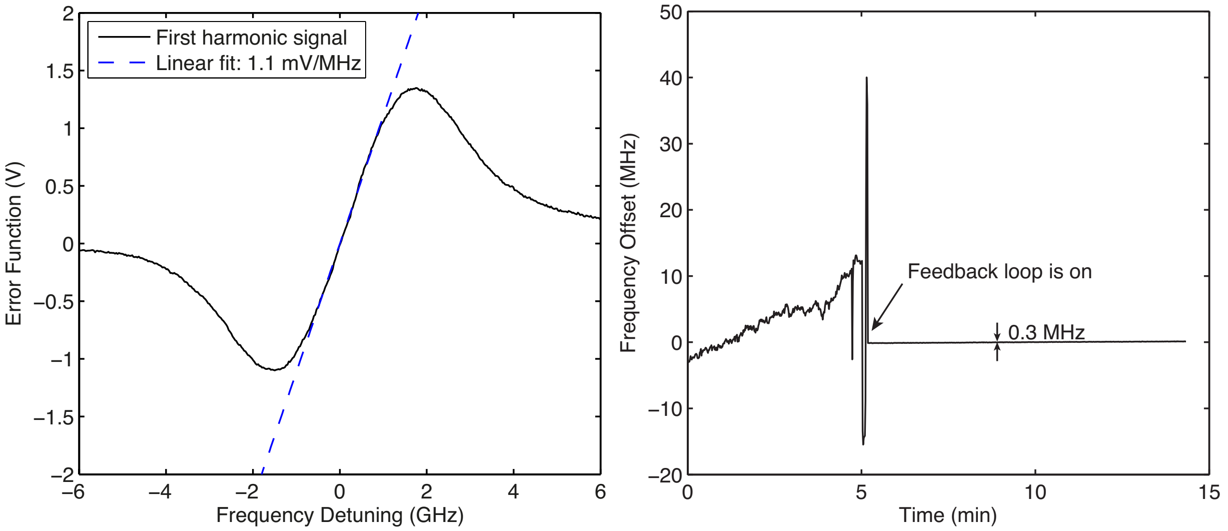

Figure 2.10. Frequency stabilisation of a DFB laser diode using a PCF frequency reference filled with 76 mbars of acetylene gas. Left panel: Signal profile of the error function. The dashed line represents the linear fitting of the error signal in the central region. Right panel: Laser fluctuations as a function of time in free-runing and in locked-mode. Frequency fluctuations are reduced from 15 MHz to 0.3 MHz by locking the laser line to the P15 absorption line ($\lambda = 1534.1$nm).

the laser frequency to the absorption line. The relative instability $\Delta f/f$ of the laser frequency was $1.5 \cdot 10^{-9}$ once locked to the absorption line, which is fairly good considering the compactness of the setup. A straightforward improvement would be to perform lock-in detection at the third harmonic as the first derivative of the absorption line is strictly not zero at the center of the absorption line due to intensity modulation. Another considerable improvement would be to use saturated absorption spectroscopy to obtain Doppler-free absorption lines since the efficiency of the wavelength stabilisation technique is a function of the linewidth of the absorption feature [6]. Relative frequency instabilities of $1.2 \cdot 10^{-11}$ could be obtained using sub-Doppler features and hollow-core fibre gas cells filled at vacuum pressures [19].

References

[1] Benabid, F., Couny, F., Knight, J. C., Birks, T. A., and Russell, P. S. J. (2005). Compact, stable and efficient all-fibre gas cells using hollow-core photonic crystal fibres. *Nature*, 434:488–491.

[2] Bond, K. S., Collett, N. D., Fuller, E. P., Hardwick, J. L., Hinds, E. E., Keiber, T. W., Kelly-Morgan, I. S. G., Matthys, C. M., Pilkenton, M. J., Sinclair, K. W., and Taylor, A. A. (2008). Temperature dependence of pressure broadening and shifts of acetylene at 1550 nm by He, Ne, and Ar. *Applied Physics B: Lasers and Optics*, 90(2):255–262.

[3] Chin, S., Dicaire, I., Beugnot, J.-C., Foaleng-Mafang, S., Gonzalez-Herraez, M., and Thévenaz, L. (2009). Material slow light does not enhance beer-lambert absorption. In *Slow and Fast Light*, page SMA3. Optical Society of America.

[4] Couny, F. and Benabid, F. (2009). Optical frequency comb generation in gas-filled hollow core photonic crystal fibres. *Journal of Optics A: Pure and Applied Optics*, 11(10):103002.

[5] Cunningham, R. and Williams, R. (1980). *Diffusion in Gases and Porous Media*. Plenum Press.

[6] Demtröder, W. (2008). *Laser Spectroscopy: Vol. 1: Basic Principles*. Springer Berlin Heidelberg, 4th edition.

[7] Dicaire, I., Beugnot, J.-C., and Thévenaz, L. (2010). Analytical modeling of the gas-filling dynamics in photonic crystal fibers. *Appl. Opt.*, 49(24):4604–4609.

[8] Dong, L., Thomas, B. K., and Fu, L. (2008). Highly nonlinear silica suspended core fibers. *Opt. Express*, 16(21):16423–16430.

[9] Dushman, S., of General Electric Research Laboratory, J. M. L. R. S., and Brown, S. C. (1962). Scientific foundations of vacuum technique. *American Journal of Physics*, 30(8):612–612.

[10] Euser, T. G., Chen, J. S. Y., Scharrer, M., Russell, P. S. J., Farrer, N. J., and Sadler, P. J. (2008). Quantitative broadband chemical sensing in air-suspended solid-core fibers. *Journal of Applied Physics*, 103(10):103108.

[11] Finazzi, V., Monro, T., and Richardson, D. (2003). The role of confinement loss in highly nonlinear silica holey fibers. *Photonics Technology Letters, IEEE*, 15(9):1246 –1248.

[12] Fini, J. M. (2004). Microstructure fibres for optical sensing in gases and liquids. *Measurement Science and Technology*, 15(6):1120.

[13] Gayraud, N., Kornaszewski, Ł. W., Stone, J. M., Knight, J. C., Reid, D. T., Hand, D. P., and MacPherson, W. N. (2008). Mid-infrared gas sensing using a photonic bandgap fiber. *Appl. Opt.*, 47(9):1269–1277.

[14] Henningsen, J. and Hald, J. (2008). Dynamics of gas flow in hollow core photonic bandgap fibers. *Appl. Opt.*, 47(15):2790–2797.

[15] Henningsen, J., Hald, J., and Peterson, J. C. (2005). Saturated absorption in acetylene and hydrogen cyanide in hollow-core photonic bandgap fibers. *Opt. Express*, 13(26):10475–10482.

[16] Hoo, Y. L., Jin, W., Shi, C., Ho, H. L., Wang, D. N., and Ruan, S. C. (2003). Design and modeling of a photonic crystal fiber gas sensor. *Appl. Opt.*, 42(18):3509–3515.

[17] Jaroszewicz, L., Murawski, M., Nasilowski, T., Stasiewicz, K., Marć, P., Szymański, M., and Mergo, P. (2011). Methodology of splicing large air filling factor suspended core photonic crystal fibres. *Opto-Electronics Review*, 19:256–259.

[18] Jost, W. (1970). *Diffusion in solids, liquids, gases.* Academic Press, 3rd edition.

[19] Knabe, K., Wu, S., Lim, J., Tillman, K. A., Light, P. S., Couny, F., Wheeler, N., Thapa, R., Jones, A. M., Nicholson, J. W., Washburn, B. R., Benabid, F., and Corwin, K. L. (2009). 10 khz accuracy of an optical frequency reference based on $^{12}C_2H_2$-filled large-core kagome photonic crystal fibers. *Opt. Express*, 17(18):16017–16026.

[20] Knight, J. C. (2003). Photonic crystal fibres. *Nature*, 424(6950):847–851.

[21] Light, P. S., Couny, F., and Benabid, F. (2006). Low optical insertion-loss and vacuum-pressure all-fiber acetylene cell based on hollow-core photonic crystal fiber. *Opt. Lett.*, 31(17):2538–2540.

[22] Monro, T. M., Warren-Smith, S., Schartner, E. P., François, A., Heng, S., Ebendorff-Heidepriem, H., and Afshar, S. (2010). Sensing with suspended-core optical fibers. *Optical Fiber Technology*, 16(6):343 – 356.

[23] NIST Special Publication 1055, Boulder, C., editor (2006). *Comparison of Saturated Absorption Spectra of Acetylene Gas Inside Photonic Bandgap Fibers.*

[24] Norton, F. J. (1957). Permeation of gases through solids. *Journal of Applied Physics*, 28(1):34 –39.

[25] O'Hanlon, J. (2003). *A user's guide to vacuum technology.* Wiley.

[26] Petrovich, M. N., Poletti, F., van Brakel, A., and Richardson, D. J. (2008). Robustly single mode hollow core photonic bandgap fiber. *Opt. Express*, 16(6):4337–4346.

[27] Pineda-Vadillo, P., Lynch, M., Charlton, C., Donegan, J. F., and Weldon, V. (2009). Non-resonant wavelength modulation saturation spectroscopy in acetylene-filled hollow-core photonic bandgap fibres applied to modulation-free laser diode stabilisation. *Opt. Express*, 17(25):23309–23315.

[28] Ritari, T., Tuominen, J., Ludvigsen, H., Petersen, J., Sørensen, T., Hansen, T., and Simonsen, H. (2004). Gas sensing using air-guiding photonic bandgap fibers. *Opt. Express*, 12(17):4080–4087.

[29] Russell, P. S. (2006). Photonic-crystal fibers. *J. Lightwave Technol.*, 24(12):4729–4749.

[30] Saitoh, K., Mortensen, N., and Koshiba, M. (2004). Air-core photonic band-gap fibers: the impact of surface modes. *Opt. Express*, 12(3):394–400.

[31] Snyder, A. W. and Love, J. D. (1983). *Optical Waveguide Theory.* Chapman and Hall, New York.

[32] Swann, W. C. and Gilbert, S. L. (2000). Pressure-induced shift and broadening of 1510–1540-nm acetylene wavelength calibration lines. *J. Opt. Soc. Am. B*, 17(7):1263–1270.

[33] Webb, A. S., Poletti, F., Richardson, D. J., and Sahu, J. K. (2007). Suspended-core holey fiber for evanescent-field sensing. *Optical Engineering*, 46(1):010503.

[34] Yaws, C. L. (1995). *Handbook of transport property data: viscosity, thermal conductivity, and diffusion coefficients of liquids and gases.* Gulf Pub. Co.

[35] Zhu, Y., Du, H., and Bise, R. (2006). Design of solid-core microstructured optical fiber with steering-wheel air cladding for optimal evanescent-field sensing. *Opt. Express*, 14(8):3541–3546.

CHAPTER 3

MOLECULAR ABSORPTION AND SLOW LIGHT IN OPTICAL FIBRES

3.1. Introduction

So far the effect of molecular absorption on radiation has been determined by fixed quantities such as the gas concentration and the optical path length. To improve sensing efficiencies as to realise more compact photonic devices, there have been theoretical considerations that slowing down the velocity of a light signal could lead to enhanced light-matter interactions. This enhancement was thought to result from a longer transit time of light signals in optical media and to a higher energy density due to spatial compression [2, 4]. These previous considerations suggested the absorption coefficient to be inversely proportional to the group velocity of a light signal, however no experimental verification of the hypothetical enhancement of light-matter interactions was given. This chapter presents the experimental study of the possibilities of slow-light in enhancing light-matter interactions using optical fibres.

3.2. Signal propagation in dispersive media

Dispersion is defined as the phenomenon by which the refractive index n (and thereby the phase velocity $v_{ph} = c/n$) seen by a wave is frequency-dependent. Considering a signal wave travelling in the z direction through a lossless dispersive medium with refractive index $n(\omega)$, the initial electric field at $z = 0$ is:

$$E(0,t) = E_{env}(t)\exp\left(i\omega_0 t\right), \tag{3.1}$$

where $E_{env}(t)$ is the complex envelope of the signal wave, ω_0 is the carrier frequency, and t is time. By Fourier decomposition, the corresponding initial spectral distribution of the electric field is:

$$E(0,\omega) = \int_{-\infty}^{\infty} E(0,t)\exp\left(-i\omega t\right)dt. \tag{3.2}$$

A signal wave with this spectral distribution then travels a distance z in a transparent but dispersive medium. Through the transfer function $T(\omega) = \exp\left[-ik(\omega)z\right]$ the frequency component ω of the optical signal will find its phase modified to:

$$E(z,\omega) = E(0,\omega)\exp[-ik(\omega)z],\ k(\omega) = n(\omega)\omega/c, \tag{3.3}$$

in the frequency domain, where k is the wavevector. The time dependence of the optical signal is retrieved via its inverse Fourier transform:

$$E(z,t) = \int_{-\infty}^{\infty} E(z,\omega)\exp(i\omega t)d\omega = \int_{-\infty}^{\infty} E(0,\omega)\exp[-ik(\omega)z]\exp[i\omega t]d\omega. \tag{3.4}$$

The specific cases of a highly dispersive optical medium or propagation of very short temporal optical signals are difficult to treat analytically, but the propagation through weakly dispersive medium can be handled and treated in the following way. For an optical signal showing frequency components ω situated close to the central frequency ω_0, the wavevector is expanded in its Taylor series:

$$k(\omega) = k_0 + \left.\frac{\partial k(\omega)}{\partial \omega}\right|_{\omega_0}(\omega - \omega_0) + ... \tag{3.5}$$

Keeping the zero and first order terms the optical signal becomes:

$$E(z,t) = \int_{-\infty}^{\infty} E(0,\omega)\exp[-ik_0 z]\exp\left[-i\left.\frac{\partial k(\omega)}{\partial \omega}\right|_{\omega_0}(\omega - \omega_0)z\right]\exp[i\omega t]d\omega \tag{3.6}$$

By replacing the detuning frequency $\omega - \omega_0$ with Ω we obtain:

$$E(z,t) = \exp[-ik_0 z]\exp[i\omega_0 t]\int_{-\infty}^{\infty} E(0,\omega)\exp\left[i\Omega\left(t - \left.\frac{\partial k(\omega)}{\partial \omega}\right|_{\omega_0} z\right)\right]d\Omega. \tag{3.7}$$

Since the amplitude components of the initial optical signal $E(0,t)$ in the Fourier domain $E(0,\omega)$ are equal to that of the envelope $E_{env}(t)$ (see Fig. 3.1):

$$E(0,\omega) = \int_{-\infty}^{\infty} E(0,t)\exp(-i\omega t)dt = \int_{-\infty}^{\infty} E_{env}(t)\exp(-i\Omega t)dt = E_{env}(\Omega), \tag{3.8}$$

we can substitute $E(0,\omega)$ with $E_{env}(\Omega)$ in Eq. 3.7:

$$E(z,t) = \exp[-ik_0 z]\exp[i\omega_0 t]\int_{-\infty}^{\infty} E_{env}(\Omega)\exp\left[i\Omega\left(t - \left.\frac{\partial k(\omega)}{\partial \omega}\right|_{\omega_0} z\right)\right]d\Omega. \tag{3.9}$$

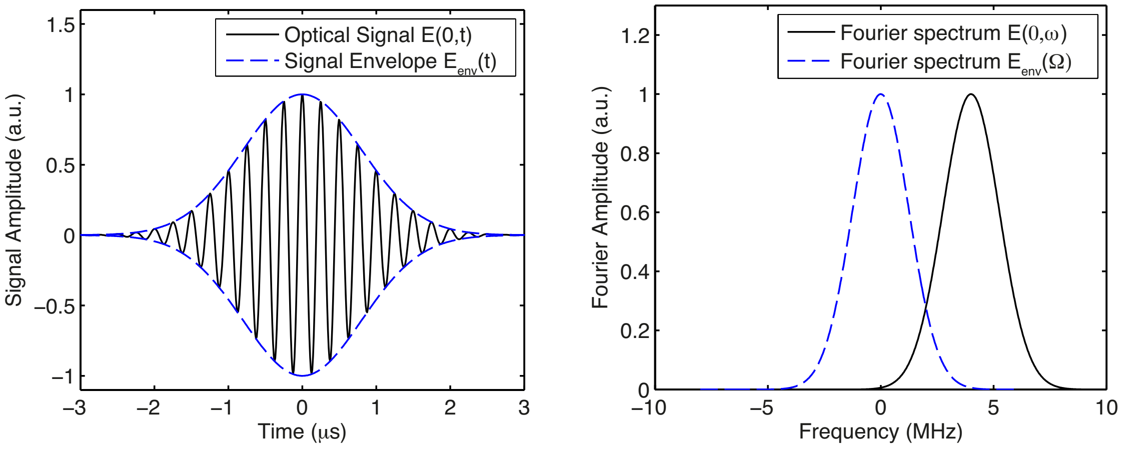

Figure 3.1. Left panel: Initial optical signal $E(0,t)$ (solid curve) with signal envelope $E_{env}(t)$ (dashed curve). Right panel: Fourier amplitude distribution centered about ω (solid curve) for the optical signal and zero (dashed curve) for that of the envelope $E_{env}(\Omega)$.

Thus the general expression for an optical signal propagating a distance z is:

$$E(z,t) = \exp\left[-i(k_0 z - \omega_0 t)\right] E_{env}\left(z,\, t - \left.\frac{\partial k(\omega)}{\partial \omega}\right|_{\omega_0} z\right) \tag{3.10}$$

Two different velocities are readily identified from Eq. 3.10:

$$v_\phi \equiv \frac{\omega_0}{k_0} = \frac{c}{n} \quad \& \quad v_g \equiv \left.\frac{\partial \omega}{\partial k}\right|_{\omega_0}. \tag{3.11}$$

It follows that in dispersive media the signal envelope travels at a group velocity v_g different from the phase velocity v_ϕ. Slow light can thus be realised by controlling the dispersion properties of a material. Finally the group index and the group delay are defined as $n_g \equiv c/v_g$ and $\tau_g \equiv z/v_g$, respectively.

3.3. Material and structural slow light

Most slow-light systems rely on controlling the dispersion properties of a material in order to reduce the group velocity. Regions of high group index n_g are obtained when there is a significant change in the refractive index with frequency through the dispersive term $\omega dn/d\omega$:

$$n_g \equiv c/v_g = \frac{\partial\, \omega n(\omega)}{\partial \omega} = n + \omega dn/d\omega. \tag{3.12}$$

There are generally two sources of dispersion: material dispersion and waveguide dispersion. Material dispersion occurs when the refractive index of the bulk material is a function of frequency. Slow-light systems based on material dispersion, hereafter called material slow-light systems, thus produce abrupt spectral changes in the refractive index of the material. For example the refractive index of a medium can be locally changed via a material excitation coupling two strong light waves whose frequency difference is given by the frequency of the excitation. This coupling occurs over a very narrow spectral range for the Brillouin resonance (30 MHz typically) and induces a strong dispersive effect that can be used to control the group velocity. Structural slow-light systems, on the other hand, are based on changing the structural dispersion properties of a system. Such systems include photonic crystals as they exhibit strong tailorable dispersion properties owing to the wavelength scale periodicity of their microstructure. Microring resonators also provide strong dispersion effects as the group delay depends critically on the detuning from the resonator frequency. Substantial group delays can be obtained for light signals matching the resonator frequency and can be attributed to light recirculating in the resonator. Owing to the different nature of material and structural slow-light, both systems will be implemented in the following experimental studies to verify their possibilities in enhancing light-matter interactions in optical fibres.

3.4. Material slow light via Stimulated Brillouin Scattering

This section presents the experimental results of the effect of material slow-light on molecular absorption. The experiment is designed so that molecular absorption and slow light generation are negligibly correlated and can be controlled independently. The group velocity of a light signal was modified through stimulated Brillouin scattering. In stimulated Brillouin scattering (SBS), an acoustic wave is generated in the material and causes a signal wave to experience gain from a strong light wave spectrally upshifted by the Brillouin frequency shift ν_B of the medium. With the Kramers–Kronig relations connecting the real and imaginary parts of the refractive index of a medium, any change in its absorptive or amplifying properties will result in a change in its dispersive properties and vice versa.

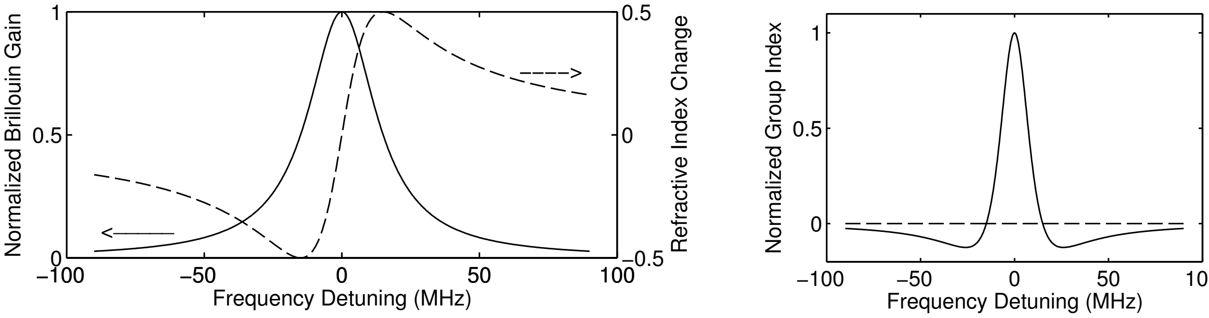

Figure 3.2. Left panel: Brillouin gain (solid line) and dispersion (dashed line) for a 30-MHz Brillouin resonance [3]. Right panel: Corresponding group index increase.

In SBS process a light wave will experience gain over a very narrow spectral range, causing abrupt changes in the refractive index of the material (see left panel of Fig. 3.2). Large values of n_g can thus be obtained via a larger dispersive term $\omega dn/d\omega$ (see right panel of Fig. 3.2 and pulse delay measurements in Fig. 3.3).

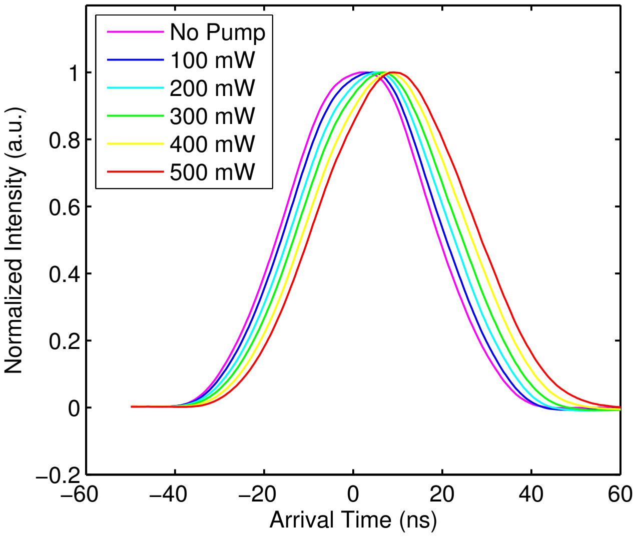

Figure 3.3. Observation of pulse delaying using stimulated Brillouin scattering (SBS) based slow-light. The higher the pump power and the stronger the dispersive effect one can obtain in order to decrease the group velocity. These measurements were obtained in a 9.18-m long solid-core photonic crystal fibre.

3.4.A. Stimulated Brillouin Scattering

In the SBS process an acoustic wave is generated in the material via electrostriction from the interference beating of a pump wave and a counterpropagating signal wave [3]. Electrostriction is a phenomenon by which the density of a material increases in regions of high optical intensity. Efficient generation of the acoustic wave will occur for an interference beating exactly superimposed onto the acoustic wave. This strict phase-matching condition leads to two counterpropagating waves whose frequency difference is given by the acoustic vibration frequency ν_B. The acoustic wave co-propagates with the high frequency wave and induces a moving dynamic Bragg grating that diffracts the high frequency wave into the lower frequency wave with the proper Doppler shift, providing gain to the lower frequency wave. The pump wave is spectrally upshifted by the Brillouin frequency shift ν_B so as to provide gain to the signal wave. The acoustic wave will then adjust to the new signal

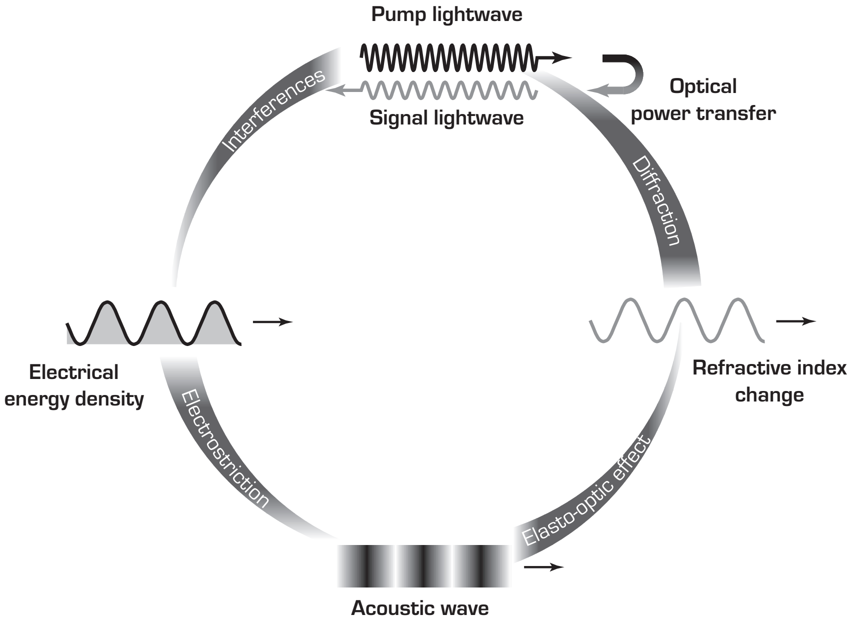
Pump lightwave
Signal lightwave
Optical
power transfer
Interferences
Diffraction
Electrical
energy density
Refractive index
change
Electrostriction
Elasto-optic effect
Acoustic wave

Figure 3.4. Schematic representation of the stimulated Brillouin scattering (SBS) process. A signal wave experiences gain from a counterpropagating pump spectrally upshifted by the Brillouin frequency shift ν_B. The interference beating of both waves creates via electrostriction an acoustic wave that diffracts the pump wave into the signal wave, reinforcing the nonlinear coupling. (From chapter 9 of [3], with permission).

intensity, providing a stronger coupling between both waves. The stimulated Brillouin scattering process is depicted in Fig. 3.4.

3.4.B. Experimental configuration and results

An absorption cell made of a solid-core photonic crystal fibre was the perfect candidate for performing the material slow-light experiment as it could also play the role of a Brillouin gain medium. The velocity of light in the PCF is controlled by modifying the material dispersion properties of the fibre core using stimulated Brillouin scattering. The fibre holes are filled with acetylene gas and the absorption of molecules is probed used evanescent-field spectroscopy. The benefit of using such configuration is that the effect of slow-light and optical absorption can be controlled independently without significantly interfering. Actually the acetylene absorption induces a fast light effect explained by the Kramers-Kronig relations, however the effect is very low compared to the slow light effect of the Brillouin gain. This is due to the relatively large width of the absorption resonance, which merely causes small changes in the refractive index of the acetylene gas (the opposite of Fig. 3.2). The dispersive term $\omega dn/d\omega$ is thus slightly modified by the acetylene resonance and induces a fast light effect of only a few percent.

The fibre chosen to perform this study is made of a solid silica core with a diameter of 2.87 μm and effective area of 5.3 μm^2 at $\lambda = 1.55\mu$m (see middle panel of Fig. 3.5). Numerical simulations of the fundamental optical mode propagating in such fibre have been done using the Matlab toolbox named Source Model Technique Package (SMTP) [1]. The mode field distribution of the fundamental optical mode is shown in the left panel of Fig. 3.5. Its effective refractive index is estimated to 1.407 and the fraction of optical power located inside the holes is estimated to 2.9 %. The intensity distribution of the evanescent field propagating inside the air holes is shown in the right panel of Fig. 3.5.

The experimental implementation of this fundamental light-matter interaction study is depicted in Fig. 3.6. A distributed-feedback (DFB) laser diode operating at 1535 nm was used as a light source and its output was split using a directional coupler. One branch was sent to an erbium-doped fibre amplifier (EDFA) to increase its optical power as to play the role of the pump wave. The pump power was precisely varied using a variable optical attenuator (VOA) before entering the fibre gas cell. The other branch was modulated through an electrooptic Mach-Zehnder intensity

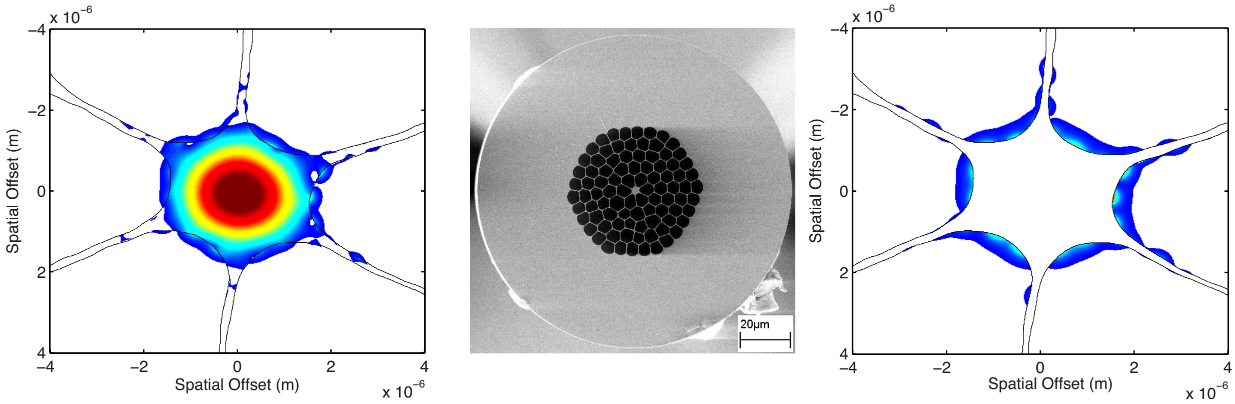

Figure 3.5. All-fibre gas absorption cell. Left panel: Calculated mode field distribution of the fundamental mode. Middle panel: SEM image of the solid-core photonic crystal fibre. Right panel: Distribution of the small evanescent fraction of the optical field available for sensing.

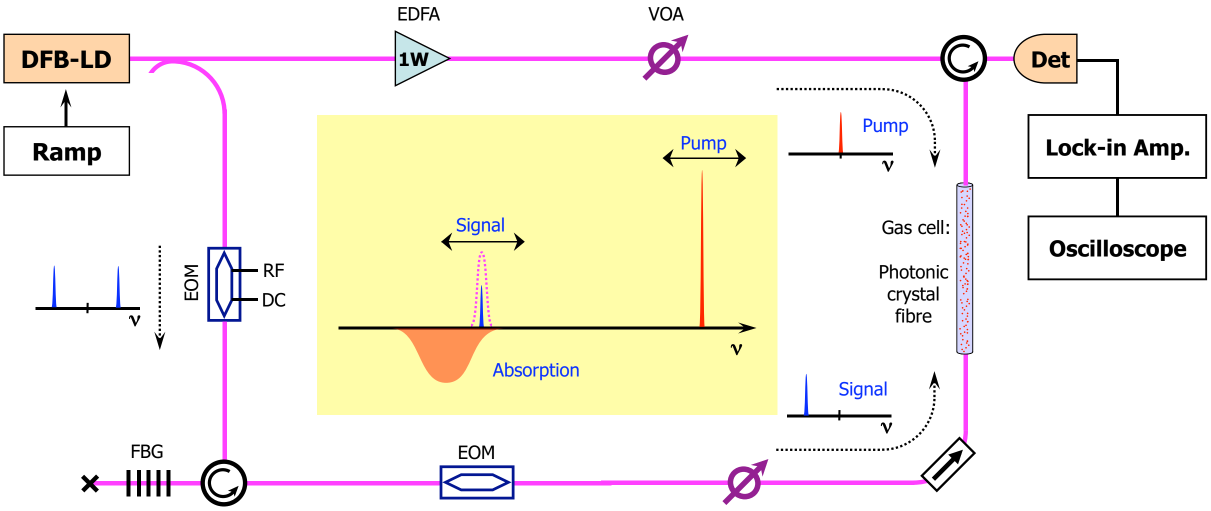
DFB-LD
Ramp
EDFA
1W
VOA
Det
Lock-in Amp.
Oscilloscope
Pump
Signal
Absorption
ν
Pump
ν
Gas cell:
Photonic crystal fibre
Signal
ν
EOM
RF
DC
ν
FBG
EOM

Figure 3.6. Experimental setup realising simultaneously slow-light and gas absorption in the same fibre gas cell. The optical frequency of the signal is amplified and slowed down using stimulated Brillouin scattering and is scanned through an absorption line. The frequency separation between the pump wave and the signal wave remains constant during the frequency scan.

modulator (EOM) at precisely the Brillouin frequency shift of the PCF to generate two first-order sidebands. The DC bias of the modulator was then adequately set to achieve complete suppression of the carrier. The lower frequency sideband was then filtered by a fibre Bragg grating (FBG) and launched into the PCF as the signal wave.

Absorption profiles were observed by sweeping the frequency of the signal wave over the absorption line using a slow variation of the driving current of the DFB laser diode. The pump frequency was also perfectly and constantly swept since the pump and signal waves are generated from the same laser source, preserving their exact spectral distance matched to the Brillouin shift. Consequently, even though the signal frequency was swept by the ramp signal, the pump wave continuously generated a Brillouin gain resonance at the swept signal frequency.

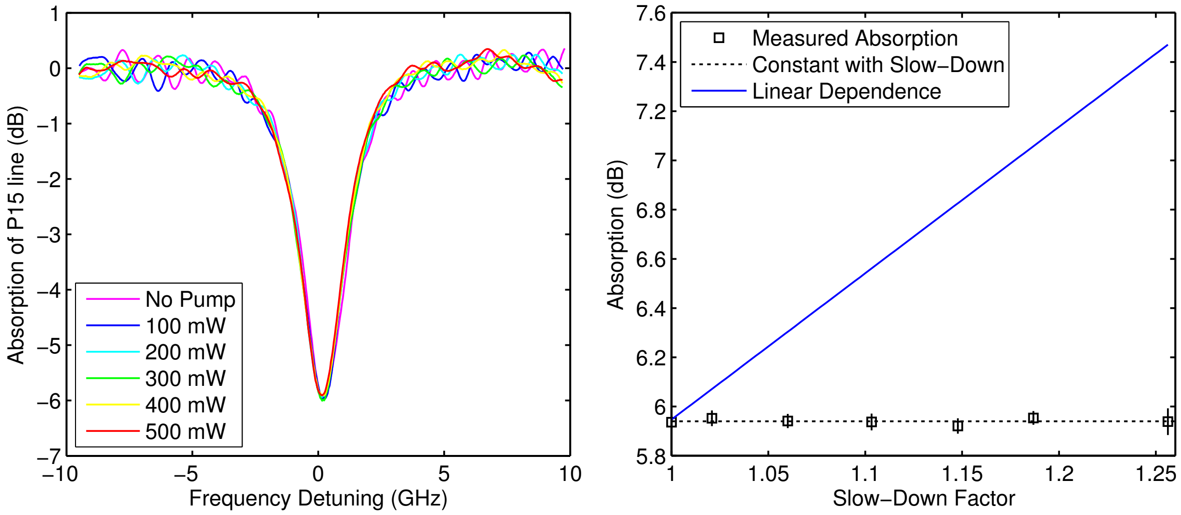

Figure 3.7. Effect of Brillouin slow-light on the P15 acetylene absorption profile. Left panel: P15 absorption profiles measured for several pump powers. Right panel: Peak absorption measured as a function of the slow-down factor (squares). The black dashed line represents the data points fitted with a constant value ($A = 5.940$ dB) while the blue line represents an absorption coefficient hypothetically proportional to the slow-down factor.

Clean absorption signals were then acquired by performing lock-in detection of the signal wave. This was done by sinusoidally modulating at 100 kHz the intensity of the signal wave branch using another external EOM. The signal power was then adjusted using another VOA to avoid any saturation of the acetylene transition by observing the absence of intensity-dependent absorption for the highest signal level used in the experiment. After propagation inside the PCF gas cell, the detected signal intensities were demodulated using a lock-in amplifier and acquired using a digital oscilloscope for several pump powers. The left panels of Fig. 3.7 and 3.8 present the P15 & P17 absorption profiles measured for several pump powers, respectively.

The effective slow-down factors shown in Fig. 3.7 & 3.8 were obtained from their corresponding pump powers from group velocity measurements and calibrations. For these measurements the frequencies of the pump and signal waves were spectrally positioned in a region where absorption resonances are absent. The SBS-induced group delay was then precisely determined by sinusoidally modulating the signal wave at 1 MHz by the external EOM. The phase of the sine wave after propagation through the PCF could be precisely determined for pump powers ranging from 0 to 500 mW in 100-mW steps. The comparison of the wave modulation phase obtained with the pump propagating in the fibre and with the pump switched off yielded a differential phase shift from which group delay changes were obtained. Additionally the transit time through the PCF absorption cell (45ns) was determined by performing the same measurement without the PCF. The group delay

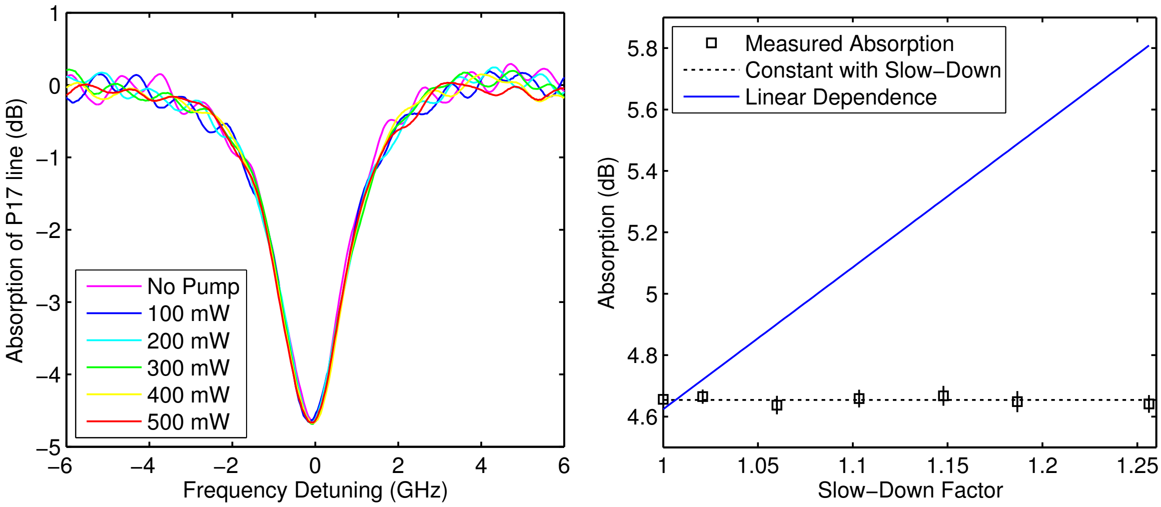

Figure 3.8. Effect of Brillouin slow-light on the P17 acetylene absorption profile. Left panel: P17 absorption profiles measured for several pump powers. Right panel: Peak absorption measured as a function of the slow-down factor (squares). The black dashed line represents the data points fitted with a constant value ($A = 4.654$ dB) while the blue line represents an absorption coefficient hypothetically proportional to the slow-down factor.

change was quantified by defining a slow-down factor S corresponding to the ratio between the transit time through the PCF gas cell with and without the pump wave, respectively. The largest time delay achieved through the PCF was 11.7 ns for a 600 mW pump power, corresponding to 26 % reduction in group velocity. The right panels of Fig. 3.7 and 3.8 present the P15 & P17 absorption peaks shown as a function of the slow-down factor.

3.4.C. Discussion

Both figures clearly show that the optical absorption of molecules is totally independent of the group velocity. This experimental result could be anticipated by realising that even though optical pulses are slowed down at low group velocities, the pulse duration remains identical for all group velocities. Thus the interaction time of each pulse with a set of molecules is not modified at low group velocities and cannot lead to an enhancement of the absorption effect. In addition the Beer-Lambert law and evanescent-field spectroscopy are scaled by the Poynting vector P describing energy flow and the energy velocity is actually not changed by stimulated Brillouin scattering based slow-light [5]. This can be understood by introducing the concept of the transport velocity of electromagnetic (EM) energy [6]. For propagation through an uniform transmission medium the electromagnetic energy velocity is defined as the ratio of the power flow density P to the electromagnetic energy density W:

$$v_{EM} = \frac{\langle P \rangle}{\langle W \rangle} \tag{3.13}$$

where chevrons denote spatial averaging over a closed surface for the Poynting vector P and over a volume for the EM energy density W. Very frequently energy velocity is equal to the group velocity, e.g. the case of pulse propagation through dispersive dielectric material with low loss such as silica glass. For the case of dispersive dielectric materials showing attenuation or gain at frequencies near resonance (e.g. lasers), group velocity is not equal to the electromagnetic energy velocity. Brillouin resonance is typically a narrow material resonance showing high attenuation or gain. At the Brillouin resonance the signal wave experiences gain from a pump wave via an acoustic wave, which becomes reinforced by a stronger signal wave due to interference and electrostriction. Energy is therefore constantly transferred between the acoustic wave and the propagating EM wave. The gain response is however not instantaneous as the acoustic wave must build up and adjust to the exponentially growing signal wave, leading to time delay and group velocity reduction (see Fig.

3.9). During this time as the acoustic wave builds up part of the wave energy is stored in the polarisation of the gain medium. Even though this localised energy contributes to increase the total energy density of the medium, it cannot participate to the evanescent-field spectroscopy for gas sensing purposes. Therefore only the EM energy density should be considered in the calculation of the energy velocity.

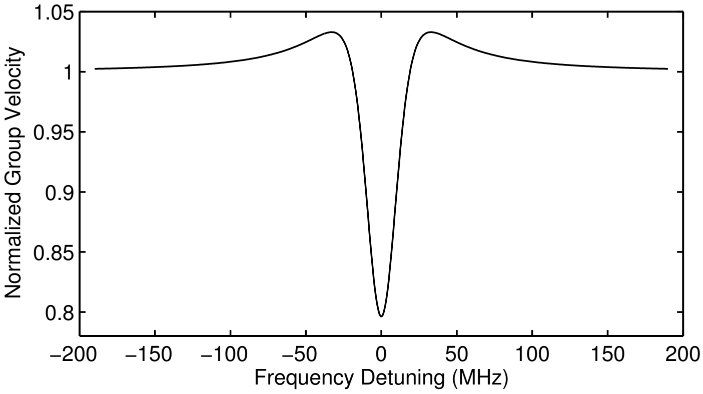

Figure 3.9. Theoretical group velocity profile v_g across a Brillouin resonance for a 15 dB gain in a 9.18-m long PCF fibre and normalised by its off-resonance value.

The expression for the velocity of the electromagnetic energy v_{EM} in an absorptive and dispersive material is:

$$v_{EM}(\omega) = \frac{2n(\omega)c}{1+n(\omega)^2+\kappa(\omega)^2}, \tag{3.14}$$

where $n(\omega)$ is the real part of the refractive index and $\kappa(\omega)$ is the imaginary part of the refractive index of the Brillouin resonance [6]. The EM energy velocity profile is shown below for a Brillouin gain of 15 dB in a 9.18-m long PCF fibre.

As illustrated in Fig. 3.10, the Brillouin resonance induces very weak changes in the EM energy velocity. The latter was calculated according to Eq. 3.14 with real and imaginary index profiles taken from chapter 3 of Ref. [3]. The EM energy velocity is thus negligibly modified by material slow light and therefore cannot lead to enhancement of light-matter interactions, as experimentally demonstrated by this slow-light experiment.

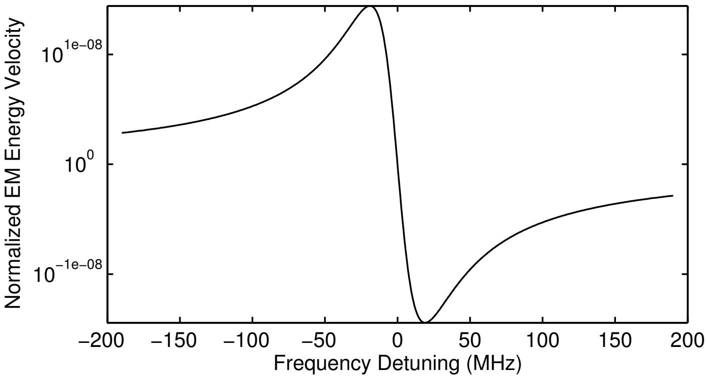

Figure 3.10. Theoretical electromagnetic (EM) energy velocity profile $v_{EM}(\omega)$ across a Brillouin resonance for a 15 dB gain in a 9.18-m long PCF fibre (Eq. 3.14).

3.5. Structural slow light via Cavity Ring Resonators

In cavity ring resonators substantial group delays can be obtained for light signals matching the resonator frequency and can be attributed to light recirculating in the resonator. Cavity ring resonators essentially behave as frequency filters because wavelengths fitting an integer number of times within the cavity length will be selected and the other wavelengths will be rejected. Strong waveguide dispersion effects can therefore be obtained in such devices. A macroscopic version of microring resonators was built using fibre optics to provide a series of closely packed resonances inside a given gas-phase optical absorption resonance. The experiment is designed so that the molecular absorption and the slow light generation are negligibly correlated and can be controlled independently, as it could be done with the material slow light experiment. The macroscopic cavity can be conveniently opened or closed to operate either in standard or in slow-light regime, leaving the absorbing fibre segment untouched. Closing the cavity results in delayed propagation and longer effective optical path lengths according to the cavity round-trip loss. Figure 3.11 illustrates the delaying effect of the cavity ring resonator on Gaussian pulses for several cavity recirculation factors.

3.5.A. Theoretical group delay in long cavity ring resonators

The group delay obtained in long cavity ring resonators can be calculated and turns out to be completely described by the cavity round-trip loss. In macroscopic cavities the cavity round-trip

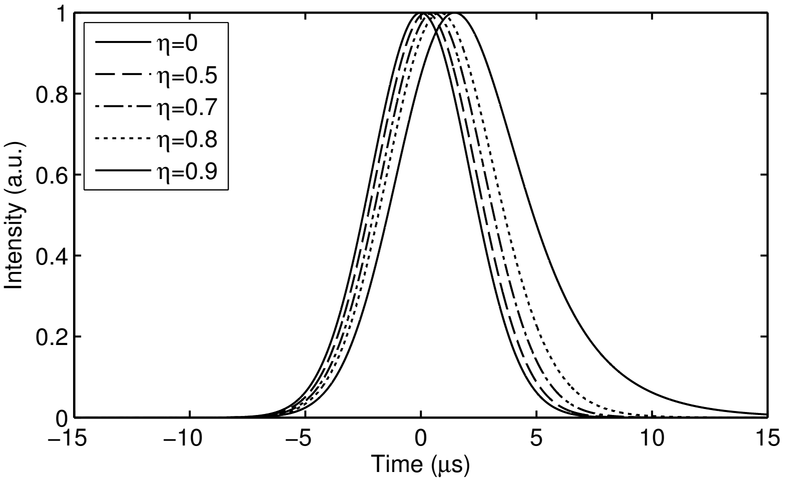

Figure 3.11. Theoretical delaying effect of the macroscopic cavity system on 5 μs Gaussian pulses for several cavity recirculation factors η (based on Eq. 3.21).

time can be fairly long compared to the coherence time of a semiconductor laser source. Typical laser linewidths are 5 MHz for distributed-feedback laser diodes, resulting in a coherence time of 200 ns. As the signal wave suffers from significant decoherence after a single propagation through the cavity, incoherent light signals are considered in the calculation of the group delay. Let's suppose, without loss of generality, a sine wave sinusoidally modulated at a frequency f. The optical intensity arriving at the detector is:

$$I(t) = P_0\left\{1 + m\cos[2\pi ft]\right\}, \tag{3.15}$$

where P_0 is the average optical intensity, m is the intensity modulation index, and t is time. The corresponding optical field is:

$$E(t) = \sqrt{P_0\left\{1 + m\cos[2\pi ft]\right\}}\exp\left(i2\pi\nu_0 t\right), \tag{3.16}$$

where ν_0 is the carrier frequency. The field arriving one round-trip later is:

$$E_{1\tau}(t) = \sqrt{P_0\left\{1 + m\cos[2\pi(ft - f\tau)]\right\}}\exp\left(i2\pi\nu_0 t\right)\exp(i\widehat{\phi_1}), \tag{3.17}$$

where τ is the cavity round-trip time and $\widehat{\phi_1}$ is the additional random phase due to wave propagation inside the cavity. The field arriving two round-trips later is:

$$E_{2\tau}(t) = \sqrt{P_0\left\{1+m\cos[2\pi(ft-2f\tau)]\right\}}\exp\left(i2\pi\nu_0 t\right)\exp(i\widehat{\phi_2}). \tag{3.18}$$

By taking into account the recirculation factor η related to the cavity round-trip loss, the total optical field inside the cavity is:

$$E_{tot}(t) = E(t) + \eta^{1/2}E_{1\tau}(t) + \eta E_{2\tau}(t) + \eta^{3/2}E_{3\tau}(t) + ... \tag{3.19}$$

The total optical intensity inside the cavity is:

$$\begin{aligned} I_{tot}(t) = \langle E_{tot}(t)\cdot E^*_{tot}(t)\rangle = &\left[E(t) + \eta^{1/2}E_{1\tau}(t) + \eta E_{2\tau}(t) + \eta^{3/2}E_{3\tau}(t) + ...\right] \\ &\cdot\left[E^*(t) + \eta^{1/2}E^*_{1\tau}(t) + \eta E^*_{2\tau}(t) + \eta^{3/2}E^*_{3\tau}(t) + ...\right] \end{aligned} \tag{3.20}$$

where chevrons denote temporal averaging. As each cross term will average to zero with time due to the random nature of the phase terms $\exp(i\widehat{\phi})$, the total intensity inside the cavity is:

$$\begin{aligned} I_{tot}(t) &= E(t)E^*(t) + \eta E_{1\tau}(t))E^*_{1\tau}(t) + \eta^2 E_{2\tau}(t)E^*_{2\tau}(t) + \eta^3 E_{3\tau}(t)E^*_{3\tau}(t) + ... \\ &= I(t) + \eta I_{1\tau}(t) + \eta^2 I_{2\tau}(t) + \eta^3 I_{3\tau}(t) + ... \end{aligned} \tag{3.21}$$

With an initial optical intensity $I(t) = P_0\{1+m\cos[2\pi ft]\}$ arriving onto the detector, the total intensity inside the cavity becomes:

$$I_{tot} = P_0\{1+m\cos[2\pi ft]\} + \eta P_0\{1+m\cos[2\pi(ft-f\tau)]\} + \eta^2 P_0\{1+m\cos[2\pi(ft-2f\tau)]\} + ... \tag{3.22}$$

By rearranging terms one can obtain:

$$I_{tot}(t) = P_0\left\{1+\eta+\eta^2+...\right\} + P_0 m\left\{\cos[2\pi ft] + \eta\cos[2\pi(ft-f\tau)] + \eta^2\cos[2\pi(ft-2f\tau)] + ...\right\}. \tag{3.23}$$

Since the recirculation factor η is restricted to the $0 \leq \eta \leq 1$ range, where $\eta = 1$ indicates a lossless propagation and $\eta = 0$ indicates an opened cavity and thus a stopped propagation, the geometric series converges to its nominal value and Eq. 3.23 becomes:

$$\begin{aligned}I_{tot}(t) = \frac{P_0}{1-\eta} &+ P_0 m\{\cos[2\pi ft] + \eta\cos[2\pi ft]\cos[2\pi f\tau] + \eta\sin[2\pi ft]\sin[2\pi f\tau]\} \\ &+ P_0 m\left\{\eta^2\cos[2\pi ft]\cos[4\pi f\tau] + \eta^2\sin[2\pi ft]\sin[4\pi f\tau]\right\} + ...\end{aligned} \tag{3.24}$$

where the trigonometric identity for angle substraction $\cos(a-b) = \cos a\cos b + \sin a\sin b$ was used. Since the modulation frequency f is chosen to let the period of the sine wave be much larger than the cavity length, the $2\pi f\tau$ terms bring only small corrections and the small angle approximation can be used. The total intensity is therefore:

$$I_{tot}(t) = \frac{P_0}{1-\eta} + P_0 m\left\{\cos[2\pi ft] + \eta\cos[2\pi ft] + \eta 2\pi f\tau\sin[2\pi ft] + \eta^2\cos[2\pi ft] + \eta^2 4\pi f\tau\sin[2\pi ft] + ...\right\} \tag{3.25}$$

By rearranging terms we get:

$$I_{tot}(t) = \frac{P_0}{1-\eta} + P_0 m\cos[2\pi ft]\{1 + \eta + \eta^2 + ...\} + P_0 m 2\pi f\tau\sin[2\pi ft]\{\eta + 2\eta^2 + ...\} \tag{3.26}$$

The geometric series and its first derivative converge to their nominal values to yield:

$$I_{tot}(t) = \frac{P_0}{1-\eta} + \frac{P_0}{1-\eta}m\cos[2\pi ft] + P_0\frac{\eta}{(1-\eta)^2}2\pi f\tau m\sin[2\pi ft] \tag{3.27}$$

By rearranging terms we obtain an expression for the total intensity in the cavity that is a function of a single cosine wave:

$$\begin{aligned}I_{tot}(t) &= \frac{P_0}{1-\eta}\left\{1 + m\cos[2\pi ft] + \frac{\eta 2\pi f\tau}{1-\eta}m\sin[2\pi ft]\right\} \\ &= \frac{P_0}{1-\eta}\left\{1 + m\sqrt{1 + \left(\frac{\eta 2\pi f\tau}{1-\eta}\right)^2}\cos[2\pi ft - \varphi]\right\}, \varphi = \arctan\left(\frac{\eta 2\pi f\tau}{1-\eta}\right) \approx \frac{\eta 2\pi f\tau}{1-\eta}\end{aligned} \tag{3.28}$$

The final expression for the total intensity in the cavity is:

$$I_{tot}(t) = \frac{P_0}{1-\eta}\left\{1 + m\sqrt{1 + \left(\frac{\eta 2\pi f\tau}{1-\eta}\right)^2}\cos\left[2\pi f\left(t - \frac{\eta\tau}{1-\eta}\right)\right]\right\} \tag{3.29}$$

The theorerical group delay is thus only function of the recirculation factor η for long cavity ring resonators:

$$\tau_g = \frac{\eta\tau}{1-\eta}, \tag{3.30}$$

where τ is the cavity round-trip time. Figure 3.12 shows the theoretical group delay as a function of the recirculation factor η and normalised by the cavity round-trip time τ.

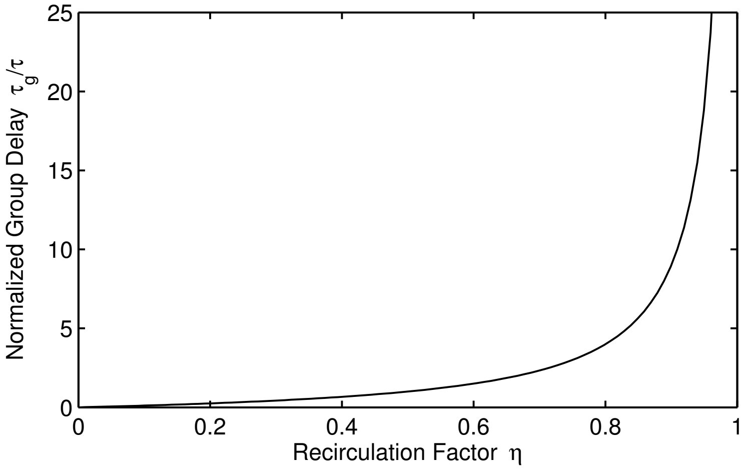

Figure 3.12. Theoretical group delay obtained using macroscopic cavity ring resonators as a function of the recirculation factor and normalised by the cavity round-trip time τ.

3.5.B. Experimental configuration and results

To test the effect of structural slow light on the optical absorption molecules, a long fibre cavity ring resonator system was built according to Fig. 3.13. Light from a DFB laser diode operating at 1534 nm was launched into the fibre cavity. The optical power of the light signal was precisely controlled using a variable optical attenuator (VOA) before entering the cavity as to avoid saturation of the erbium-doped fibre amplifier (EDFA) placed inside the cavity. The EDFA provided gain to the light signal to compensate any loss present in the cavity. A fibre Bragg grating (FBG) operated in reflection was used to filter out the amplified spontaneous emission coming from the EDFA and a second VOA was used to continously vary the cavity round-trip loss. To determine precisely its value, cavity ring down measurements were performed by sending short optical pulses into the cavity

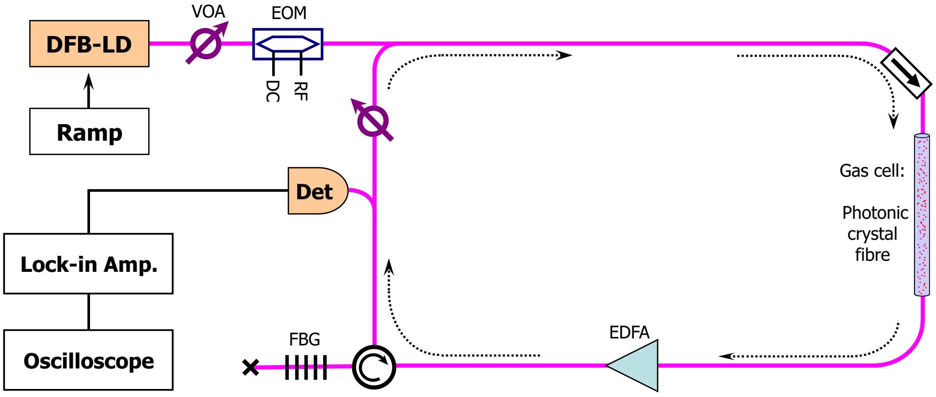

Figure 3.13. Experimental setup realising structural slow light using a long fibre ring resonator system. Variable group delay is achieved by modifying the propagation loss in the fibre loop. The gas cell is made of a photonic crystal fibre filled with acetylene gas and fusion spliced to standard single-mode fibres.

and detecting the pulse intensity decaying with each cavity round-trip (see Fig. 3.14). For these measurements the laser frequency was positioned in a spectral region where absorption resonances were absent and the pulses were generated using an electrooptic Mach-Zehnder intensity modulator (EOM).

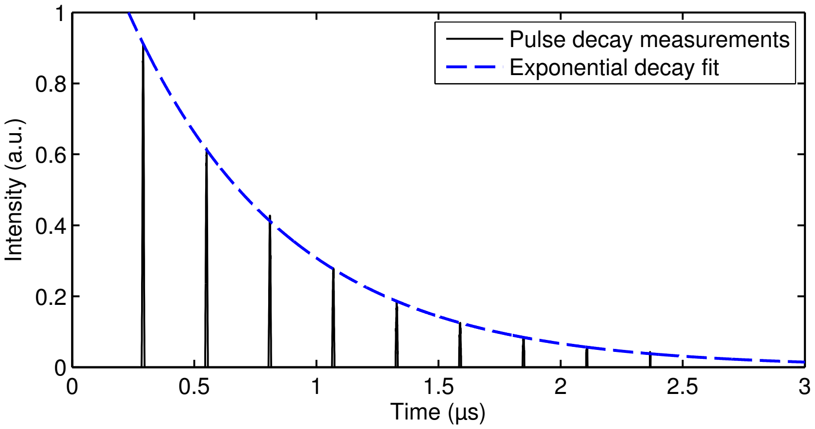

Figure 3.14. Cavity ring down measurements. A cavity round-trip loss of 1.7 dB/pass is found by fitting the exponentially decaying pulse intensities and measuring the cavity round-trip time (260 ns).

The cavity-induced group delay was then controlled by continuously varying the round-trip loss using a VOA. Semi-quantitative measurements of the group delay were performed by using 3.8 μs optical pulses. Relatively long optical pulses should be used so that they could be much narrower in the frequency domain than the free spectral range of the cavity. With the cavity acting as a frequency filter, the pulse width should be as narrow as possible in the frequency domain to avoid any frequency filtering effect, which would lead to temporal broadening. However the pulse width in the time domain cannot be increased arbitrarily as it will decrease the precision of the measured group delay. The value of 3.8 μs is therefore a compromise between avoiding pulse temporal broadening and distortion and obtaining a relatively precise measurement of the pulse delay. The pulse delay measurements are shown in the left panel of Fig. 3.15 for several round-trip losses.

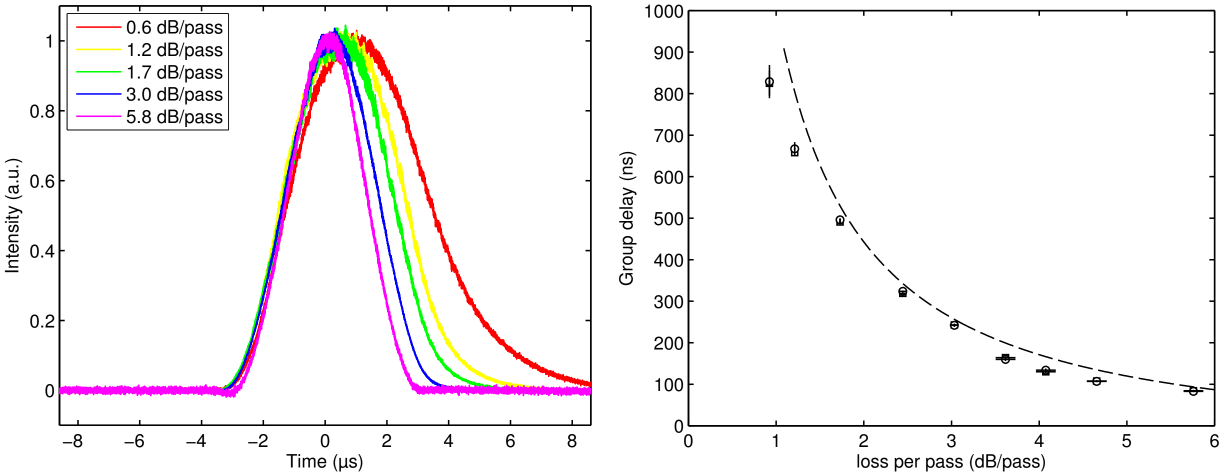

Figure 3.15. Left: Pulse delay measurements shown for several cavity round-trip losses. Decreasing the cavity loss leads to longer pulse arrival time through light recirculation. Right: Group delay measured as a function of the cavity round-trip loss using the phase shift technique. The dashed curve shows theoretical dependence obtained from Eq. 3.30 for a cavity round-trip time of 260 ns.

To determine precisely the cavity-induced group delay, the output of the laser diode was sinusoidally modulated at 70 kHz and 95 kHz by an electro-optic Mach-Zehnder intensity modulator (EOM) and the phase of the sine wave was measured after propagation through the cavity using a lock-in amplifier. Substracting this value from the phase of the sine wave measured with the cavity opened gave the phase shift value from which the group delay could be obtained. The phase shift measurements were performed at two different modulation frequencies to verify the accuracy of the measured group delay. In addition, the intensity modulator was operated at relatively high frequencies to maximize the precision of the phase shift measurements while staying below the 100-kHz bandwidth limit of the lock-in amplifier. The largest time delay achieved through the cavity was $\sim$ 700 ns for a loop time of 260 ns, corresponding to a group velocity reduced to 27 % of its nominal value. The phase shift measurements are shown in the right panel of Fig. 3.15 as a function of the cavity round-trip loss with the dashed line representing the theoretical group delay (Eq. 3.30).

Absorption profiles were obtained by applying a voltage ramp signal to the laser diode combined with lock-in detection to acquire clean signals. Figure 3.16 shows absorption profiles for the P14 acetylene line in a hollow-core PCF gas cell for several group indices and experimentally demonstrates substantial enhancement of the molecular absorption effect. Experimental data points were fitted with a theoretical model developped in the next section and show a fairly good agreement with the expected absorption enhancement. Absorption enhancements were also studied in the same solid-core PCF used for the material slow-light experiment. Figure 3.17 & 3.18 show the

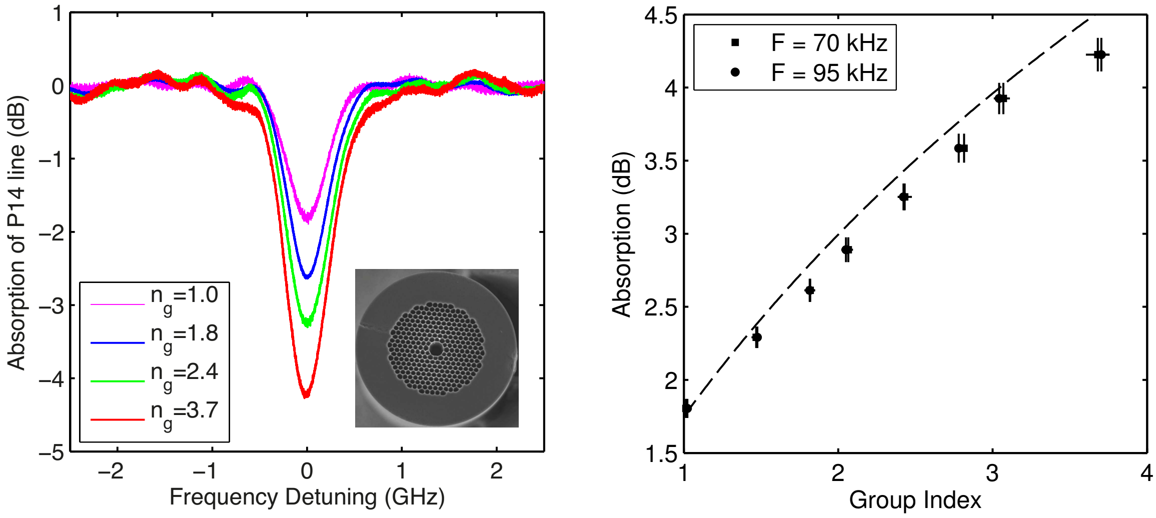

Figure 3.16. Left: Absorption profiles measured in the 5.0-m long hollow-core PCF for the P14 line ($\lambda = 1533.46$ nm) for several group indices. Right: Absorption enhancement as a function of the group index. The dashed line represents Eq. 3.35 fitted with $A_0 = 1.75$ dB.

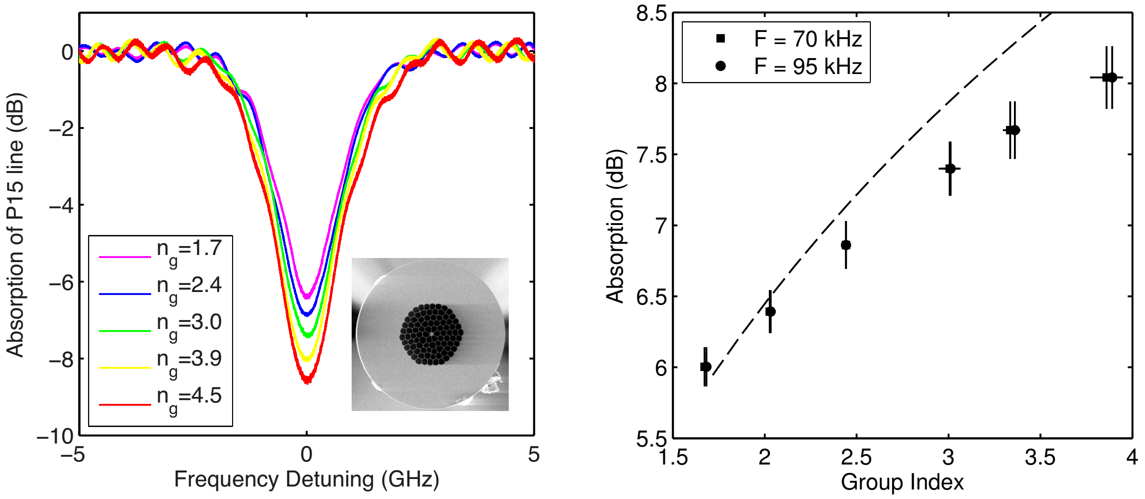

Figure 3.17. Left: Absorption profiles measured in the 9.18-m long solid-core PCF for the P15 line ($\lambda = 1534.10$ nm) for several group indices. Right: Absorption enhancement as a function of the group index. The dashed line represents Eq. 3.35 fitted with $A_0 = 5.5$ dB.

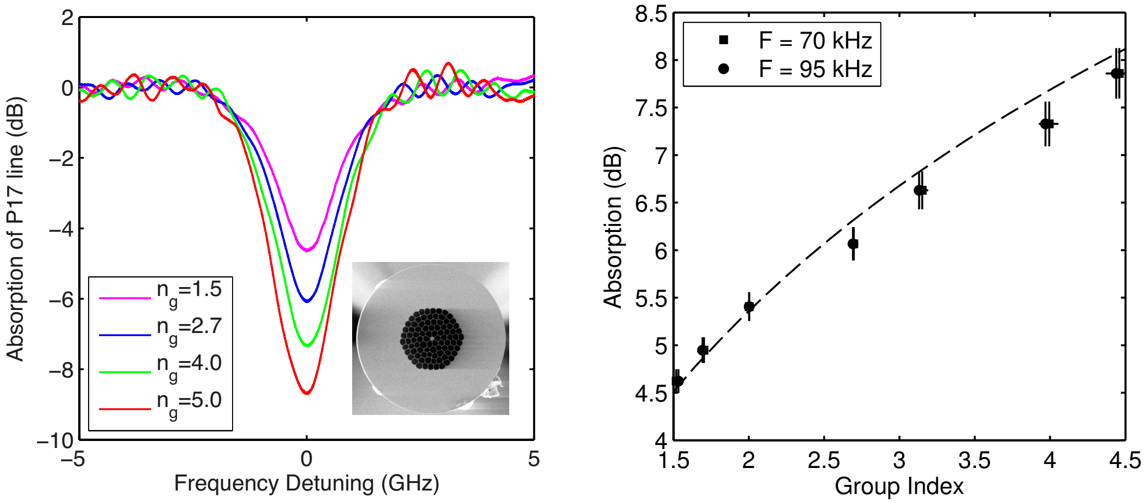

Figure 3.18. Left: Absorption profiles measured in the 9.18-m long solid-core PCF for the P17 line ($\lambda = 1535.40$ nm) for several group indices. Right: Absorption enhancement as a function of the group index. The dashed line represents Eq. 3.35 fitted with $A_0 = 4.5$ dB.

enhancement of the molecular absorption effect with respect to the group index in a solid-core PCF for acetylene lines P15 & P17 respectively, with Eq. 3.33 fitted to the data points. The theoretical model agrees fairly well for the P17 line, however the model performs somewhat badly for the P15 line. We believe this is due to a strong initial absorption for the P15 line causing additional loss in the cavity and hence reducing the cavity-induced group delay. As a result the absorption obtained for a given group velocity is subtantially less than that expected for the corresponding cavity losses (Eq. 3.30). Thus for strong absorption levels molecular absorption and slow light generation are impacting one another and cannot be controlled independently.

3.5.C. Discussion

This structural slow-light experiment clearly demonstrates the enhancement of the molecular absorption effect as a function of the cavity-induced group delay. This experimental result can actually be explained out of the framework of slow light theory, by looking at the actual intensity building up inside the cavity. Outside the absorption line the intensity build-up is found from the recirculation factor η:

$$I_{tot}(\alpha_L = 0) = I_0 + \eta I_0 + \eta^2 I_0 + \eta^3 I_0 + ... = \frac{I_0}{1-\eta}\ , \eta < 1 \tag{3.31}$$

in the incoherent case, where I_0 is the initial optical intensity arriving at the detector. Inside the absorption line the intensity build-up is:

$$I_{tot}(\alpha_L) = I_0 \exp(-\alpha_L L) + \eta I_0 \exp(-2\alpha_L L) + \eta^2 I_0 \exp(-3\alpha_L L) + ... = \frac{I_0 \exp(-\alpha_L L)}{1-\eta\exp(-\alpha_L L)}\ , \eta < 1 \tag{3.32}$$

As absorption profiles are normalized by the intensity outside the absorption resonance, the normalised absorption profile is:

$$\frac{I_{tot}(\alpha_L)}{I_{tot}(\alpha_L = 0)} = \frac{\frac{I_0 \exp(-\alpha_L L)}{1-\eta\exp(-\alpha_L L)}}{\frac{I_0}{1-\eta}} = \frac{(1-\eta)\exp(-\alpha_L L)}{1-\eta\exp(-\alpha_L L)}, \tag{3.33}$$

where $\exp(-\alpha_L L)$ is the single-pass normalised absorption. The graphical interpretation of Eq. 3.33 is shown in Fig. 3.19 and reveals an enhancement of the optical absorption effect as a function of the loss inside the cavity. The lower the loop loss and the more time energy spends circulating inside the cavity, therefore extending the interaction length for light-matter interaction and causing an apparent slowing of light signals measured by the group velocity.

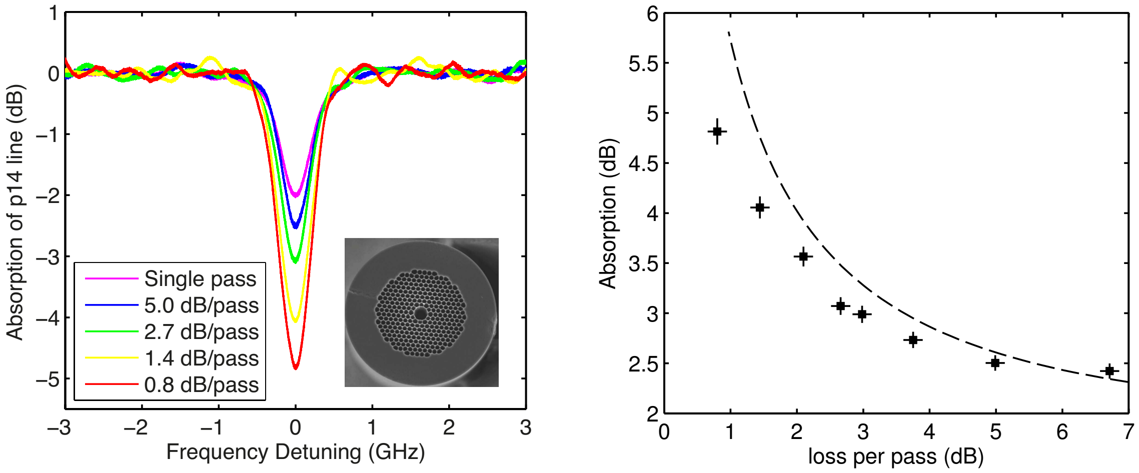

Figure 3.19. Left: Absorption profiles measured in the hollow-core PCF for the P14 line ($\lambda = 1533.46$ nm) for several cavity round-trip losses. Right: Absorption enhancement as a function of the cavity round-trip losses. The dashed line represents the theoretical absorption enhancement expected for a longer effective optical path length through light recirculation (Eq. 3.33).

The theoretical enhancement of absorption expressed as a function of the group index is obtained by replacing the recirculation factor η in Eq. 3.33 with $\eta = \tau_g/(\tau_g+\tau)$ according to Eq. 3.30. The logarithmic value of Eq. 3.33 is:

$$A(\tau_g, A_0) = 10 \cdot \log\left[1 - \frac{\tau_g}{\tau_g+\tau}\right] - 10 \cdot \log\left[1 - \frac{\tau_g}{\tau_g+\tau}10^{-A_0/10}\right] - A_0, \tag{3.34}$$

where A_0 is the single-pass absorption in dB scale. By doing some algebra we can obtain a simplified expression:

$$A(\tau_g, A_0) = -10 \cdot \log\left[1 + \frac{\tau_g}{\tau}\left(1 - 10^{-A_0/10}\right)\right] - A_0. \tag{3.35}$$

This expression describes the theoretical enhancement of the molecular absorption effect for structural slow light induced by macroscopic ring cavities. The enhancement of molecular absorption is not linearly proportional to the group index in such slow-light systems, in contradiction with theoretical work [4]. However it is worth pointing out that for small absorptions, i.e. when the absorption does not significantly impact on the round-trip loss, Eq. 3.35 reduces to an absorption coefficient that is linearly proportional to the group index:

$$A(\tau_g, A_0) = -10 \cdot \log\left[1 + \frac{\tau_g}{\tau}\left(\ln 10 \frac{A_0}{10}\right)\right] - A_0 = -\frac{\tau_g}{\tau} A_0 - A_0 = -\frac{A_0 n_g}{n}. \tag{3.36}$$

To illustrate this, Fig. 3.20 presents the absorption enhancement in the hollow-core PCF gas cell for a weak absorption line (T =95 %). Both the theoretical model and the linear model agree relatively well with the measured enhanced absorption and demonstrate that for cavity-induced slow light the absorption coefficient is linearly proportional to the group index in the weak absorption limit.

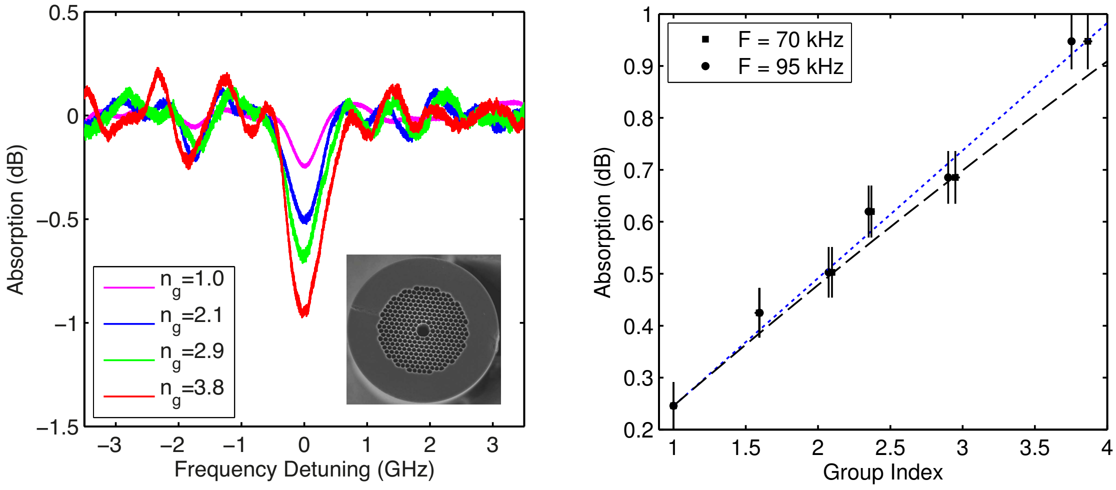

Figure 3.20. Left: Absorption profiles measured at λ = 1535.43nm in the 5.0-m long hollow-core PCF for several group indices. Right: Absorption enhancement as a function of the group index. The dashed line represents Eq.3.35 fitted with A_0 = 0.2457 dB while the dotted line represents an absorption coefficient scaling linearly with n_g (Eq. 3.36).

3.6. Conclusion

Experimental results of two different fibre-based slow-light systems were presented in this chapter. The absorption coefficient was measured for several group velocities in the very same fibre gas cell and for the same acetylene absorption lines using material and structural slow light. As illustrated in Fig. 3.21, no enhancement of molecular absorption was observed for material slow light whereas

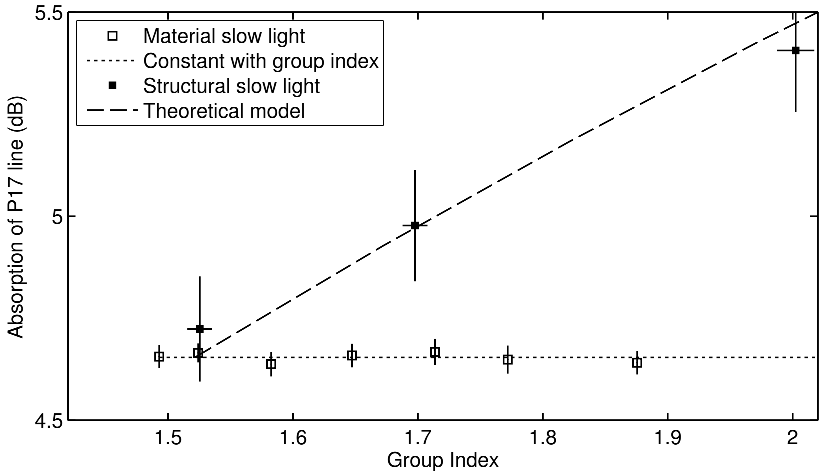

Figure 3.21. Dependence of the optical absorption of molecules on the group index for material slow light (white squares) and structural slow light (black squares). The dotted line represents an absorption coefficient constant with group index and the dashed line represents the theoretical model for the absorption enhancement in macroscopic cavities (Eq. 3.35). Larger error bars seen for the structural slow-light data points are related to normalisation issues due to a non-uniform intensity build-up of the line background, whereas gain uniformity is ensured for the material slow-light experiment via simultaneous tuning of the pump and signal waves.

enhancement could be observed for structural slow light. Since the dependence of the optical absorption of molecules on the group velocity is radically different depending on the slow-light generation mechanism, the group velocity may not be the appropriate universal quantity scaling light-matter interactions. In a periodic, lossless media such as ring resonators the velocity of energy propagation is identical with the group velocity of a quasi monochromatic wave [7, 8]. Reducing the electromagnetic energy velocity through structural slow light effectively increases the electromagnetic energy density and yields the observed enhancement of light-matter interactions. However in the presence of significant attenuation or gain part of the energy is dissipated or stored in material excitations and cannot contribute to enhance the EM energy density. The average velocity of the EM energy flow is negligibly changed by material resonances and cannot enhance the molecular absorption effect, as experimentally verified. Consequently, these experimental results suggest that the optical absorption of molecules is predominantly scaled by the electromagnetic energy velocity of optical lightwaves.

References

[1] Hochman, A. and Leviatan, Y. (2007). Efficient and spurious-free integral-equation-based optical waveguide mode solver. *Opt. Express*, 15(22):14431–14453.

[2] Jensen, K., Alam, M., Scherer, B., Lambrecht, A., and Mortensen, N. (2008). Slow-light enhanced light-matter interactions with applications to gas sensing. *Optics Communications*, 281(21):5335 – 5339.

[3] Khurgin, J. and Tucker, R. (2009). *Slow light: Science and Applications.* CRC Press.

[4] Mortensen, N. A. and Xiao, S. (2007). Slow-light enhancement of Beer-Lambert-Bouguer absorption. *Applied Physics Letters*, 90(14):141108.

[5] Santagiustina, M. (2011). Electromagnetic energy velocity in slow light. In *Slow and Fast Light*, page SLTuB5. Optical Society of America.

[6] Schulz-DuBois, E. (1969). Energy transport velocity of electromagnetic propagation in dispersive media. *Proceedings of the IEEE*, 57(10):1748 – 1757.

[7] Yariv, A., Xu, Y., Lee, R. K., and Scherer, A. (1999). Coupled-resonator optical waveguide: a proposal and analysis. *Opt. Lett.*, 24(11):711–713.

[8] Yeh, P. (1979). Electromagnetic propagation in birefringent layered media. *J. Opt. Soc. Am.*, 69(5):742–756.

CHAPTER 4

GAS SPECTROSCOPY USING PHOTONIC CRYSTAL WAVEGUIDES

4.1. Introduction

Photonic crystal waveguides represent the planar version of photonic crystal fibres (PCF). While for both light guiding structures lateral confinement of light is ensured by a photonic crystal lattice, vertical confinement in photonic crystal slab waveguides is ensured by standard total internal reflection. PC slabs are very compact devices, with physical dimensions typically in the millimeter range, and require very small sample volumes and very short filling times compared to PCF fibres. They could therefore be potentially very interesting devices for gas spectroscopy and for the detection of hazardeous material.

Several experimental studies have demonstrated some of the possiblities of photonic crystal slab technology in performing chemical sensing. Refractive refractive index sensing was performed using PC cavities [5, 15, 17], however this technique cannot specifically identify the detected chemical species since there is no individual fingerprint as in gas spectroscopy of rotational-vibrational transitions. Gas spectroscopy of methane was performed using dispersion-engineered photonic crystal slab waveguides in the slow-light regime [9], however the actual enhancement of optical absorption due to slow light was not experimentally verified. In addition the detection of carbone dioxyde was performed in [11] at one given wavelength without any wavelength modulation that would give an absorption profile and also further information about the physical properties of the detected set of molecules. Moreover they say an absorption enhancement of a factor 3 is experimentally obtained, however the impact of the group index on the absorption profiles was again not studied.

This work presents experimental studies of the optical absorption of acetylene gas in dispersion-engineered photonic crystal waveguides. Individual absorption profiles will be obtained using tunable diode laser absorption spectroscopy (TDLAS) and studied to gain information about the evanescent-field spectroscopic system that is formed by photonic crystal waveguides. Finally the effect of the group index on absorption profiles will be determined.

4.2. Photonic crystal waveguides

Photonic crystal waveguides consist of a high index thin film surrounded by an air cladding and having a two-dimensional array of air holes known as a photonic crystal (see Fig. 4.1 for one sample). Light is propagating through a line defect of missing air holes, confined in the lateral direction by a photonic bandgap effect and in the vertical direction by total internal reflection.

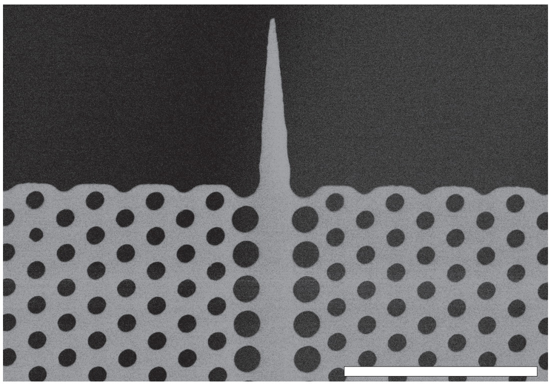

Figure 4.1. Micrograph of a photonic crystal waveguide made of Gallium Indium Phosphide (GaInP) (Courtesy of Thales Research and Technology). The membrane thickness is 180 nm (not shown here). The lattice constant is ∼500 nm and the diameter of the air holes is 220 nm. The white scale bar represents 3 μm.

Photonic crystals can be seen as two-dimensional Bragg gratings, where light is coherently backscattered at each dielectric interface. The distance between the centre of adjacent holes is known as the lattice constant a and is typically in the $400 - 500$ nm range. Light reflected at each dielectric interface will add up in phase for a certain wavelength range related to the lattice constant and light will eventually be prevented from propagating inside the photonic lattice. This wavelength range is called the stop band of the grating and its centre wavelength is given by the Bragg condition $\lambda_{Bragg} = 2a$. For these wavelengths the forward and backward travelling components agree in phase and amplitude, resulting in a standing wave inside the photonic lattice, or equivalently a wave propagating with zero group velocity. For wavelengths located near the band edge, the forward and the backward waves are slightly out of phase but still interact to yield a slowly moving interference pattern: the slow mode [1, 7].

4.3. Slow light in photonic crystal waveguides

As with structural slow light generated in optical fibres, slow light can be controlled in photonic crystal slabs by engineering the waveguide dispersion properties of the photonic lattice. Waveguide dispersion is here used as a global term and includes structural dispersion properties in periodic structures such as ring resonators. Strong tailorable dispersion can be obtained in photonic crystal waveguides due to the wavelength scale periodicity of the microstructure. To engineer their dispersion and slow-light properties the position or the size of the air holes of the photonic lattice are generally altered, with the two innermost rows of holes providing the strongest impact on waveguide dispersion. This has proven to be a successful method for controlling the group velocity as group indices of up to 100 have been demonstrated experimentally [14].

One important consequence of low group velocities resides in the enhancement of the optical intensity of the slow-light mode. Let's assume an arbitrary optical signal with an engineered group velocity constant over the range of wavelenghs considered. As it enters the slow-light medium the front of the optical signal will become slowed down with respect to the tail of the signal, which will then catch up with the front, resulting in spatial compression without any change in the corresponding spectral properties. In order to satisfy energy conservation the peak intensity would theoretically increase in the slow-light structure according to the group index n_g [8]:

$$I_{SL} = \frac{n_g}{n_\phi} I_0, \tag{4.1}$$

where I_0 is the optical intensity outside the slow-light medium and n_ϕ is the phase index. This linear scale law is however not observed in practice in photonic crystal waveguides because the mode field distribution generally changes with the group index. At low group indices the optical mode is confined in the lateral direction by a photonic bandgap effect, however at high group indices the slow-light mode extends further into the photonic lattice [6]. So even though the optical mode compresses in the propagation direction, this lateral spread will somewhat reduce the enhancement of optical intensity. Moreover we have shown that in structures made of long fibre resonators the enhancement of optical intensity in the slow-light regime is also not uniquely scaled by the group index but scales with the cavity loss as well.

Another consequence of low group velocities is related to propagation losses. Even if samples with very low group velocities can be fabricated, any benefit of using slow light can vanish if most of the light is lost in the process. These losses arise from fabrication imperfections such as roughness and deviation from a perfect microstructure. As the group index increases the optical intensity increases as well, leading to higher scattering loss due to the structure roughness. In addition slow light is usually created close to the Brillouin zone boundary and results from the strong coupling of a forward and a backward travelling waves. A higher group index will mean a stronger coupling between the two waves and will increase the amount of light scattered into the backward propagating mode [8, 14]. As a result propagation loss often scales with the square of the group index [4]. Typical loss is 5 dB/cm for standard fast propagation and up to 30 dB/cm in the slow-light regime ($n_g \gg 15$). Figure 4.2 presents the transmission and group index characteristics of a photonic crystal waveguide fabricated and characterised by Thales Research and Technology[2].

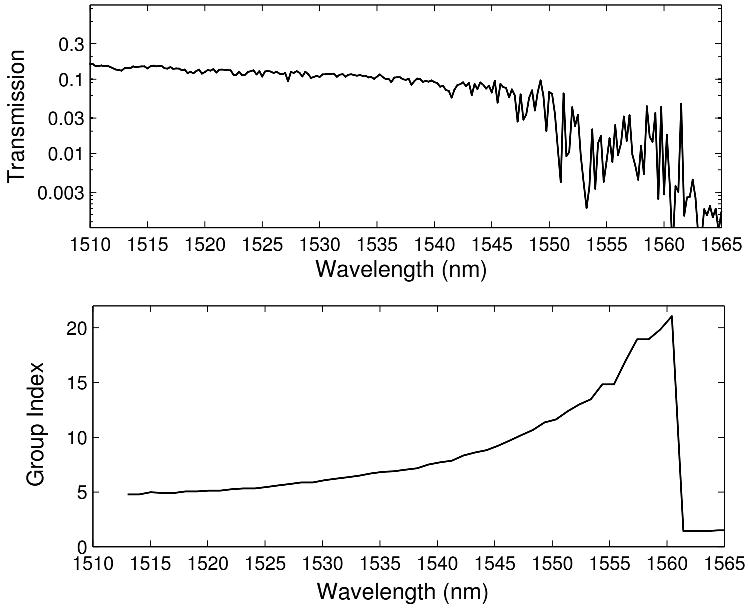

Figure 4.2. Transmission and group index characteristics of a photonic crystal waveguide fabricated and characterised by Thales Research and Technology, http://www.thalesresearch.com. The structural dispersion properties were tuned by increasing the innermost hole diameter from 224 nm to 252 nm.

However experimental studies reveal that the structural dispersion and hence the group velocity can be engineered without having detrimental effects on the propagation loss, indicating that general low propagation loss can be expected in the slow-light regime with further development of the technology [7]. The attenuation in photonic crystal slabs is however considerably higher than the typical propagation loss in optical fibres and is explained by the large difference in the refractive index contrast at dielectric interfaces. Photonic crystal slabs show much higher index contrast at the core-cladding interface, resulting in much stronger light scattering than in optical fibres. In addition optical fibres are fabricated from a heated macroscopic preform, which has the result of smoothing out any fabrication imperfection. Optical fibres therefore possess transverse structures that are extremely invariant along the propagation direction and light scattering is thus considerably reduced, compared to waveguide structures which are directly written in the material.

---

[2] http://www.thalesresearch.com

4.4. Experimental study of molecular absorption in photonic crystal waveguides

4.4.A. Experimental setup

The end-fire technique is commonly used to characterise photonic crystals. As depicted in Fig. 4.3, it consists in coupling externally-generated light into the device using optical fibres and measuring the corresponding change in intensity. The optical fibre must be precisely aligned with the line defect of the photonic crystal in the horizontal plane and with the high-index thin film in the vertical plane. Since the thickness of the high-index membrane is typically less than 200 nm and the width of the line defect less than 1 μm, lensed or tapered fibres are usually used to provide accurate optical coupling with the waveguide. Mode adapters are directly integrated into the slab waveguide to help build the slow-light mode by gradually increasing the group index [16]. They also suppress reflections at the cleaved facets due to the strong index contrast between the semicon-

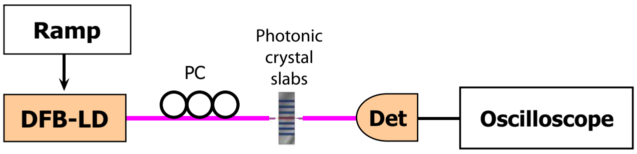

Figure 4.3. End-fire setup for photonic crystal characterisation. Optical coupling is ensured by lensed optical fibres precisely aligned with the line defect of the photonic crystals.

ductor material and the surrounding air cladding giving rise to Fabry-Perot patterns. The optical fibres are mounted on micropositioning stages, providing precise fibre positioning in all directions, and the fabricated samples are placed on chip holders. In addition since usually several photonic crystals are written per sample, a linear stage is used to provide lateral movement for the chip holder in order to rapidely and conveniently select different waveguides. Free-space optics can also be used as coupling optics, however for gas sensing measurements this would seriously affect the absorption measurements as an important fraction of light would be propagating in the gas-phase material. To ensure proper launching conditions a viewing setup comprising a microscope objective, a visible-IR camera, and an illumination system is used. Finally the position of the optical fibres with respect to the line defect of the waveguide samples is finely tuned by optimising the amount of light detected at the output.

To perform gas sensing measurements the end-fire setup was placed inside the very same gas chamber used to fill photonic crystal fibres. The volume of the gas chamber was increased to accommodate the micropositioning stages and additional optical feedthrough were added for monitoring the output transmission. Vacuum experiments were first performed to ensure that the modified gas chamber was airtight and that the positioning stages did not outgas at vacuum pressure. Then measurements of the stability of the transmitted optical signal were performed because the optical coupling is very sensitive on the displacement of the fibres. Deviations of 1 μm of the coupling optical fibres with respect to the waveguide will result in complete signal extinction and deviations as small as 100 nm will result in variations of several dB in the transmitted optical power. To completely immobilise the optical fibres V-grooved magnetic fibre holders were used in combination with small magnets. The magnets should be sufficiently strong to efficiently immobilise the fibres without causing any physical damage to the fibres. In addition the fibre holders were placed as close as possible to the samples to minimise the length of fibre suspended in air and thus minimise any cantilever effect which would verticaly change the position of the fibres with pressure. The effect is non-negligible at the nanometre scale range and is proportional to the fourth power of the cantilever length [2]. Finally the photonic crystal chips were glued to the sample holder using silver conductive paste to provide mechanical stability to the samples.

Then the stability of the optical coupling to mechanical vibrations created by the vacuum pump or by the gas chamber itself was tested. The photonic crystal sample was placed inside the chamber and the optical coupling of the optical fibres with the line defect of the waveguide was optimised. The polarisation of the incoming optical signal was set to TE using polarisation controllers to optimize the interaction with the photonic lattice. A linear polariser provided a fixed arbitrary polarisation which was modified using polarisation controllers so that the state of polarisation was set to TE when entering the waveguide. Figure 4.4 presents stability measurements in a photonic crystal with low group index over the wavelength range studied ($n_g \leq 10$). The solid line presents the transmission spectrum taken at atmospheric pressure with the gas chamber closed. Then air was evacuated from the gas chamber using a vacuum pump with the corresponding transmission spectrum shown as a dashed line. Finally acetylene gas was introduced in the gas chamber at a pressure of 70 mbars (dotted line).

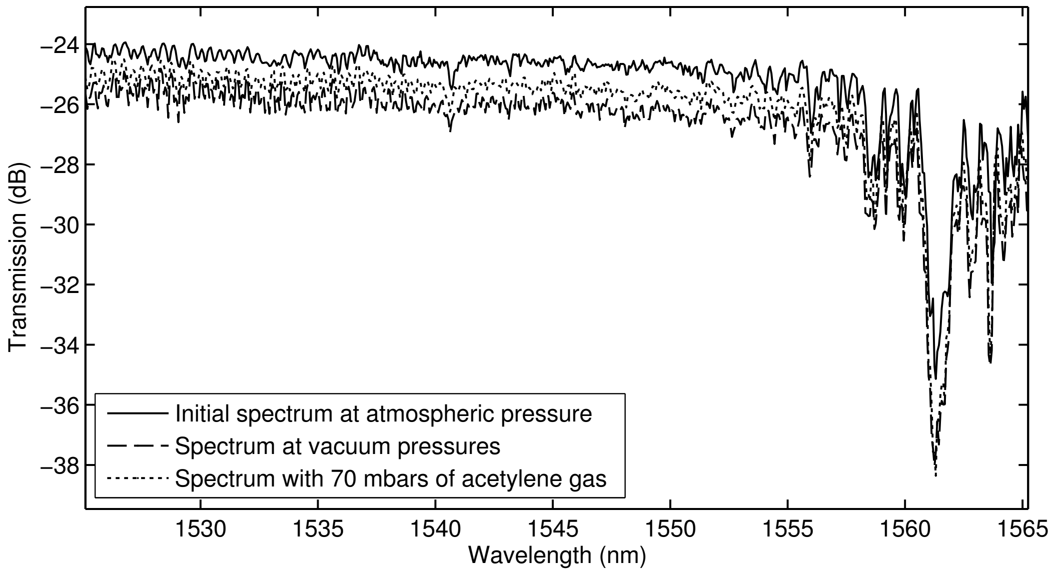

Figure 4.4. Stability of the optical coupling to external perturbations with the end-fire setup placed inside a gas chamber. Air is evacuated from the chamber using a vacuum pump and 70 mbars of acetylene gas is introduced in the chamber. A transmission difference of only 1 dB is obtained during the gas loading process.

As illustrated in Fig. 4.4, there is less than a 2 dB difference in transmission when air is evacuated from the gas chamber and this difference reduces to about 1 dB when the chamber is filled with acetylene gas. This behaviour is in agreement with the cantilever effect and the resulting fibre displacement due to a change in gas pressure. The optical coupling is clearly very sensitive to external perturbations but Fig. 4.4 shows good signal stability nevertheless, allowing gas sensing measurements to be performed. Individual absorption lines cannot be observed at this point due to the spectral resolution of the measurement, which is twice than the full width of the absorption lines (R=0.1nm).

To observe acetylene absorption lines the TDLAS spectroscopic technique was used. First the optical coupling and the input polarisation are optimised to observe photonic stopbands. The amplified spontaneous emission (ASE) of an erbium-doped fibre amplifier (EDFA) is used as a broadband source and an optical spectrum analyser is used to acquire transmission spectra. The gas chamber is then closed, and air is evacuated using a vacuum pump. Acetylene gas is introduced at a pressure of 70 mbars in the chamber and a broad transmission spectrum is acquired over the 1520-1570 nm wavelength range. Figure 4.5 presents transmission spectra of different waveguides with different values of the group index n_g at 1534 nm. Transmissions were all normalised to allow for better comparison between each measurement.

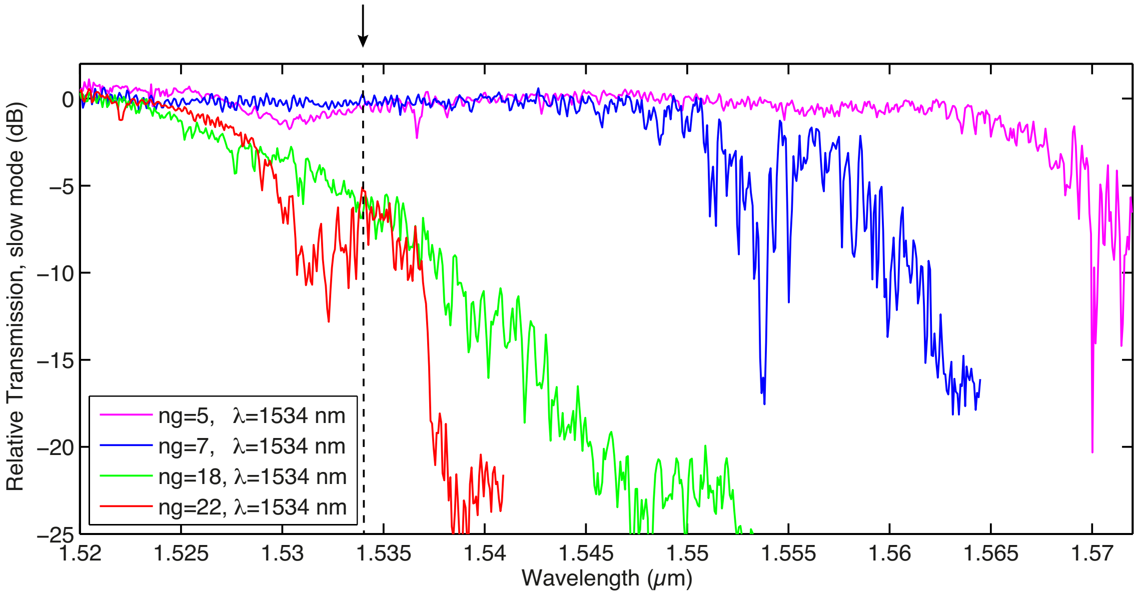

Figure 4.5. Transmission spectrum of several photonic crystal waveguides with different group indices n_g measured at 1534 nm. The band-edges are clearly seen for all measured waveguides and are positioned closer to the reference wavelength λ =1534 nm for waveguides having larger group indices at this wavelength, demonstrating that lower group velocities can be obtained for light signals propagating closer to the bandgap.

To observe individual absorption lines the EDFA is switched off and a distributed-feedback laser diode operating at 1534.10 nm is switched on. This process does not change the polarisation state of the light entering the photonic crystal line defect since a linear polariser is inserted in the setup after the light source and provides a fixed polarisation. Once the polarisation is optimised all optical components placed after the linear polariser remain untouched, including the photonic crystal itself and the coupling optics. To observe line shapes the driving current of the laser diode is linearly varied using a ramp current and the absorption profiles are acquired with an oscilloscope.

4.4.B. Results

The following figure presents the absorption profile of the P15 acetylene line measured for several group indices and experimentally demonstrates the dependence of the optical absorption on group velocity. Assuming that the mode field distribution varies negligibly from $n_g = 5$ to $n_g = 7$, the absorption seems to be proportional to n_g as $A(n_g = 7)/A(n_g = 5) \approx 7/5$. The assumption

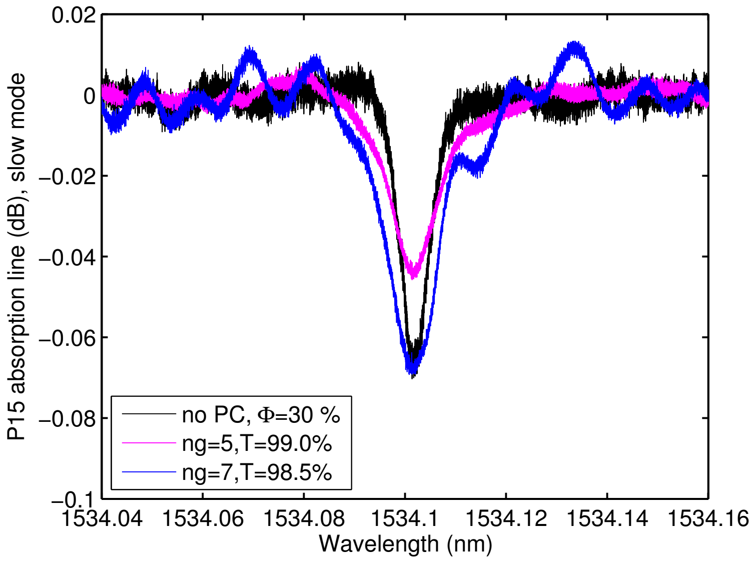

Figure 4.6. Variarion of the absorption line shape with group index. The black curve represents the experimental absorption of acetylene gas over a distance equal to 30 % of the photonic crystal length. The maximum absorption is $A = 0.0440$ dB for $n_g = 5$ and $A = 0.0678$ dB for $n_g = 7$. The linewidth is [0.87 ± 0.05] GHz for the black curve and [1.40 ± 0.05] GHz & [1.46 ± 0.05] GHz for $n_g = 5$ & $n_g = 7$ respectively. The difference in linewidths is due to different contributions from transit-time broadening (see §4.4.C for a detailed lineshape analysis).

will be verified in the next section by further analysing the absorption profiles. In addition, the measured absorption profiles demonstrate that no enhancement of optical absorption is obtained with respect to free space absorption. The absorption obtained is about 30% that of free space for the corresponding physical length (1.5mm). This is due to the fact that for TE polarisation most of the electric field is located in the photonic crystal membrane (the high index material, see Fig. 4.7). It seems that current photonic crystal slab technology offers no real bonus regarding molecular absorption with respect to free-space propagation and that further optimisation of the photonic crystal characteristics is needed. Finally the interference pattern seen in the $n_g = 7$ absorption spectrum is due to a stronger backward propagating wave leading to stronger cavity effects.

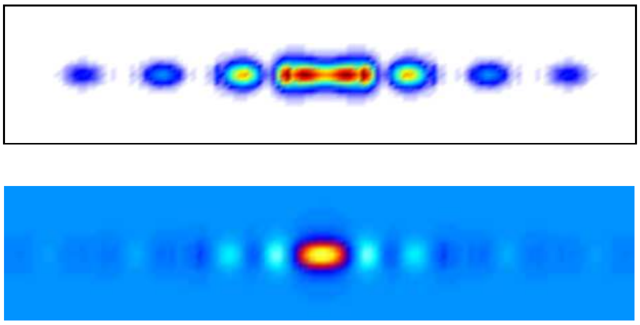

Figure 4.7. Top: Simulated intensity of the electric field $\| E \|^2$ for the TE polarisation along the transverse section of the photonic crystal slab. The electric field is strongly confined to the high-index dielectric slab and cannot therefore interact with the gas molecules. Bottom: Simulated time-averaged Poynting vector $\frac{1}{2}\Re[E \times H^*]$ for the TE polarisation along the transverse section of the photonic crystal slab. Numerical simulations are a courtesy of Thales Research and Technology.

Absorption profiles were also obtained for the TM polarisation. For this state of polarisation the electric field is perpendicular to the periodic lattice and therefore is not subject to a photonic bandgap effect. The group velocity is therefore assumed constant with an average value of $n_g = 1.7$. Figure 4.8 presents the absorption profiles for the TM polarisation for several photonic crystals engineered to obtain different TE group indices. The absorption coefficients measured along the TM polarisation are constant for all photonic crystals, a result which was expected since the optical mode sees the same average structure and the same group index.

In addition we find the unexpected result that even if the optical mode is guided in the high-

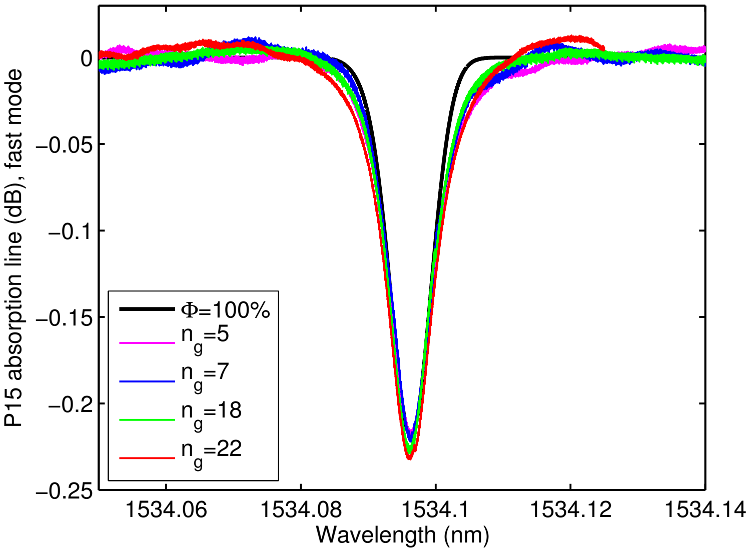

Figure 4.8. Absorption profiles along the TM polarisation for several photonic crystals with the n_g values corresponding to the TE engineered ones. The TM values are all approximately equal to $n_g = 1.7$. The black curve represents the simulated absorption of acetylene gas over a distance equal to the photonic crystal length for an overlap fraction between the optical power and the gas molecules of 100 %. The maximum absorption is $A = 0.218$ dB for the simulated molecular absorption (black curve) and $A = [0.224 \pm 0.007]$ dB for the absorption profiles measured in the photonic crystal samples.

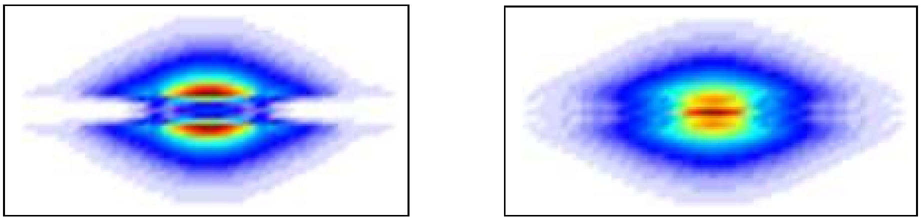

Figure 4.9. Left: Simulated intensity of the electric field $\| E \|^2$ for the TM polarisation along the transverse section of the photonic crystal slab. The electric field is located mostly in the lower-index material and can therefore strongly interact with the gas molecules. Right: Time-averaged Poynting vector $\frac{1}{2}\Re[E \times H^*]$ for the TM polarisation. Numerical simulations are a courtesy of Thales Research and Technology.

index material due to total internal reflection along the transverse section, we obtain the very same absorption coefficient as for an overlap fraction of 103 % for a free-propagating beam (black curve, simulation from experimental data shown in Fig. 4.6). For TM propagation most of the electric field is outside the photonic crystal slab (see Fig. 4.9), and therefore can interact strongly with the gas species. This is due to the discontinuous boundary conditions at material interfaces. For TM polarisation the electric field is perpendicular to the dielectric slab. At the boundary between a high-index dielectric material with electric permittivity $\varepsilon = n^2\varepsilon_0$ and a lower index air cladding with permittivity ε_0 the normal component of the electric displacement field $D = \varepsilon E$ must be continuous [13]. Since the electric permittivity is lower in air by a factor $\varepsilon/\varepsilon_0$ the normal component of the electric field will be much larger by the same factor $\varepsilon/\varepsilon_0$. As a result the electric field is increased in the lower-index cladding (here acetylene gas or otherwise air molecules) for the TM polarisation, leading to a high overlap fraction with the gas species and a strong absorption. We find the surprising result that gas sensing can be easily performed using TM polarisation as the electric field intensity $\parallel E \parallel^2$ is enhanced in the air cladding, and that the absorption is reduced for the TE polarisation as the mode field is strongly confined to the high-index photonic crystal membrane.

4.4.C. Lineshape analysis

Further analysis of the absorption profiles obtained for both polarisations is performed in this section to experimentally confirm the spatial distribution characteristics of the mode fields. Table 4.I presents the characteristics of the different absorption profiles obtained in photonic crystals compared to those of free-space propagation with 30% overlap between the optical mode and the gas molecules. The absorption linewidths were directly obtained from the measured absorption profiles and demonstrate that for TM polarisation the optical mode is approximately subject to the same broadening effects as in free space and that the effect of transit-time broadening is fairly negligible. As a result the lineshape function defined in Chapter 1 is approximately the same and the absorption coefficients can be directly compared. The absorption obtained for the TM polarisation is therefore the same as for an overlap fraction of ~100 % for a free-propagating beam with the same physical distance, even if the optical mode is guided in the high-index material. This special property is due to the enhanced electric field outside the photonic crystal slab interacting efficiently with the gas molecules.

Table 4.I. Characteristics of different absorption profiles obtained in photonic crystals

Absorption Line	Maximum Absorption [dB]	Normalised Absorption [%]	Linewidth [GHz]	Beam Radius [μm]
Free-space, $\Phi = 30\%$	0.065	30	0.87 ± 0.05 [a]	5.2 ± 0.5
TM polarisation	0.224 ± 0.007	103 ± 4	0.94 ± 0.01 [a]	0.8 ± 0.1
TE polarisation, $n_g = 5$	0.044	20	1.4 ± 0.1	0.13 ± 0.03 [b]
TE polarisation, $n_g = 7$	0.0678	31	1.5 ± 0.3	0.11 ± 0.08 [b]

---

[a] *a.* Transit-time broadening is thus fairly negligible

[b] *b.* Hence same spatial distribution

Table 4.I also presents the experimental beam radius values obtained from the absorption linewidths. First the Lorentzian component $\Delta\nu_L$ of the total linewidth $\Delta\nu_V$ was retrieved for each absorption profile using the following empirical equation:

$$\Delta\nu_V \approx 0.5346\Delta\nu_L + \sqrt{0.2166\Delta\nu_L^2 + \Delta\nu_G^2}, \tag{4.2}$$

where the Gaussian linewidth $\Delta\nu_G$ was estimated to 472 MHz from Eq. 1.20 in Chapter 1. The contribution of pressure broadening (585 MHz) was removed and the contribution from saturation broadening was assumed to be negligible as the optical power is much less than the theoretical saturation power (see Appendix II for the calculation). Finally the beam radius value was experimentally obtained from the remaining broadening contribution due to the limited transit time of gas molecules through the optical beam (Eq. 1.23). The obtained beam radius does not significantly change for the TE polarisation when the group index is increased from 5 to 7, indicating that the spatial distribution of the guided optical mode remains equal. Their respective absorption coefficients can therefore be directly compared to the group index and the result of the absorption coefficient being proportional to n_g is experimentally valid.

4.5. Theoretical absorption coefficient in photonic crystal waveguides

Theoretically the absorption coefficient is proportional to the fraction of the electric field intensity $\| E \|^2$ overlapping with the absorbers, divided by the Poynting vector averaged over the cross section:

$$\alpha = -\frac{dI}{I \cdot dx} \approx \frac{\int_{gas} \Im[\varepsilon] \| E \|^2 \, dV/2}{\Re[\int_S E \times H^* dS]}, \tag{4.3}$$

where H is the magnetic field and ε is the complex electric permittivity. The functions $\Re$ and $\Im$ denote the real and imaginary parts of a complex number, respectively and the integration volume V extends from x to $x + dx$ in the propagation direction. The Poynting vector describes the time-averaged flux of electromagnetic energy per unit time and per unit area and its value averaged over the cross section is proportional to the electromagnetic energy density via the velocity of the electromagnetic energy v_{EM} (see Eq. 3.13 in Chapter 3). With the electromagnetic energy velocity being equal to the group velocity for photonic crystal waveguides [12], Eq. 4.3 can be simplified and the theoretical absorption coefficient reduces to [10]:

$$\alpha \propto n_g \cdot f_E, \tag{4.4}$$

where f_E is the overlap fraction of the electric field with the absorbing region. The absorption coefficient is therefore a function of the electric field distribution and its evanescent fraction, in agreement with Fig. 4.9 (left) showing an enhanced electric field intensity $\| E \|^2$ in the air cladding. The absorption coefficient is independent of the optical intensity distribution since its value is integrated over the waveguide cross section. This is in agreement with Fig. 4.9 (right) showing relatively low fractions of the optical intensity outside the planar waveguide. In addition the absorption coefficient is expected to show a linear dependence as a function of the group index in photonic crystal waveguides.

Numerical simulations of the molecular absorption effect in photonic crystal waveguides have been performed for both TE and TM polarisations. Figure 4.10 presents the theoretical absorption coefficient for the TE polarisation normalised by the theoretical absorption that would be obtained in free-space propagation for the same physical length.

As illustrated in Fig. 4.10, the theoretical absorption coefficient is much less for the TE polarisation than that obtained in free-space propagation. A relative absorption coefficient of 28% is found

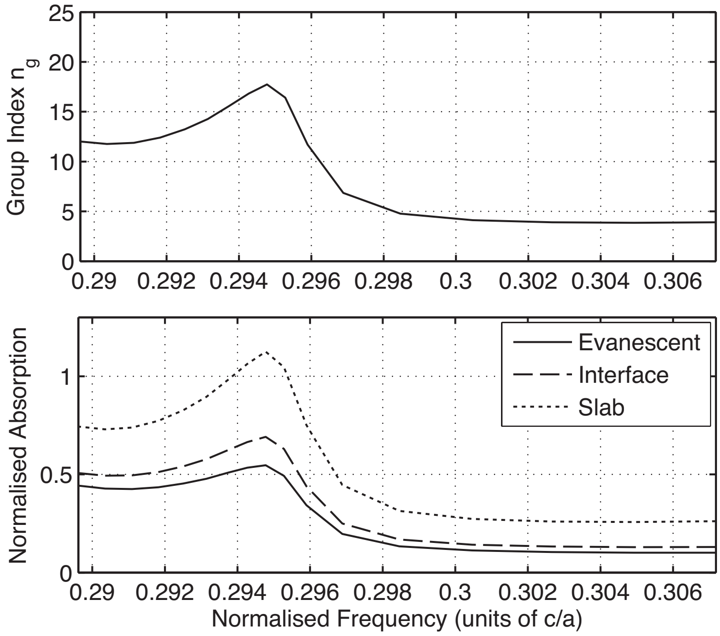

Figure 4.10. Simulated absorption relative to free-space propagation for the TE polarisation in photonic crystal waveguides as a function of the optical frequency normalised by the lattice constant a and the speed of light c. The electric field is strongly confined to the high-index dielectric slab and decays rapidely outside the slab in the low-index medium, leading to low overlap fractions with the gas molecules. The theoretical absorption coefficient is less than unity in all situations, hence smaller than in free-space propagation. Numerical simulations are a courtesy of Thales Research and Technology.

for a group index of 7 at the interface with the high-index thin film where most of the evanescent electric field is located; for a group index of 5 the relative absorption coefficient reduces to 17%. These theoretical values agree relatively well with the corresponding experimental values of 31% and 20%, respectively (see Table 4.I). In addition the theoretical absorption coefficient shows a dependence on the group index, which is also in agreement with the experimental work. Figure 4.10 also shows that there is not any enhancement of the molecular absorption effect with respect to free-space propagation. Even for large n_g values, the resulting absorption cannot exceed that in free space. Enhancement of the absorption is therefore only possible if the fraction of electric field outside the photonic crystal slab is increased.

The normalised absorption coefficient was also simulated for the TM polarisation. As illustrated in Fig. 4.11, the theoretical absorption coefficient in photonic crystal waveguides is approximately

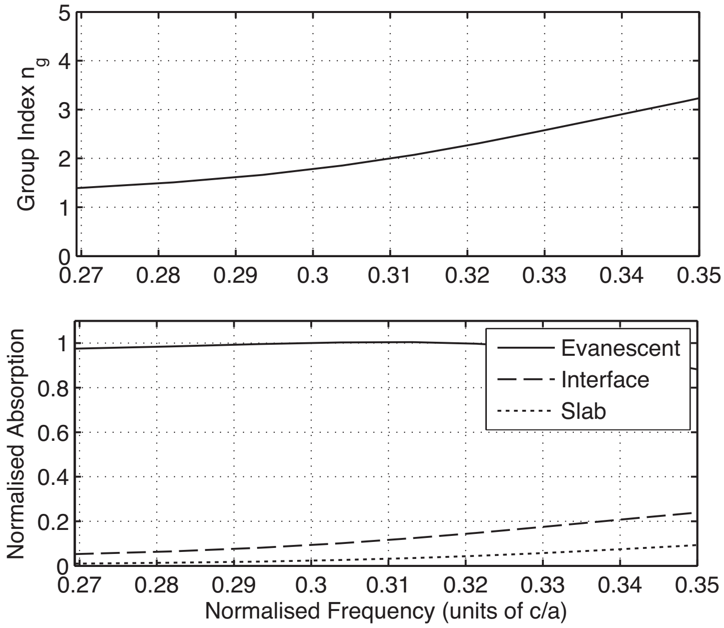

Figure 4.11. Simulated absorption relative to free-space propagation for the TM polarisation in photonic crystal waveguides as a function of the optical frequency normalised by the lattice constant a and the speed of light c. The electric field is located mostly in the low-index medium and can therefore strongly interact with the gas molecules. The theoretical absorption coefficient is approximately the same as that obtained in free-space propagation even though the optical mode is guided within the planar waveguide. Very weak dependence of the absorption coefficient on the group index is obtained. Numerical simulations are a courtesy of Thales Research and Technology.

the same as that obtained for free-propagating beams, even though the optical mode is guided in the PC slab waveguide and even for a TM group index of 1.7. In addition the ~100% relative absorption coefficient shows very weak dependence on the group index. Both results agree well with the experimental value of [103 ± 4] % obtained for the TM polarisation perpendicular to a broad range of TE-engineered group indices. The larger absorption coefficient obtained for the TM polarisation compared to the perpendicular one is due to the enhancement of the electric field intensity outside the photonic crystal slab for the TM polarisation, which benefits from the discontinuity of the electric field at the dielectric interface and the strong index difference between the two materials. The experimental and simulated absorption coefficients relative to free-space propagation are compared in Table 4.II.

Table 4.II. Experimental and simulated relative logarithmic absorption coefficients

Polarisation	Group index	Experimental Absorption [%]	Simulated Absorption [%]
TE	$n_g = 5$	20 ± 1	17
TE	$n_g = 7$	31 ± 2	28
TM	$\bar{n_g} = 1.7$	103 ± 4	100

4.6. Conclusion

In this Chapter we could experimentally demonstrate that the absorption coefficient linearly scales with the group velocity for photonic crystal waveguides. With the group velocity being equal to the electromagnetic energy velocity in such structures [12], the absorption effectively scales with the velocity of the electromagnetic energy, which has proven to be a more fundamental physical quantity scaling light-matter interactions according to Chapter 3. In addition we could experimentally show that the enhancement of the electric field density outside the photonic crystal slab is actually a more effective way of enhancing the absorption effect than considering only slow-light propagation. In the slow-light regime the total mode field intensity and the energy density approximately scale with the group index, however the intensity of the electric field outside the photonic crystal slab remains very low and strongly contributes to decreasing the observed absorption. Moreover the high-frequency interference noise caused by the strong optical coupling between the forward and backward components in the slow-light regime proved to be detrimental for gas sensing. Finally the experimental results all agree with numerical simulations performed by considering the absorption to be proportional to the electromagnetic energy velocity and to the overlap fraction of the electric field intensity with the absorbers.

These experimental results indicate that photonic crystal waveguides could become compact and effective gas sensing devices provided a careful design of the waveguide that would considerably enhance the intensity of the electric field outside the photonic crystal slab in the slow-light regime. One possible configuration could be slotted photonic crystal waveguides, where a thin air slot is cut in the middle of a photonic crystal line defect. This structure supports a guided mode confined mostly in air and which can efficiently interact with any material located in the slot. In addition the electric field of the slow-light TE-polarised mode is perpendicular to the slot dielectric interface in this geometry and strongly probes the discontinuity in the refractive index [3]. The electric field intensity of the TE-polarised slow mode is therefore enhanced in the air slot according to the index contrast between the semiconductor material and the air cladding and could potentially lead to enhanced light-matter interactions. However the photonic crystal lattice should be engineered so that the high-frequency interference noise present in its transmission spectrum is reduced to a minimum value, which would improve considerably the gas detection efficiency of the device in the slow-light regime.

References

[1] Baba, T. (2008). Slow light in photonic crystals. *Nature Photonics*, 2(8):465–473.

[2] Craig, R. (2000). *Mechanics of Materials*, volume 2. John Wiley & Sons.

[3] Di Falco, A., O'faolain, L., and Krauss, T. (2008). Photonic crystal slotted slab waveguides. *Photonics Nanostruct. Fundam. Appl.*, 6(1):38–41.

[4] Engelen, R. J. P., Mori, D., Baba, T., and Kuipers, L. (2008). Two regimes of slow-light losses revealed by adiabatic reduction of group velocity. *Phys. Rev. Lett.*, 101:103901.

[5] Jágerská, J., Zhang, H., Diao, Z., Thomas, N. L., and Houdré, R. (2010). Refractive index sensing with an air-slot photonic crystal nanocavity. *Opt. Lett.*, 35(15):2523–2525.

[6] Joannopoulos, J. D., Johnson, S. G., Winn, J. N., and Meade, R. D. (2008). *Photonic Crystals: Molding the Flow of Light.* Princeton University Press, 2$^{\text{nd}}$ edition.

[7] Khurgin, J. and Tucker, R. (2009). *Slow light:* S*cience and* A*pplications.* CRC Press.

[8] Krauss, T. F. (2007). Slow light in photonic crystal waveguides. *Journal of Physics D: Applied Physics*, 40(9):2666.

[9] Lai, W.-C., Chakravarty, S., Wang, X., Lin, C., and Chen, R. T. (2011). On-chip methane sensing by near-ir absorption signatures in a photonic crystal slot waveguide. *Opt. Lett.*, 36(6):984–986.

[10] Mortensen, N. A. and Xiao, S. (2007). Slow-light enhancement of Beer-Lambert-Bouguer absorption. *Applied Physics Letters*, 90(14):141108.

[11] Pergande, D., Geppert, T. M., Rhein, A. v., Schweizer, S. L., Wehrspohn, R. B., Moretton, S., and Lambrecht, A. (2011). Miniature infrared gas sensors using photonic crystals. *Journal of Applied Physics*, 109(8):083117 –083117–7.

[12] Sakoda, K. (2005). *Optical Properties of Photonic Crystals.* Springer Series in Optical Sciences. Springer, Heidelberg, Germany, 2$^{\text{nd}}$ edition.

[13] Saleh, B. E. A. and Teich, M. C. (2007). *Fundamentals of Photonics.* John Wiley & Sons, 2$^{\text{nd}}$ edition.

[14] Schulz, S. A., O'Faolain, L., Beggs, D. M., White, T. P., Melloni, A., and Krauss, T. F. (2010). Dispersion engineered slow light in photonic crystals: a comparison. *Journal of Optics*, 12(10):104004.

[15] Scullion, M., Falco, A. D., and Krauss, T. (2011). Slotted photonic crystal cavities with integrated microfluidics for biosensing applications. *Biosensors and Bioelectronics*, 27(1):101 – 105.

[16] Tran, Q. V., Combrié, S., Colman, P., and Rossi, A. D. (2009). Photonic crystal membrane waveguides with low insertion losses. 95(6):061105.

[17] Wang, B., Dündar, M. A., Nötzel, R., Karouta, F., He, S., and van der Heijden, R. W. (2010). Photonic crystal slot nanobeam slow light waveguides for refractive index sensing. 97(15):151105.

CONCLUSIONS AND PERSPECTIVES

Photonic crystal fibres (PCFs) have proven to be effective devices for performing light-matter interactions owing to their long interaction lengths and the small confinement volume of both the guided light and the gas molecules. One disadvantage of such configuration is related to the filling time of chemical species along the air holes, as their microscopic size compared to the length of the fibre capillaries may lead to an lengthy gas progression along the fibre. To evaluate the time scale of the filling process a simple model of the gas filling time has been developed. Based on the theory of gas diffusion, the model can be applied to any type of fibre, fibre geometry, or length. The validity of the model could be verified by analysing the gas filling dynamics in fibres samples of various geometries. This is a major background contribution brought by this thesis.

One important application of PCFs is to realise frequency references based on all-fibre gas cells. Combined with optical fibre fusion splicing, the helium permeation technique is a very effective mean of obtaining fibre gas cells containing a pure set of gas molecules. The efficiency of the sealing technique has been tested over a two year period with no visible sign of contamination and demonstrated the excellent long-term stability of all-fibre gas cells. These compact frequency references can be implemented in a straightforward way into practical systems and are very effective in terms of robustness, reliability, and long-term stability. A simple laser frequency stabilisation system could be developed by locking a laser line to the absorption line of acetylene gas contained in an all-fibre gas cell. Such portable frequency references can be attractive for space applications and they offer the additional benefits of alignment-free fibre-based systems. Finally the current state of the PCF technology allowed us to choose one particular fibre type according to a set of properties preferred for a given experiment. However it seems as if the design and fabrication of the ideal single-mode PCF fibre having a high overlap fraction of the optical mode with the fibre holes, that can be easily spliced to standard optical fibres, and that shows a high quality in its spectral transmission characteristics are challenging tasks for which the solution has not yet been found, if it ever exists. For the moment it is necessary to compromise between all these conditions.

For gas detection applications the long interaction length available in PCFs cannot completely compensate for low overlap fractions. In such cases the interaction length can be artificially increased via multipass absorption cells and cavity ring resonators to enhance the absorption effect.

Two experiments based on different slow-light generation mechanisms were conducted to test the possibilities of slow light in enhancing the absorption effect in optical fibres. The experiments were designed so that molecular absorption and slow light generation are not significantly correlated and can be controlled independently. Absorption cells made of photonic crystal fibres played the role of a slow-light medium and the velocity of light could be controlled by modifying the material and structural dispersion properties of the fibre system. The measured dependence of the optical absorption on the group velocity is radically different depending on the slow-light generation mechanism and suggests that the concept of pure group velocity is misleading for gas sensing applications. Group velocity merely describes the delaying effect of slow-light systems on light signals whereas gas sensing measurements are more intimately related to the concept of energy velocity. In structural slow-light the velocity of the electromagnetic energy is reduced and can enhance light-matter interactions through an increase in the electromagnetic energy density, whereas the latter is only very marginally modified in material slow-light and cannot lead to enhanced absorption. Modifying the structural properties of a system is the key element in enhancing the detection sensitivity.

Such systems include photonic crystal waveguides, where the structural dispersion properties are modified to increase the propagation time of light signals through the device. Gas spectroscopy of acetylene gas could be performed in dispersion-engineered photonic crystal waveguides and the impact of structural slow light on absorption experimentally evaluated. We could show that even if the experimental absorption coefficient is strongly dependent on the group index in PC waveguides, there is no net enhancement of the molecular absorption effect with respect to free-space propagation. In addition we could experimentally show that the enhancement of the electric field intensity outside the photonic crystal slab is actually a more effective way of enhancing the absorption effect than slow-light considerations alone. PC waveguides offer promising spectroscopic capabilities, however further optimization will be needed to improve both the evanescent field characteristics and the spectral quality of the device. Finally the strong sensitivity of the coupling optics to nanometer scale displacements is a important drawback towards practical implementation and must be addressed to ensure the long-term stability of the device.

As a summary the major contributions brought by this thesis are:

- Development of an analytical model predicting the gas-filling time in photonic crystal fibres.
- Determination and comparative study of the gas-sensing properties of different fibre samples

and geometries and conclusion that photonic crystal fibres showing a complete set of desired properties are not yet fabricated.

- Demonstration of the long-term stability of photonic crystal fibres as spectroscopic gas cells.
- Demonstration that material slow light has no impact on the optical absorption of molecules.
- Demonstration that structural slow light has an impact on the absorption efficiency and that the enhancement linearly scales with the group index.
- Conclusion that group velocity is not the universal physical quantity scaling light-matter interaction, but rather the velocity of the electromagnetic energy.
- Demonstration that in planar photonic crystal waveguides the field enhancement and its evanescent fraction have more impact on the absorption efficiency than the reduction of the group velocity of light signals.

From the experimental studies conducted in this thesis it turns out that slow light techniques do not necessarily lead to enhancement of light-matter interactions for gas spectroscopy applications. Experiments specifically designed to control the group velocity of light signals were not entirely effective in terms of gas sensing and better absorption results could be obtained by simply considering the structural and optical properties of the spectroscopic system. Instead of decreasing group velocities, spectroscopic systems should be designed so that the interaction length or the electric field intensity and its evanescent fraction are enhanced with respect to standard propagation. One possibility of development not yet investigated is to combine the long interaction length of fibre-based systems with the structural dispersion engineering capabilities of planar semiconductor devices as a means of enhancing the absorption effect. As an example one-dimensional Bragg gratings could be written in the solid-core of a photonic crystal fibre and operated in the slow-light regime by propagating light signals at the edge of the stop band as to enhance the electric field density. In addition Bragg gratings showing large index contrasts would be required in order to obtain strong structural dispersive effects and low electromagnetic energy velocities. Such structures could provide attractive gas sensing capabilities and hopefully provide new insights into the management of light-matter interactions.

Appendix I

Computation of the theoretical Lorentzian width

Here is computed the theoretical saturated Lorentzian width for the saturated absorption spectroscopy (SAS) experiment. The different contributions to the homogeneous width of the Lamb dip are summarized in Table I.I.

Table I.I. Calculated broadening contributions

Pressure broadening	$C_P \cdot P$	37 MHz
Transit time broadening	$u \cdot \sqrt{2\ln 2}/2\pi w$	21 MHz
Power broadening	$\frac{\Delta\nu_L}{2}\left[\sqrt{1+I/I_S}-1\right]$	14 MHz
Sum of all broadenings		72 MHz

The contribution of pressure broadening was evaluated from the coefficient C_P for the P14 acetylene absorption line (8.33 MHz/mbars; λ=1533.46nm [1]). The 5-m long absorption cell was filled with 4.5 mbars of acetylene gas, giving a contribution of 37 MHz to the Lorentzian linewidth. The most probable velocity u is 432.55 m/s for acetylene molecules and the beam waist of the optical field is 3.75 μm for hollow-core PCFs. The transit time of molecules through the optical beam is estimated to 9 ns, resulting in a spectral broadening of 21 MHz. This gives a theoretical unsaturated Lorentzian linewidth $\Delta\nu_L$ of 58 MHz. Using linear absorption data a theoretical saturation power of 410 mW was obtained in §1.5.B, giving a saturated Lorentzian width of 72 MHz for a pump power of 500 mW. This agrees well with the experimental dip width of 71 ± 1 MHz.

References

[1] Swann, W. C. and Gilbert, S. L. (2000). Pressure-induced shift and broadening of 1510–1540-nm acetylene wavelength calibration lines. *J. Opt. Soc. Am. B*, 17(7):1263–1270.

Appendix II

Computation of the theoretical saturation power in photonic crystal waveguides

Here is calculated the theoretical saturation power in photonic crystal waveguides to verify that the increase of the optical intensity of the guided mode is not saturating the acetylene transitions in the slow-light regime. The saturation intensity I_s is:

$$I_s = \frac{\varepsilon_0 c \hbar^2 \Gamma^2}{2\mu^2} \tag{II.1}$$

according to Chapter 1, where μ is the dipole moment of the transition and Γ is the relaxation rate of the transition. The relaxation rate represents the rate at which all molecules decay to the lower level and given by the Lorentzian linewidth homogeneous for all molecules. The transition dipole moment is found from the experimental absorption coefficient per unit length α_L according to Eq. 1.31 reproduced here:

$$\mu^2 = \frac{3\varepsilon_0 \hbar u}{\sqrt{\pi}} \frac{k_B T}{\Delta\eta} \frac{\alpha_L}{P}, \tag{II.2}$$

where $\Delta\eta = (N_n - N_m)/N$ is the relative population difference between the lower and upper levels and is given by the Boltzmann distribution:

$$\Delta\eta = \frac{N_n - N_m}{N} = \frac{N_n}{N}\left[1 - \exp\left(-\frac{h\nu_{mn}}{k_B T}\right)\right] \approx \frac{g_n}{Z}\exp\left(-\varepsilon_n hc/k_B T\right), \tag{II.3}$$

where g_n is the statistical weight for the lower level $|n>$, Z is the total internal partition function at $T = 296K$, and ε_n is the lower state energy in cm^{-1}. All three parameters can be found in HITRAN [1] for the P15 absorption line and give a value of 5.61 % for the relative population difference $\Delta\eta$. From Fig. 4.6 the absorption coefficient per unit length is $\alpha_L = 0.104\,\mathrm{cm}^{-1}$ for $n_g = 7$ and for a gas pressure of 70 mbars. The transition dipole moment is calculated using Eq. II.2 and a numerical value of $7.28 \cdot 10^{-33}\,\mathrm{C \cdot m}$ is obtained. The saturation intensity is therefore:

$$I_s = 7.868 \cdot 10^{-3} [\Delta\nu_L/2]^2\,\mathrm{mW}/\mu\mathrm{m}^2 = 3.308 \cdot 10^3\,\mathrm{mW}/\mu\mathrm{m}^2 \tag{II.4}$$

for a Lorentzian linewidth $\Delta\nu_L$ of 1297 MHz. It is then straightforward to calculate the saturation power from the total beam waist $w \approx 0.1\mu m$:

$$P_S = \pi w^2 \cdot 3.308 \cdot 10^3\,\mathrm{mW}/\mu\mathrm{m}^2 = 104\,\mathrm{mW}. \tag{II.5}$$

Such power levels can be reached in photonic crystal waveguides in the slow-light regime. It is however stronger than the ~ 1 mW power levels used in the slow-light experiment.

References

[1] Rothman, L. S., Gordon, I. E., Barbe, A., Benner, C., Bernath, P. F., Birk, M., Boudon, V., Brown, L. R., Campargue, A., Champion, J. P., Chance, K., Coudert, L. H., Dana, V., Devi, V. M., Fally, S., Flaud, J. M., Gamache, R. R., Goldman, A., Jacquemart, D., Kleiner, I., Lacome, N., Lafferty, W. J., Mandin, J. Y., Massie, S. T., Mikhailenko, S. N., Miller, C. E., Ahmadi, N. M., Naumenko, O. V., Nikitin, A. V., Orphal, J., Perevalov, V. I., Perrin, A., Cross, A. P., Rinsland, C. P., Rotger, M., Simecková, M., Smith, M. A. H., Sung, K., Tashkun, S. A., Tennyson, J., Toth, R. A., Vandaele, A. C., and Auwera, J. V. (2009). The hitran 2008 molecular spectroscopic database. *Journal of Quantitative Spectroscopy and Radiative Transfer*, 110(9-10).

LIST OF PUBLICATIONS

Journal publications

1. I. Dicaire, J.-C. Beugnot and L. Thévenaz,”Analytical modeling of the gas-filling dynamics in photonic crystal fibers” in Applied Optics, vol. 49, num. 24, p. 4604-4609 (2010).
2. L. Thévenaz, S. Chin, I. Dicaire, ”Molecular absorption under material and structural slow light illumination”, to be submitted to Nature Photonics.
3. I. Dicaire, A. de Rossi, L. Thévenaz, ”Probing molecular absorption using a photonic crystal waveguide under slow light propagation”, to be submitted to Optics Letters.

Conference proceedings

1. L. Thévenaz, I. Dicaire, S. Chin, ”Enhancing the light-atom interactions using slow light: towards the concept of dense light (Invited paper)”, in Photonics West - Advances in Slow and Fast Light V, San Francisco, California, USA, Proceedings of SPIE Vol 8273, 8273-48 (2012).
2. I. Dicaire, S. Chin, and L. Thévenaz, ”Structural slow light can enhance Beer-Lambert absorption,” in Slow and Fast Light, OSA Technical Digest (CD), paper SLWC2 (2011).
3. I. Dicaire, J.-C. Beugnot, L. Thévenaz, ”Optimized conditions for gas light interaction in photonic crystal fibres” in Fourth European Workshop on Optical Fibre Sensors, Proceedings of SPIE Vol. 7653, 76530L (2010).
4. L. Thevenaz, S. Chin, I. Dicaire, J.-C. Beugnot, S. Foaleng Mafang, M. González Herráez, ”Experimental verification of the effect of slow light on molecular absorption” in 20th International Conference on Optical Fibre Sensors, Proceedings of SPIE Vol. 7503, 75034W (2009).
5. I. Dicaire, J.-C. Beugnot, L. Thévenaz, ”Suspended-core fibres as optical gas sensing cells: study and implementation” in Photonic Crystal Fibers III, Proceedings of SPIE Vol. 7357, 73570U (2009).

LIST OF ABBREVIATIONS

ASE	Amplified Spontaneous Emission
DCF	Dispersion-Compensating Fibre
DET	Detector
DFB	Distributed-Feedback
EDFA	Erbium-Doped Fibre Amplifier
EOM	Electro-Optic Modulator
EM	Electromagnetic
FBG	Fibre Bragg Grating
FWHM	Full Width Half Maximum
GaInP	Gallium Indium Phosphide
Hg	Mercury
HITRAN	HIgh-resolution TRANsmission
HWHM	Half Width Half Maximum
H_2	Hydrogen
IR	Infrared
LD	Laser Diode
PBF	Photonic Bandgap Fibre
PBS	Polarisation Beam Splitter
PC	Polarisation Controller
PCF	Photonic Crystal Fibres
N_2	Nitrogen
OI	Optical Isolator
OSA	Optical Spectrum Analyser
O_2	Oxygen
SAS	Saturated Absorption Spectroscopy
SEM	Scanning Electron Microscope

SMF	Single Mode Fibre
SMTP	Source Model Technique Package
SBS	Stimulated Brillouin Scattering
TDLAS	Tunable Diode Laser Absorption Spectroscopy
TE	Transverse Electric
TM	Transverse Magnetic
UV	Ultraviolet
VOA	Variable Optical Attenuator
WMS	Wavelength Modulated Spectroscopy

CURRICULUM VITAE

ISABELLE DICAIRE
ELE 117, EPFL STI GR-SCI-LT Station 11, CH-1015 Lausanne | +41 21 693-5606
Email: isabelle.dicaire@gmail.com
Nationality: Canada
Birthdate: September 8th, 1983

Junior researcher in fibre optics and laser spectroscopy, EPFL

EDUCATION

- École Polytechnique Fédérale de Lausanne, Lausanne, Switzerland
  Ph.D. in Science. Specialisation in Photonics. 2007-2012

- Université de Montréal, Montréal, Canada
  M.Sc. in Science. Specialisation in Physics. Option: Astrophysics. 2005-2007
  Graduation honours: Dean's Honour List

- Université de Montréal, Montréal, Canada
  B.Sc. in Science. Specialisation in Physics. 2002-2005

JOURNAL PUBLICATIONS

1. I. Dicaire, J.-C. Beugnot, L. Thévenaz, "Analytical modeling of the gas-filling dynamics in photonic crystal fibers", Applied Optics **49**, 4604-4609 (2010).

2. I. Dicaire et al., "Hα kinematics of the *Spitzer* Nearby Galaxies Survey, II", MNRAS, **385,** 553-605 (2008).

3. I. Dicaire et al., "Deep Fabry-Perot Hα Observations of NGC 7793: a Very Extended Hα disk and a Truly Declining Rotation Curve", The Astronomical Journal, **135**, 2038-2047 (2008).

PROFESSIONAL BACKGROUND

- Teaching assistant at EPFL
  Supervision of student exercises 2009-2011

- Collaboration with Yonsei University, Seoul, South Korea
  Short stay to learn about numerical simulation tools October 2010

- Scientific editing of R&D reports, CET inc., Boucherville, Canada **2005-2007**

TECHNIQUES

Photonic crystal fibres, laser spectroscopy, arc-fusion splicing, gas diffusion dynamics, all-fiber gas cells, numerical simulations, spectroscopy techniques (saturated absorption, wavelength modulation), group velocity measurements, and photonic crystal waveguides.

LANGUAGES

French – Native language
English – Advanced level
German – Intermediate level (A2/B1 level; European language standards)